Wave Refraction Effects in High Intensity Focused Ultrasound

by

Lauren Burnett

A thesis
presented to the University of Waterloo
in fulfillment of the
thesis requirement for the degree of
Master of Mathematics
in
Applied Mathematics

Waterloo, Ontario, Canada, 2019

Author's Declaration

I hereby declare that I am the sole author of this thesis. This is a true copy of the thesis, including any required final revisions, as accepted by my examiners.

I understand that my thesis may be made electronically available to the public.

Abstract

High-Intensity Focused Ultrasound (HIFU) is a promising field of research being developed as an alternative to surgery and radiation therapy for the treatment of tumours. Within this field, many current methods of calculation/simulation use approximations rather than solve the Partial Differential Equation (PDE) directly. We consider the linear acoustic equation with and without damping for a material with spatially varying properties.

Our approach used spectral methods to manage the derivatives and solve the PDE. We started from the basics to tune our intuition for the problem. This allowed us to discuss some effects of phenomenological damping and to study the effects of wave reflection and refraction. Further, we were able to use these tools to investigate a possible cause of unexpected heating found clinically. To this end we used spectral numerical methods to solve the equation and applied stochastic analysis to examine the effects of variations in a few of the relevant parameters (sound speeds and the radius of an anomaly) on the outcome.

This model highlighted the fact that, due to the reflection and refraction of the ultrasound waves, more heating may occur inside obstacles in the treatment path than previously expected. The stochastic review found that discrepancies in the radius of the obstacle has a much larger impact on the outcome of the HIFU treatment than discrepancies in the parameters for the speed of sound in the various media. Thus more time and resources should be allocated to properly mapping and measuring the size and shape of obstacles in the treatment path as opposed to improving the exactness of the values for the speeds of sound.

Acknowledgements

I would like to start by thanking my supervisors Marek Stastna and Sivabal Sivaloganathan for their guidance and compassion, Marek in particular for his determination and help when things went sideways (again and again).

Thank you to my officemates: Ben Storer, David Deepwell, Xiaolin Bai, Will (Chengzhu) Xu, Laura Chandler, Liz Webb, and Sarah Walsh. You helped to keep me sane.

Also thank you to Andrew Grace, Lindsey Daniels, Justin Shaw, Aaron Coutino, Matt Harris, and Christian Barna for some very interesting discussions.

Finally, thank you to all of my family and friends, who helped me de-stress more times than I can count.

Dedication

This thesis is dedicated to my family.

Dad and Nana: I'm sorry you weren't able to see it finished. I miss you.

Table of Contents

List of Tables

List of Figures

Chapter 1

Introduction

High-Intensity Focused Ultrasound (HIFU) is a therapy currently being developed that will revolutionize the treatment of tumours, both benign and malignant. HIFU is non-invasive, unlike surgery, and unlike current radiation therapies HIFU does not use ionizing radiation which can damage otherwise healthy tissue. Focused ultrasound is a useful delivery method as it means only the focal area receives high levels of energy, sparing the surrounding healthy tissue. In fact, few severe side effects have been noted so far [7], largely some skin irritation or burns that clear within a day of treatment [6]. Figure 1.1 depicts a HIFU transducer creating a lesion.

Ultrasound is any sound with a frequency higher than the human hearing range (20 Hz to 20 kHz [16]). In medicine, the majority of people are familiar with the use of ultrasound for diagnostics, which usually uses frequencies in the 1-40 MHz range, depending on the tissue, with intensity of 8-100 mW/cm^2 [16]. HIFU however uses frequencies in the 2-6 MHz range with intensity of 2000 W/cm^2 [16]. This means four to five orders of magnitude more energy is used in HIFU than for diagnostic purposes, but unlike HIFU diagnostic ultrasound is not meant to deposit much energy in the tissues. To be a useful therapy HIFU requires energy being deposited into the target tissue.

HIFU treatment involves a temperature increase, mainly in the focal area by design. Changes in temperature in the body are described using Pennes's bioheat transfer equation [15] (see also [4]):

$$\rho_t c_t \frac{\partial}{\partial t} T = \vec{\nabla} \cdot \left(k \vec{\nabla} T \right) + W_b c_b (T_a - T) + q_m$$

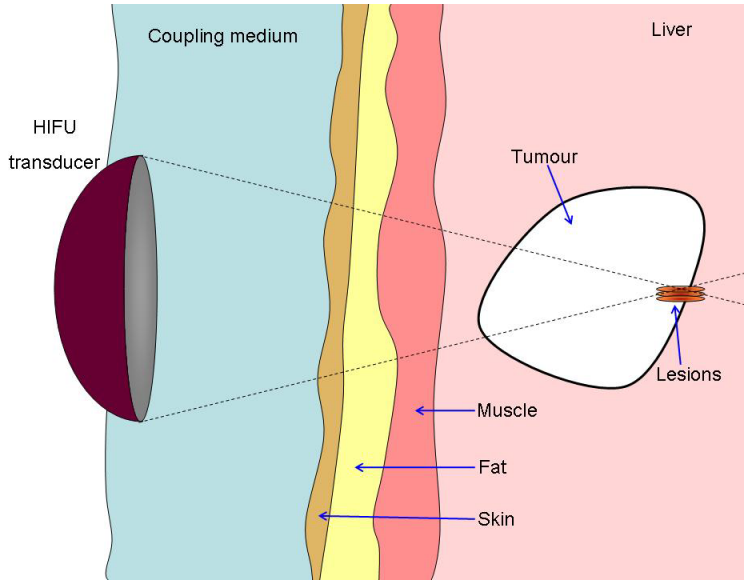

Figure 1.1: Diagram depicting a HIFU transducer creating a lesion at the focal site in a tumour. Many such lesions can be created inside the tumour volume for proper coverage. Adapted from McLaughlan [12]

where ρ_t is the tissue density; c_t is the tissue specific heat; T is temperature; k is thermal conductivity of the tissue; W_b is the mass flow rate of blood per unit volume of tissue; c_b is the blood specific heat; T_a is the arterial blood temperature and; q_m is the metabolic heat generation per unit volume. HIFU introduces an additional heat generation term that is dependent on the square of the acoustic pressure, ie $Q \propto |P|^2$ where P is the amplitude of the pressure [3, 5]. The equation can be written in terms of mechanisms as

$$\begin{aligned}\text{Rate of change of temperature with time} = \quad & \text{Diffusion} + \text{Transport by blood flow} + \\ & \text{Metabolic heat generation} + \text{Acoustic Heating}.\end{aligned}$$

The equation for pressure in an acoustic wave is

$$\frac{\partial^2 p}{\partial t^2} + b\frac{\partial p}{\partial t} = \vec{\nabla} \cdot \left(c^2 \nabla p\right) = 2c\vec{\nabla} c \cdot \vec{\nabla} p + c^2 \nabla^2 p$$

where b is a phenomenological damping coefficient and c is the speed of sound in the medium. A model using spectral methods was developed for this thesis to solve the above equation when moving through one medium into another. Chapter 3 specifically addresses

the case of tissue surrounding bone.

Immediate thermal toxicity occurs when a cell is at 56°C or more for at least one second and this thermal toxicity leads to coagulative necrosis triggering cell death [7]. HIFU can lead to temperatures upwards of 80°C [7]. HIFU actually has two mechanisms leading to the death of tumour cells: the hyperthermia (overheating) discussed here and cavitation (which involves the formation and destruction of micro-bubbles). This thesis focuses on the hyperthermia mechanism.

1.1 Therapy options

Surgery and radiotherapy are commonly used targeted therapies to treat both benign and malignant tumours but the variety of cancer types and locations means each treatment has a different efficacy in each condition. Maloney and Hwang [11] reviewed the application of HIFU for tumours in the liver, breast, pancreas, bone, connective tissue, thyroid, parathyroid, kidney and brain.

Tumours in the liver, kidneys and pancreas are all difficult to treat with current HIFU technology as the ribs make for a difficult treatment window and respiration causes too much movement in the area of the targets [11]. For now, ablation (the medical term for the destruction or removal of cells) of any kind is only advised for renal tumours in patients who are a high risk for surgery [8]. In the future HIFU could prove to be useful in these cases as new technology is developed, including accounting for respiratory movement using motion gating which is currently in development [11].

The initial findings for the treatment of thyroid, parathyroid and connective tissue tumours look promising but require more data gathering as there is currently a limited number of studies [11]. The non-invasive nature of HIFU makes it ideal for treatment in the brain, but transducers did not have the necessary power until recently. As such the use of HIFU to treat brain tumours could use more study as well [11]. Additionally, the cavitation mechanism of HIFU is uniquely useful when interacting with the brain as this allows HIFU to temporarily disrupt the blood-brain barrier [11], a significant hinderance in the past to other treatments relying on drug delivery.

Finally, HIFU has been found to be very effective for treating breast and bone tumours [11]. HIFU has been very successful treating both benign and malignant breast tumours, particularly for patients wanting a non-surgical solution to conserve breast tissue [11]. Bone metastases in particular mean significant pain for the patient and the current standard of care is radiation therapy [11]. However HIFU has shown a better rate of pain relief as well as "no significant adverse events" [11]. For primary bone tumours results have shown that HIFU treatment is comparable to surgical intervention combined with radiotherapy in efficacy and yet is non-invasive [11]. One example of a primary bone tumour is osteoid osteoma which usually forms in the cortex of bones in children and adolescents and so surgical options are difficult as they mean significant resection (surgical removal of part or all) of the bone and surrounding tissue [18]. In the particular case of osteoid osteomata, the current standard of care is radiofrequency ablation (RFA) but outcomes with HIFU are comparable without the same exposure to ionizing radiation [11]. In fact since it is mostly young patients who exhibit osteoid osteoma, collateral damage from surgery and ionizing radiation is more likely to have lasting negative effects in their lives [18].

In addition to considering HIFU as the first course of action for treatment, HIFU can be used after radiation is no longer viable due to maximum safe doses. HIFU also does not prevent other treatment options after its application [2]. As an emerging therapy HIFU requires more study, but the results so far also show that basic research into HIFU is likely to payoff tremendously and should absolutely continue in parallel.

The purpose of this thesis is to create a model using high order numerical methods and then applying said model to provide analysis of simple configurations. In this thesis Chapter 2 derives and develops the background for a model of HIFU and probes instances of refraction. Chapter 3 takes a parametric stochastic view, allowing parameters to vary to investigate if reasonable parameter variations would result in large changes in the outcome (i.e. sensitivity analysis).

Chapter 2

Model Development

This chapter presents the background of a linear model of HIFU in the presence of variable sound speed, starting with tutorial material. The ultimate goal is a numerical simulation but we start by looking at how far a semi-analytic approach can take us. First, the wave equation is developed from basic gas dynamics. This is followed by a discussion of the effects of scattering and phenomenological damping in a variety of situations that allow a semi-analytical solution. Finally this chapter concludes with a numerical application of refraction both with and without damping.

2.1 Derivation of Wave Equation from Basic Equations for Sound

Neglecting Earth's gravity and rotation (negligible for audible frequencies and above) as well as diffusion and viscosity to simplify the problem gives the governing equations:

$$\begin{aligned} \rho_t + \vec{\nabla} \cdot (\rho \vec{u}) &= 0 \\ \rho \frac{D\vec{u}}{Dt} + \vec{\nabla} p &= 0 \\ \frac{DS}{Dt} &= 0 \end{aligned} \tag{2.1}$$

where ρ is density, $\vec{u}$ is velocity and S is entropy. The first equation is conservation of mass, the second is conservation of linear momentum and the third is conservation of energy. Note that starting from an undisturbed state with constant ρ_0, $p_0 = \bar{p}(\rho_0)$ and

$\vec{u}_0 = 0$ means entropy is initially uniform and the third equation in 2.1 implies entropy remains that way as long as any disruptions to the system do not change the entropy, giving $p = \bar{p}(\rho)$. Perturbation approximations are now made for p, ρ and $\vec{u}$ using ϵ to denote the small amplitude of the perturbations from the undisturbed states (recall $\vec{u}_0 = 0$):

$$\begin{aligned} p &= p_0 + \epsilon p' \\ \rho &= \rho_0 + \epsilon \rho' \\ \vec{u} &= \epsilon \vec{u}'. \end{aligned}$$

After substituting these perturbations into 2.1 and performing a few manipulations, a linear approximation is obtained by eliminating all terms that contain ϵ, since ϵ is assumed to be very small in comparison to the other terms.

$$\rho'_t + \rho_0 \vec{\nabla} \cdot \vec{u}' = 0 \tag{2.2}$$

$$\rho_0 \vec{u}'_t + \vec{\nabla} p' = 0 \tag{2.3}$$

$$p' - c^2 \rho' = 0 \tag{2.4}$$

These can be reworked to eliminate p' by using 2.4 in 2.3 and taking the partial derivative with respect to time of 2.2 to find

$$\rho'_{tt} + \vec{\nabla} \cdot (\rho_0 \vec{u}'_t) = 0 \tag{2.5}$$

$$\rho_0 \vec{u}'_t + \vec{\nabla} c^2 \rho' = 0 \tag{2.6}$$

Using 2.6 in 2.5 an equation with only ρ' as a variable is obtained

$$\rho'_{tt} - c^2 \nabla^2 \rho' = 0.$$

Notice that because of the equation of state this wave equation could also be written for p. Similarly, taking the partial derivative with respect to time of 2.6 gives

$$\rho_0 \vec{u}'_{tt} + \vec{\nabla} c^2 \rho'_t = 0$$

and substituting in from 2.2 an equation in $\vec{u}'$ is obtained

$$\vec{u}'_{tt} - c^2 \vec{\nabla} (\vec{\nabla} \cdot \vec{u}') = 0.$$

Notice that in one dimension these become

$$\begin{aligned} \rho_{tt} - c^2 \rho_{xx} &= 0 \\ u_{tt} - c^2 u_{xx} &= 0, \end{aligned}$$

or one dimensional wave equations in ρ and u.

The 3D wave equation can be written in terms of the pressure as

$$\frac{\partial^2}{\partial t^2} p = c^2 \nabla^2 p$$

. Using three dimensions allows for the modeling of more realistic interactions between waves, but is more taxing on computers when running simulations and makes analytical progress difficult. Thus this chapter starts with one dimension in which analytical and semi-analytical progress is possible. Note also that ultrasound waves are attenuated in the body, as is the case for many practical situation in acoustics. Attenuation can be accounted for by including a phenomenological damping term to allow for the loss of energy from the wave into the tissue. More realistic models of tissue could also follow the example of elasticity theory, and allow for shear and Rayleigh waves. Again, to facilitate analytical progress, we focus on the case of purely compressive waves.

2.1.1 Wave Equation with Damping in One-Dimension

In order to develop some basic intuition, we start by looking at a 1D wave equation that includes damping, or "absorption":

$$u_{tt} + b u_t = c^2 u_{xx} \tag{2.7}$$

In order to determine at what time and space scales the absorption term is significant, the equation is non-dimensionalized using $y = \frac{x}{L}$ and $s = \frac{t}{T}$,

$$\begin{aligned}
\frac{\partial^2}{\partial t^2} u(x,t) + b \frac{\partial}{\partial t} u(x,t) &= c^2 \frac{\partial^2}{\partial x^2} u(x,t) \\
\left(\frac{\partial}{\partial s} \frac{\partial s}{\partial t} \right)^2 u(x,t) + b \left(\frac{\partial}{\partial s} \frac{\partial s}{\partial t} \right) u(x,t) &= c^2 \left(\frac{\partial}{\partial y} \frac{\partial y}{\partial x} \right)^2 u(x,t) \\
\frac{1}{T^2} \frac{\partial^2}{\partial s^2} u(yL, sT) + \frac{b}{T} \frac{\partial}{\partial s} u(yL, sT) &= \frac{c^2}{L^2} \frac{\partial^2}{\partial y^2} u(yL, sT)
\end{aligned}$$

Using $u(x,t) = u(yL, sT) = \tilde{u}(y,s)$:

$$\frac{\partial^2}{\partial s^2}\tilde{u}(y,s) + bT\frac{\partial}{\partial s}\tilde{u}(y,s) = \frac{T^2c^2}{L^2}\frac{\partial^2}{\partial y^2}\tilde{u}(y,s)$$
$$\tilde{u}_{ss} + bT\tilde{u}_s = \frac{T^2c^2}{L^2}\tilde{u}_{yy}$$

To use this result, from now on (x,t) will be referring to non-dimensionalized values (described here as (y,s)). Also notice that choosing $T = \frac{1}{b}$ and $L = \frac{c}{b}$ results in:

$$u_{tt} + u_t = u_{xx}$$

So the absorption term is significant at a scale where $T = \frac{1}{b}$ and $L = \frac{c}{b}$.

2.1.2 Dispersion

Using the wave ansatz

$$u(x,t) = e^{i(kx-\omega t)}$$

to get k as a function of ω gives

$$\begin{aligned} k(\omega) &= \pm\sqrt{\omega^2 + i\omega} \\ &= \pm\left(\omega^4 + \omega^2\right)^{\frac{1}{4}} e^{\frac{i\theta}{2}} \\ \text{where } \theta &= \arctan\left(\frac{1}{\omega}\right), \arctan\left(\frac{1}{\omega}\right) + \pi \end{aligned}$$

Notice that for any $\omega \neq 0$ there are both real and imaginary components to k resulting in (damped) propagation of the wave. To obtain more information about the behaviour of $k(\omega)$, the high and low frequency limits are investigated.

For low frequencies ω^2 will get very small so the $i\omega$ and k^2 terms will balance. To start we have the approximation:

$$k \approx k_0\omega^{\frac{1}{2}} + k_1\omega^{\frac{3}{2}} + k_2\omega^{\frac{5}{2}} + k_3\omega^{\frac{7}{2}}$$

from $k(\omega) = \pm\sqrt{\omega^2 + i\omega}$. Putting this into $k^2 = \omega^2 + i\omega$ and collecting terms:

$$k_3^2\omega^7 + 2k_2k_3\omega^6 + (2k_1k_3 + k_2^2)\omega^5 + (2k_0k_3 + 2k_1k_2)\omega^4 + (2k_0k_2 + k_1^2)\omega^3 + 2k_0k_1\omega^2 + k_0^2\omega = \omega^2 + i\omega$$

For this to be true the coefficients of the powers of ω must match. The first being:

$$k_0^2 = i$$
$$k_0 = \pm\frac{\sqrt{2}}{2}(1+i)$$

The second must satisfy:

$$2k_0k_1 = 1$$

So

$$k_1 = \begin{cases} \frac{\sqrt{2}}{4}(1-i) & \text{if } k_0 = \frac{\sqrt{2}}{2}(1+i) \\ -\frac{\sqrt{2}}{4}(1-i) & \text{if } k_0 = -\frac{\sqrt{2}}{2}(1+i) \end{cases}$$

The ω^3 terms must satisfy:

$$2k_0k_2 + k_1^2 = 0$$

So

$$k_2 = \begin{cases} \frac{\sqrt{2}}{16}(1+i) & \text{if } k_0 = \frac{\sqrt{2}}{2}(1+i) \\ -\frac{\sqrt{2}}{16}(1+i) & \text{if } k_0 = -\frac{\sqrt{2}}{2}(1+i) \end{cases}$$

So at low frequencies:

$$k = \begin{cases} \frac{\sqrt{2}}{2}(1+i)\omega^{\frac{1}{2}} + \frac{\sqrt{2}}{4}(1-i)\omega^{\frac{3}{2}} + \frac{\sqrt{2}}{16}(1+i)\omega^{\frac{5}{2}} \\ -\frac{\sqrt{2}}{2}(1+i)\omega^{\frac{1}{2}} - \frac{\sqrt{2}}{4}(1-i)\omega^{\frac{3}{2}} - \frac{\sqrt{2}}{16}(1+i)\omega^{\frac{5}{2}} \end{cases}$$

The behaviour of the real part is shown in Figure 2.1 and the behaviour of the imaginary part in Figure 2.2 where the black line is the full solution and the red line is this approximate solution.

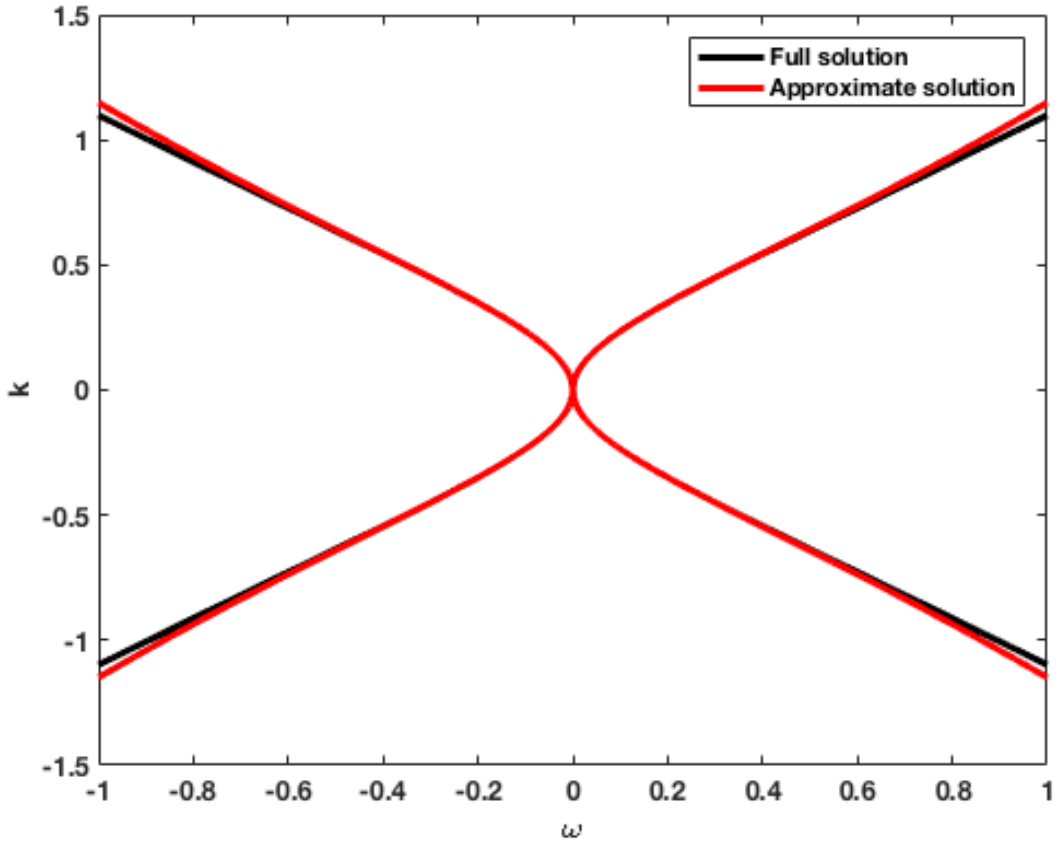

Figure 2.1: Plot of the real part of the low frequency limit approximation of $k(\omega)$. The red line is the approximate solution and the black line is the full solution for comparison.

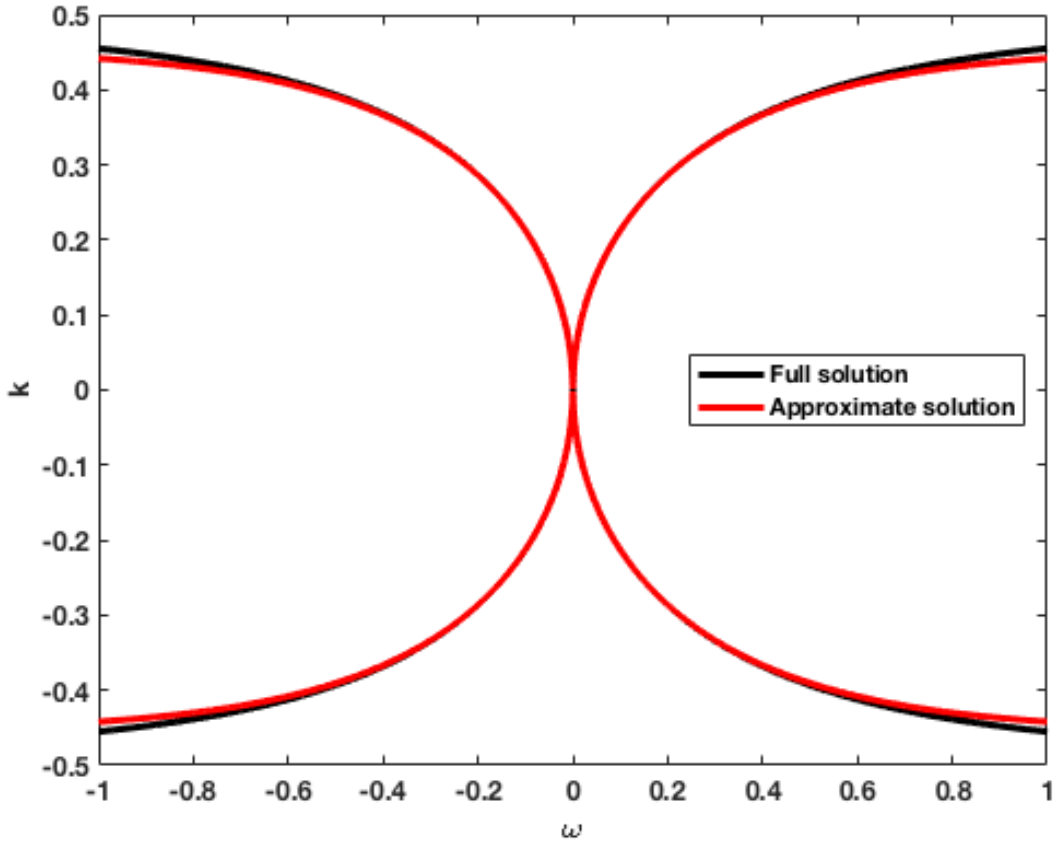

Figure 2.2: Plot of the imaginary part of the low frequency limit approximation of $k(\omega)$. The red line is the approximate solution and the black line is the full solution for comparison.

Now for high frequencies we want to balance the ω^2 and k^2 terms (as $i\omega$ becomes negligible). To better look at this balance we rescale using $l^2 = \frac{k^2}{\omega^2}$ and $\epsilon = \frac{1}{\omega}$:

$$k^2 = \omega^2 + i\omega$$
$$l^2 = 1 + i\epsilon$$

So we use the approximation:

$$l = l_0 + l_1\epsilon + l_2\epsilon^2$$

Putting this into $l^2 = 1 + i\epsilon$ and collecting terms:

$$l_2^2\epsilon^4 + 2l_1l_2\epsilon^3 + (2l_0l_2 + l_1^2)\epsilon^2 + 2l_0l_1\epsilon + l_0^2 = 1 + i\epsilon$$

For this to be true the coefficients of the powers of ϵ must match. The first being:

$$l_0^2 = 1$$

So

$$l_0 = \pm 1$$

The second must satisfy:

$$2l_0l_1 = i$$

So

$$l_1 = \begin{cases} \frac{i}{2} & \text{if } l_0 = 1 \\ -\frac{i}{2} & \text{if } l_0 = -1 \end{cases}$$

The ϵ^2 terms must satisfy:

$$2l_0l_2 + l_1^2 = 0$$

So

$$l_2 = \begin{cases} \frac{1}{8} & \text{if } l_0 = 1 \\ -\frac{1}{8} & \text{if } l_0 = -1 \end{cases}$$

So we have:

$$l = \begin{cases} 1 + \frac{i}{2}\epsilon + \frac{1}{8}\epsilon^2 \\ -1 - \frac{i}{2}\epsilon - \frac{1}{8}\epsilon^2 \end{cases}$$

Which back in the original variables is:

$$k = \begin{cases} \omega + \frac{i}{2} + \frac{1}{8\omega} \\ -\omega - \frac{i}{2} - \frac{1}{8\omega} \end{cases}$$

The behaviour of the real part is shown in Figure 2.3 and the behaviour of the imaginary part in Figure 2.4 where the black line is the full solution and the red line is this approximate solution.

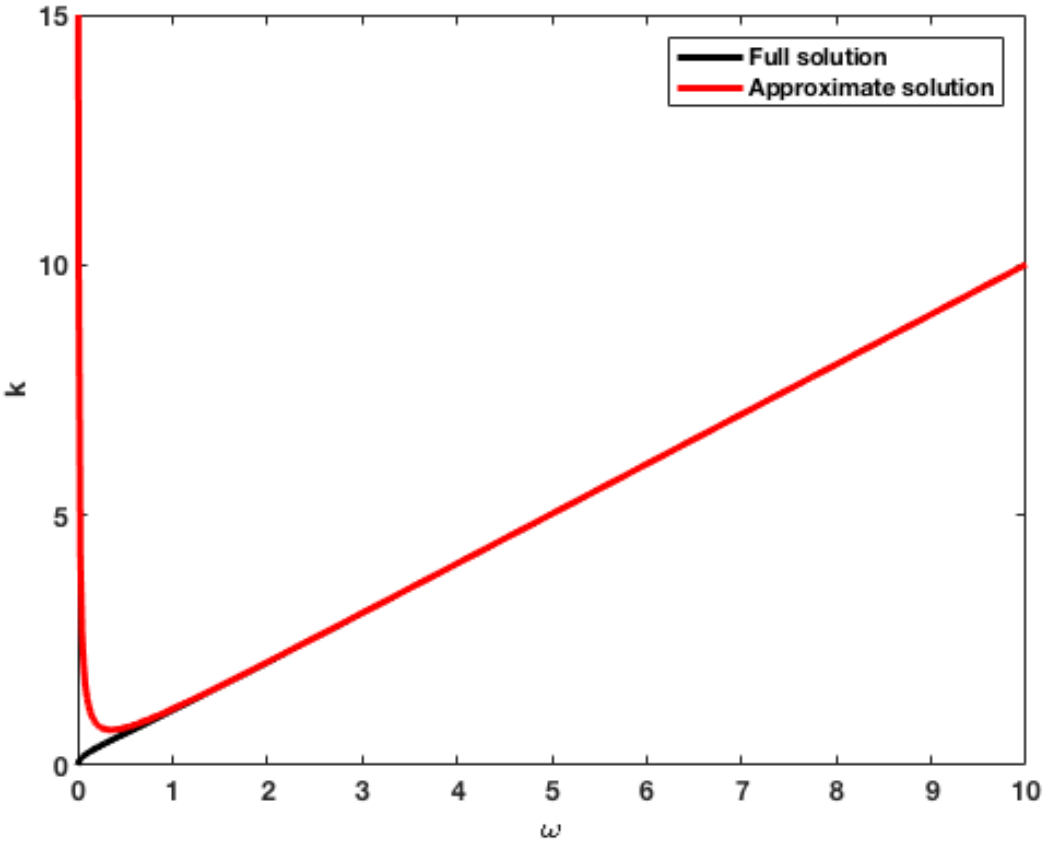

Figure 2.3: Plot of the real part of the high frequency limit approximation of $k(\omega)$. The red line is the approximate solution and the black line is the full solution for comparison.

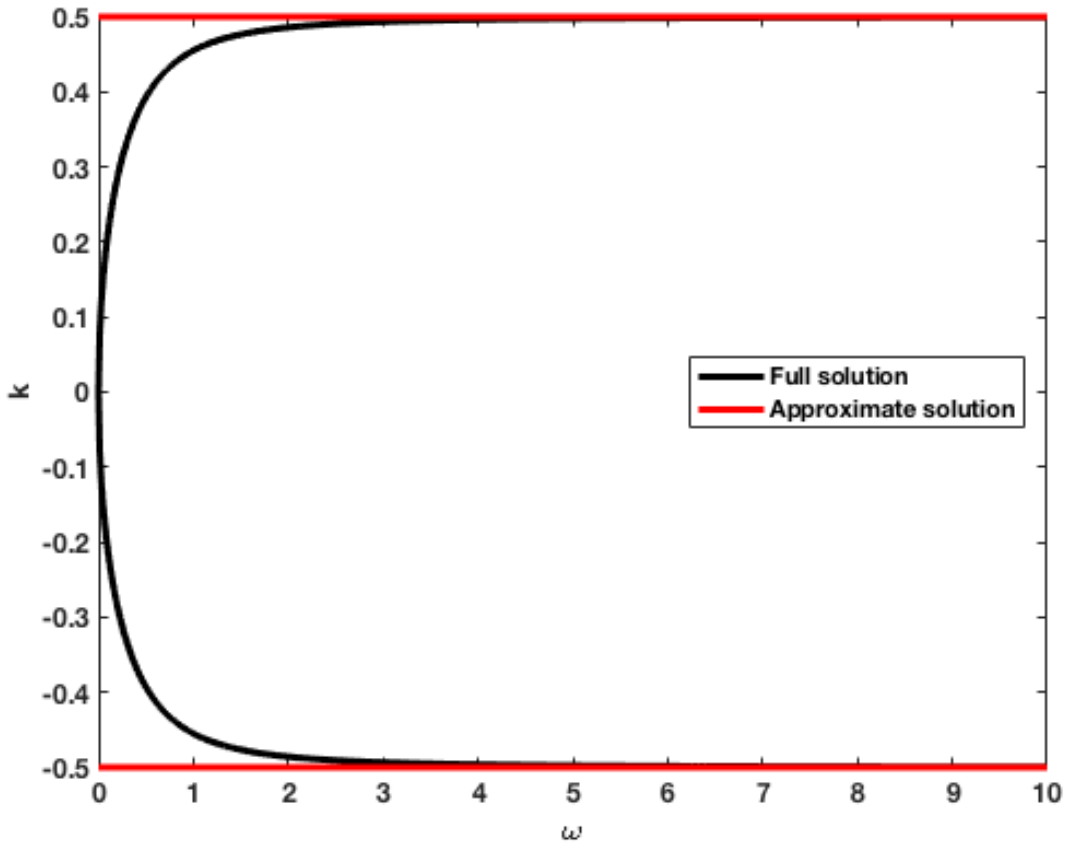

Figure 2.4: Plot of the imaginary part of the high frequency limit approximation of $k(\omega)$. The red line is the approximate solution and the black line is the full solution for comparison.

Clearly these approximations (shown in Figures 2.1, 2.2, 2.3, and 2.4) are very close to the true solution for their corresponding regions of ω. The full solution of the positive root can be seen in Figure 2.5 where the real part of the solution is shown in black and the imaginary part in red.

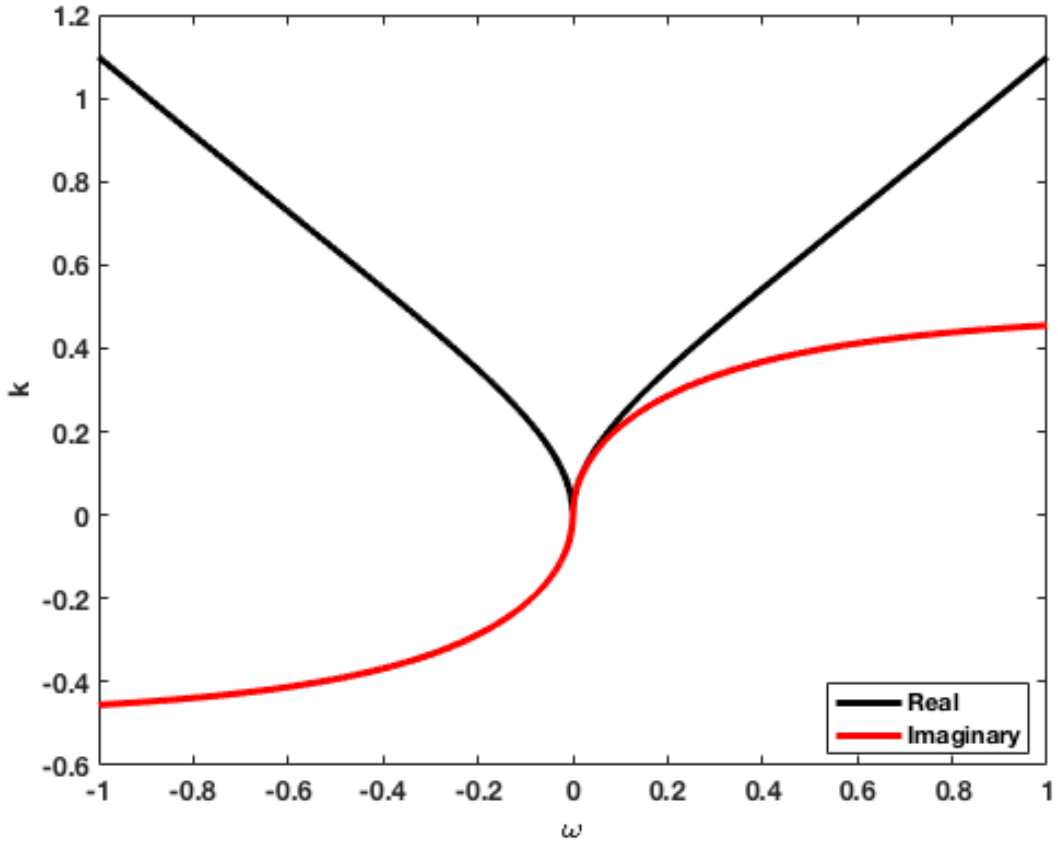

Figure 2.5: Plot of the positive root of k as a function of ω. The black line is the real part of k and the red line is the imaginary part of k.

In contrast, to get ω as a function of k:

$$\begin{aligned} 0 &= \omega(k)^2 + i\omega(k) - k^2 \\ \omega(k) &= \frac{-i \pm \sqrt{-1 + 4k^2}}{2} \\ &= \pm\frac{\sqrt{4k^2 - 1}}{2} - \frac{i}{2} \end{aligned}$$

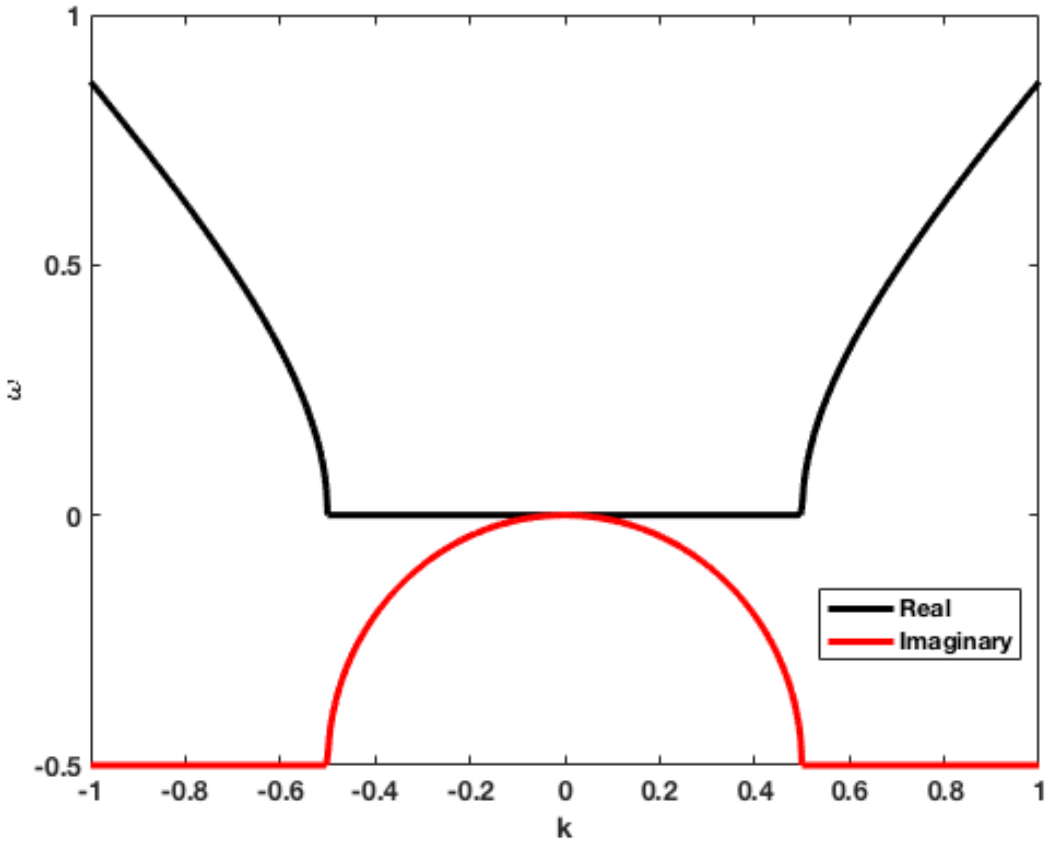

Figure 2.6: Plot of the positive root of ω as a function of k. The black line is the real part of ω and the red line is the imaginary part of ω.

Notice in Figure 2.6 the behaviour of the solution changes near $k = 0$ because when $k^2 < \frac{1}{4}$ the $\sqrt{4k^2 - 1}$ term becomes imaginary as well. When there is only an imaginary part of ω the wave does not propagate. In contrast, Figure 2.5 shows reasonably straightforward values for both the real and imaginary parts of $k(\omega)$ and there are no regions where propagation does not occur.

Taking a look at the dispersion of waves with set k values, Figure 2.7 shows a combination of short and long waves, specifically long waves with k values in the region of Figure 2.6 where the real part of ω disappears. Notice that while the short wave propagates forward before disappearing due to damping, the long wave does not propagate at all. Figure

2.8 shows how waves with different k values disperse at different rates. The top plot, with a k value of 0.3, shows faster dispersion than the middle plot (with $k = 0.075$) and the combination of the two waves in the bottom plot shows a dispersion speed between that of the two individual waves. Long waves (where $k < 0.05$, $c = 1$, $b = 0.1$) are shown in Figure 2.9 where it is clear that there is no propagation and the waves are only affected by damping.

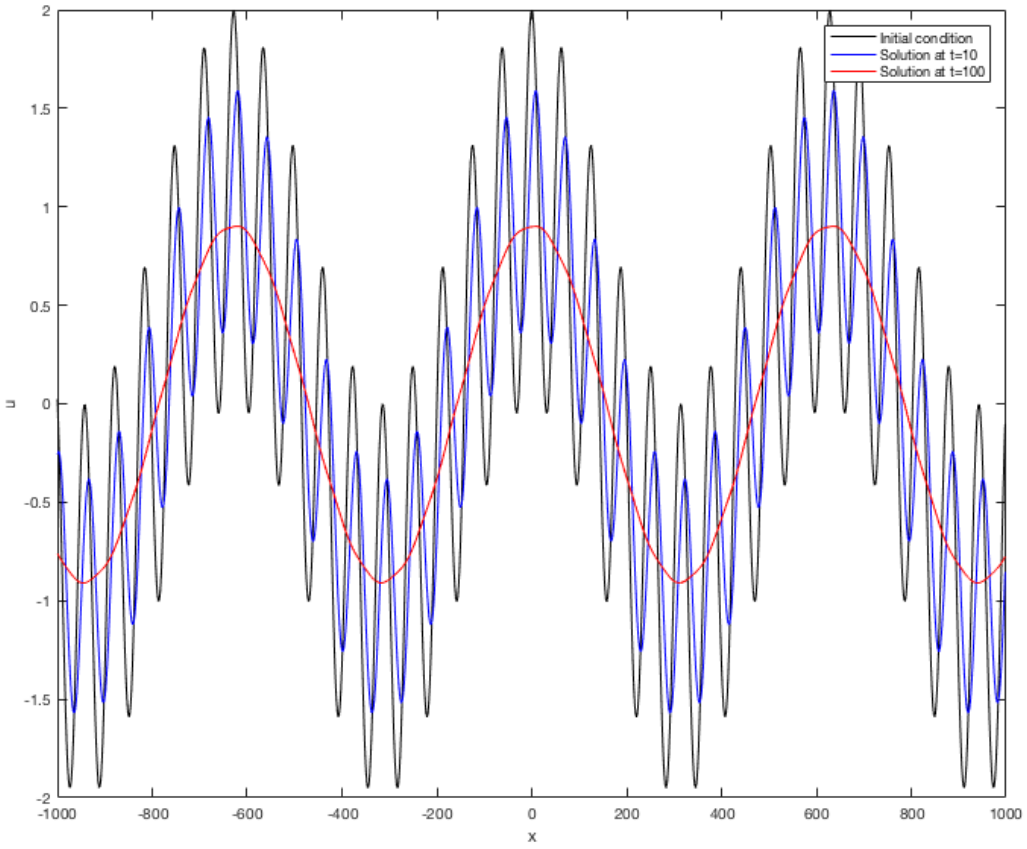

Figure 2.7: A combination of a short wave ($k_1 = 0.1$) and a long wave ($k_2 = 0.01$). The black shows the initial condition and the blue and red are progressive time steps. Parameters: $c = 1$, and $b = 0.1$

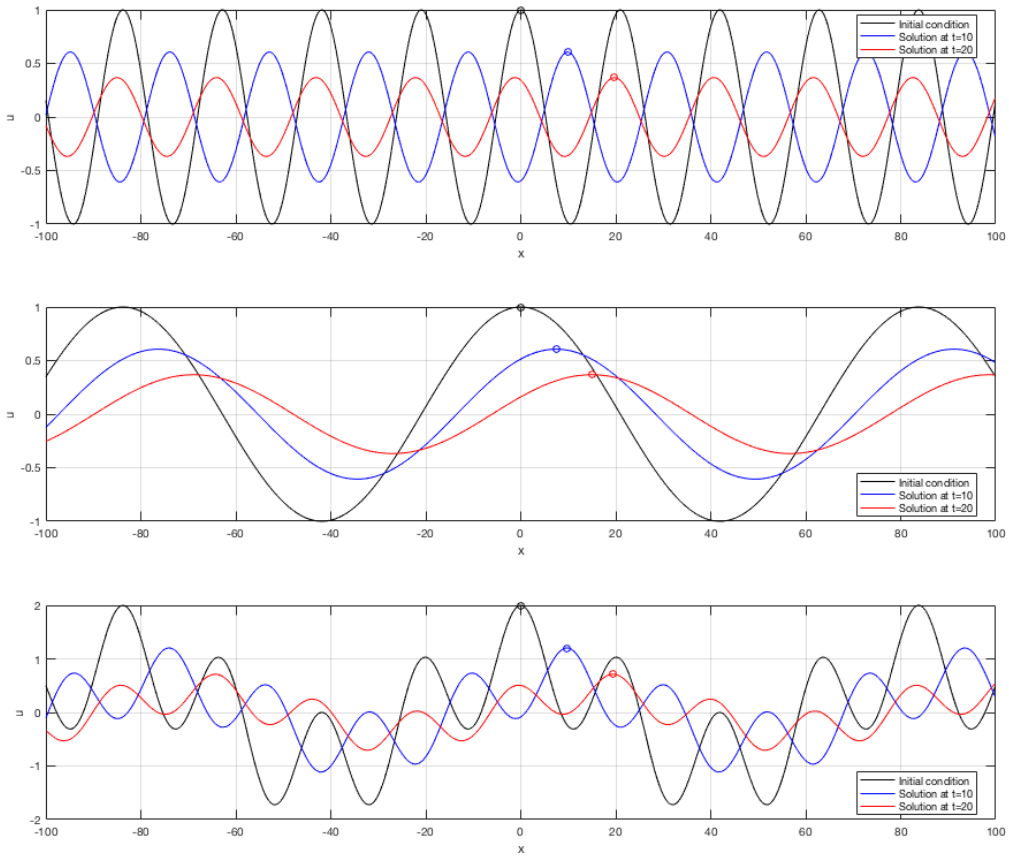

Figure 2.8: Dispersion of short waves ($k_1 = 0.3$, $k_2 = 0.075$). Top: a wave with k_1. Middle: a wave with k_2. Bottom: a combination of k_1 and k_2 waves. The black shows the initial condition and the blue and red are progressive time steps. Peaks of the wave starting at $x = 0$ are marked. Parameters: $c = 1$, and $b = 0.1$

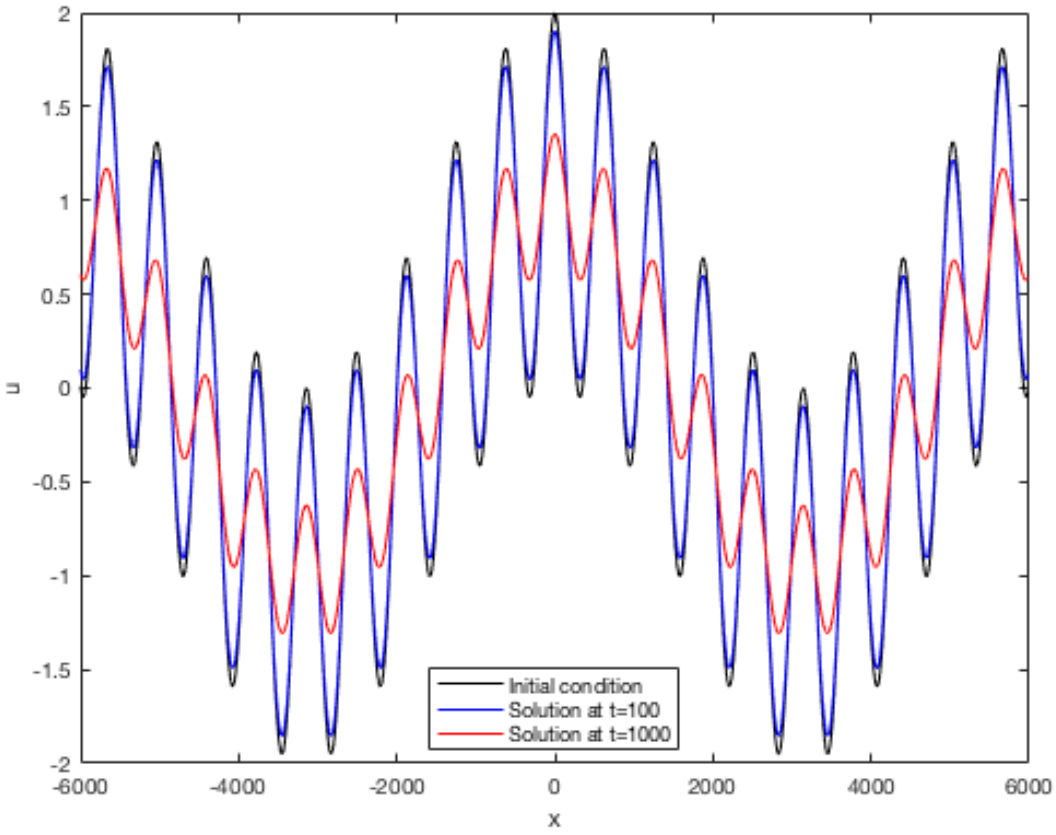

Figure 2.9: A combination of long waves ($k_1 = 0.01$, $k_2 = 0.001$). The black curve shows the initial condition and the blue and red curves are progressive time steps. Parameters: $c = 1$, and $b = 0.1$

2.1.3 Scattering

Wave scattering is a classical physical theory that considers the behaviour of waves at the interface between media with different physical properties [14]. The equations for linear acoustic waves without dissipation in a 1D continuum can be written as

$$\rho_0 u_{tt} = \tau_x \text{ with the constitutive law } \tau = \alpha u_x.$$

Figure 2.10 shows two different media meeting at $x = 0$, region 1 where $x < 0$ and

region 2 where $x > 0$. The parameters k_1, ρ_1 and α_1 apply in region 1 as the parameters k_2, ρ_2 and α_2 apply in region 2.

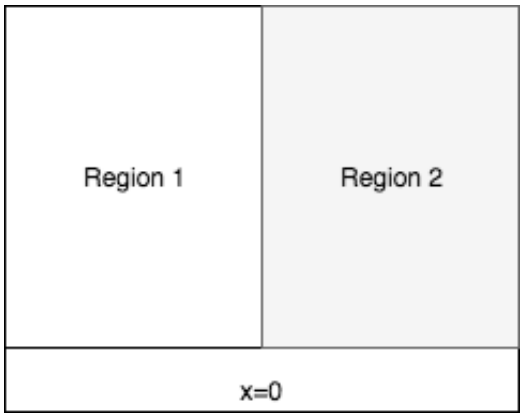

Figure 2.10: Two different media meeting at $x = 0$, region 1 where $x < 0$ and region 2 where $x > 0$

A wave traveling from left to right has an incident and reflected wave in region 1,

$$u_1(x,t) = e^{i(k_1 x - \omega t)} + Re^{i(-k_1 x - \omega t)}$$

and only a transmitted wave in region 2,

$$u_2(x,t) = Te^{i(k_2 x - \omega t)}.$$

The boundary conditions at $x = 0$ are:

$$\begin{aligned} u_1(0,t) &= u_2(0,t) \\ \tau_{1,x}(0,t) &= \tau_{2,x}(0,t) \end{aligned}$$

corresponding to a continuity of velocity and a continuity of force (i.e. stress). Working through to get relations for k_1 and k_2 with respect to ω, ρ_1, ρ_2, α_1 and, α_2:
Governing equation for region 1:

$$\begin{aligned} \rho_1 u_{1,tt} &= (\alpha_1 u_{1,x})_x \\ \rho_1(-\omega^2 u_1) &= \alpha_1(-k_1^2 u_1) \\ k_1 &= \pm\omega\sqrt{\frac{\rho_1}{\alpha_1}} \end{aligned}$$

Similarly, the governing equation for region 2:

$$\begin{aligned}\rho_2 u_{2,tt} &= (\alpha_2 u_{2,x})_x \\ \rho_2(-\omega^2 u_2) &= \alpha_2(-k_2^2 u_2) \\ k_2 &= \pm\omega\sqrt{\frac{\rho_2}{\alpha_2}}\end{aligned}$$

Applying the first BC:

$$\begin{aligned}u_1(0,t) &= u_2(0,t) \\ e^{-i\omega t} + Re^{-i\omega t} &= Te^{-i\omega t} \\ 1 + R &= T\end{aligned} \tag{2.8}$$

Applying the second BC:

$$\begin{aligned}\alpha_1 u_{1,x}(0,t) &= \alpha_2 u_{2,x}(0,t) \\ \alpha_1 ik_1 e^{-i\omega t} - \alpha_1 ik_1 Re^{-i\omega t} &= \alpha_2 ik_2 Te^{-i\omega t} \\ \alpha_1 k_1(1-R) &= \alpha_2 k_2 T\end{aligned} \tag{2.9}$$

Substituting 2.8 in 2.9:

$$\begin{aligned}\alpha_1 k_1(1-R) &= \alpha_2 k_2(1+R) \\ R &= \frac{\alpha_1 k_1 - \alpha_2 k_2}{\alpha_1 k_1 + \alpha_2 k_2}\end{aligned}$$

Substituting the result into 2.8:

$$T = 1 + \frac{\alpha_1 k_1 - k_2\alpha_2}{\alpha_1 k_1 + \alpha 2 k_2} = \frac{2\alpha_1 k_1}{\alpha_1 k_1 + \alpha_2 k_2}$$

So $k_1 = \pm\omega\sqrt{\frac{\rho_1}{\alpha_1}}$, $k_2 = \pm\omega\sqrt{\frac{\rho_2}{\alpha_2}}$, $R = \frac{\alpha_1 k_1 - k_2\alpha_2}{\alpha_1 k_1 + \alpha_2 k_2}$, and $T = \frac{2\alpha_1 k_1}{\alpha_1 k_1 + \alpha_2 k_2}$.

Shown in Figure 2.11 (included for completeness), both R and T are independent of ω once the dependence on k_1 and k_2 is addressed.

$$\begin{aligned}R &= \frac{\alpha_1 k_1 - k_2\alpha_2}{\alpha_1 k_1 + \alpha_2 k_2} \\ &= \frac{\pm\alpha_1\omega\sqrt{\frac{\rho_1}{\alpha_1}} \mp \omega\sqrt{\frac{\rho_2}{\alpha_2}}\alpha_2}{\pm\alpha_1\omega\sqrt{\frac{\rho_1}{\alpha_1}} \pm \alpha_2\omega\sqrt{\frac{\rho_2}{\alpha_2}}} \\ &= \frac{\pm\sqrt{\alpha_1\rho_1} \mp \sqrt{\alpha_2\rho_2}}{\pm\sqrt{\alpha_1\rho_1} \pm \sqrt{\alpha_2\rho_2}}\end{aligned}$$

And

$$\begin{aligned} T &= \frac{2\alpha_1 k_1}{\alpha_1 k_1 + \alpha_2 k_2} \\ &= \frac{\pm 2\alpha_1 \omega \sqrt{\frac{\rho_1}{\alpha_1}}}{\pm \alpha_1 \omega \sqrt{\frac{\rho_1}{\alpha_1}} \pm \alpha_2 \omega \sqrt{\frac{\rho_2}{\alpha_2}}} \\ &= \frac{\pm 2\sqrt{\alpha_1 \rho_1}}{\pm \sqrt{\alpha_1 \rho_1} \pm \sqrt{\alpha_2 \rho_2}} \end{aligned}$$

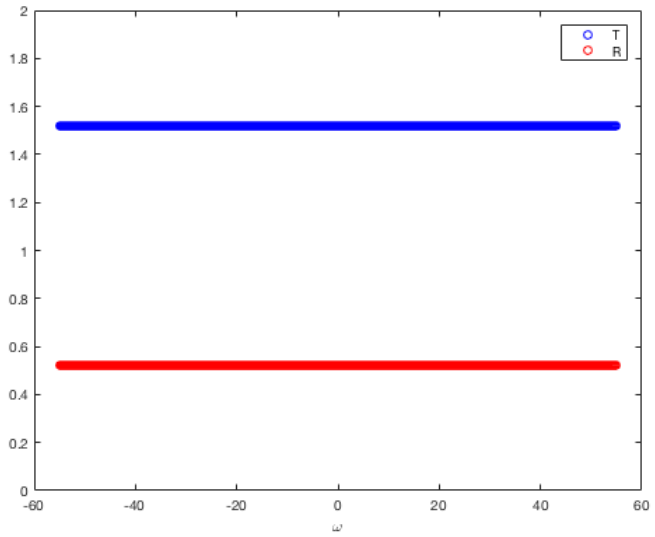

Figure 2.11: How the coefficients R and T vary (or don't) with respect to ω with constants $\alpha_1 = 1$ and $\alpha_2 = 0.1$ (and $\rho_1 = \rho_2 = 1$)

Figure 2.12 shows how R and T vary with respect to ρ_1. Figure 2.13 shows the same but for ρ_2. Figure 2.14 and Figure 2.15 show how R and T vary with respect to α_1 and α_2 respectively.

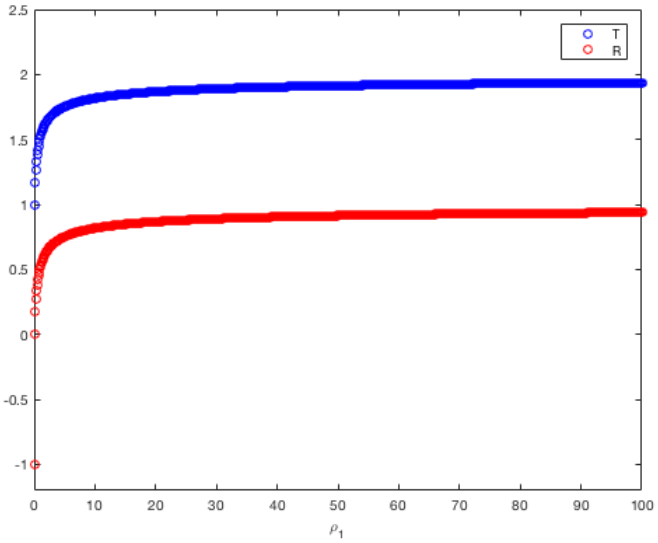

Figure 2.12: The coefficients R and T with varying ρ_1 and constant $\alpha_1 = 1$, $\alpha_2 = 0.1$ and $\rho_2 = 1$

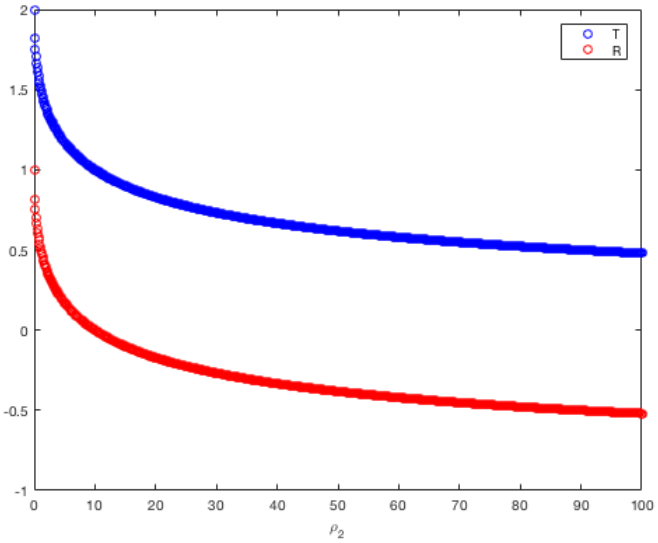

Figure 2.13: The coefficients R and T with varying ρ_2 and constant $\alpha_1 = 1$, $\alpha_2 = 0.1$ and $\rho_1 = 1$

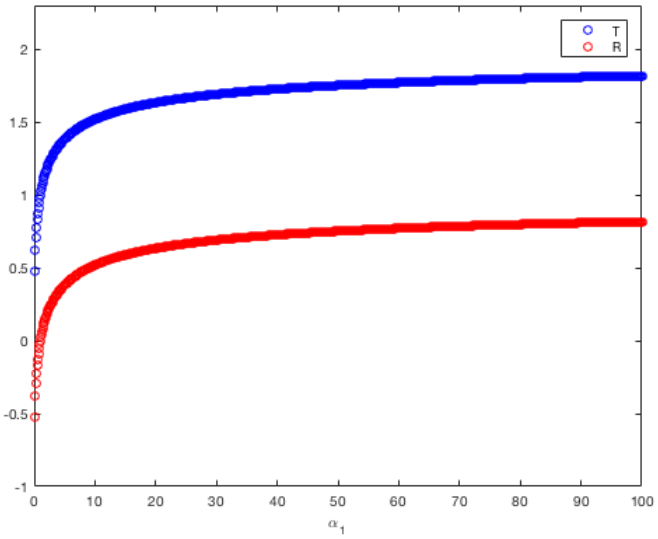

Figure 2.14: The coefficients R and T with varying α_1 and constant $\rho_1 = 1$, $\rho_2 = 1$ and $\alpha_2 = 1$

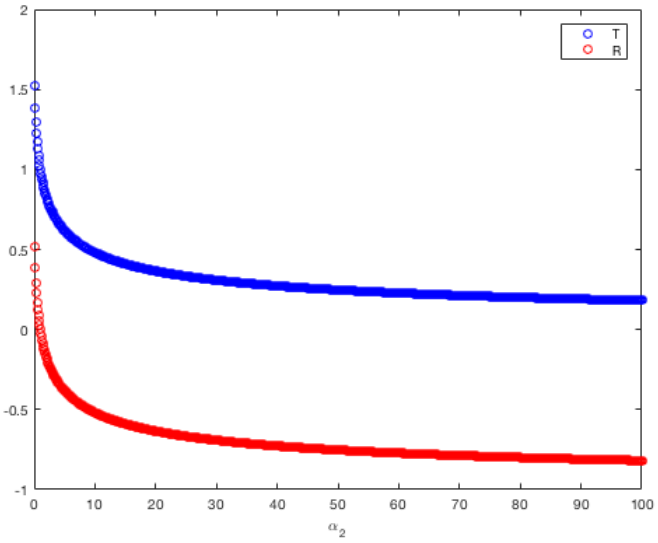

Figure 2.15: The coefficients R and T with varying α_2 and constant $\rho_1 = 1$, $\rho_2 = 1$ and $\alpha_1 = 1$

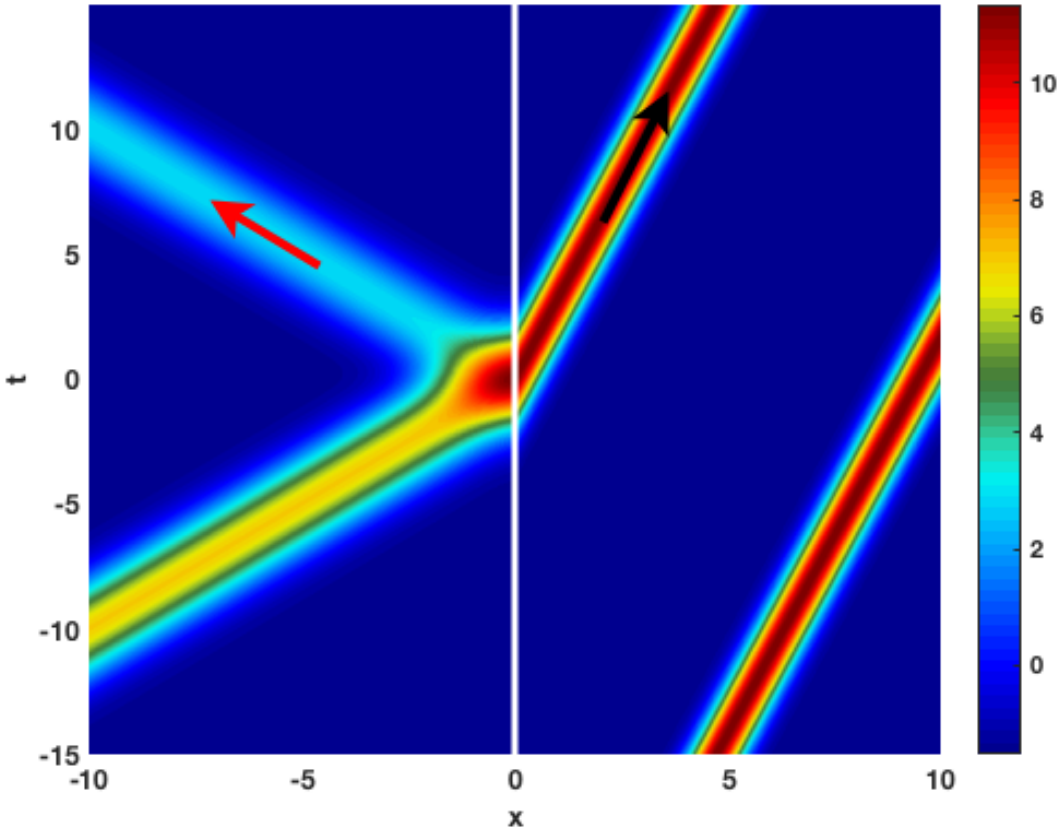

Figure 2.16: The incident and reflected waves (red arrow) in $x < 0$ and the transmitted waves (black arrow) in $x > 0$ with $\alpha_1 = 1$, $\alpha_2 = 0.1$, and $\rho_1 = \rho_2 = 1$).

It is a bit difficult to visualize scattering in 1D, even though this is the case that allows for the easiest analytical analysis. To illustrate the effect of scattering, Figure 2.16 depicts the continuity but non-differentiability of the wave solution at the $x = 0$ boundary between the regions. Note the reflected waves highlighted with the red arrow as well as the transmitted refracted waves marked with the black arrow. The bottom transmitted wave appears because of the periodicity of the solution, it is the remains of an earlier wave.

Now including absorption in region 2 ($x > 0$):

Equation for region 2 is:

$$\rho u_{tt} + b u_t = \tau_x$$

Boundary conditions are still:

$$\begin{aligned} u_1(0,t) &= u_2(0,t) \\ \tau_{1,x}(0,t) &= \tau_{2,x}(0,t) \end{aligned}$$

Governing equation for region 1:

$$\begin{aligned} \rho_1 u_{1,tt} &= (\alpha_1 u_{1,x})_x \\ \rho_1(-\omega^2 u_1) &= \alpha_1(-k_1^2 u_1) \\ k_1 &= \pm\omega\sqrt{\frac{\rho_1}{\alpha_1}} \end{aligned}$$

Similarly, the governing equation for region 2:

$$\begin{aligned} \rho_2 u_{2,tt} + b u_{2,t} &= (\alpha_2 u_{2,x})_x \\ \rho_2(-\omega^2 u_2) + b(-i\omega)u_2 &= \alpha_2(-k_2^2 u_2) \\ \rho_2\omega^2 + ib\omega &= \alpha_2 k_2^2 \\ k_2^2 &= \frac{\rho_2\omega^2}{\alpha_2} + \frac{ib\omega}{\alpha_2} \\ k_2^2 &= \sqrt{\frac{\rho_2^2\omega^4}{\alpha_2^2} + \frac{b^2\omega^2}{\alpha_2^2}}e^{i\theta} \\ \text{where } \theta &= \arctan\left(\frac{b}{\rho_2\omega}\right), \arctan\left(\frac{b}{\rho_2\omega}\right) + \pi \\ k_2 &= \pm\left(\frac{\rho_2^2\omega^4}{\alpha_2^2} + \frac{b^2\omega^2}{\alpha_2^2}\right)^{\frac{1}{4}} e^{\frac{i\theta}{2}} \end{aligned}$$

Applying the first BC:

$$\begin{aligned} u_1(0,t) &= u_2(0,t) \\ e^{-i\omega t} + Re^{-i\omega t} &= Te^{-i\omega t} \end{aligned}$$

$$1 + R = T \tag{2.10}$$

Applying the second BC:

$$\begin{aligned} \alpha_1 u_{1,x}(0,t) &= \alpha_2 u_{2,x}(0,t) \\ \alpha_1 i k_1 e^{-i\omega t} - \alpha_1 i k_1 R e^{-i\omega t} &= \alpha_2 i k_2 T e^{-i\omega t} \end{aligned}$$

$$\alpha_1 k_1 (1 - R) = \alpha_2 k_2 T \tag{2.11}$$

Substituting 2.10 in 2.11:

$$\begin{aligned} \alpha_1 k_1 (1 - R) &= \alpha_2 k_2 (1 + R) \\ R &= \frac{\alpha_1 k_1 - \alpha_2 k_2}{\alpha_1 k_1 + \alpha_2 k_2} \end{aligned}$$

Substituting the result into 2.10:

$$T = 1 + \frac{\alpha_1 k_1 - k_2 \alpha_2}{\alpha_1 k_1 + \alpha 2 k_2} = \frac{2\alpha_1 k_1}{\alpha_1 k_1 + \alpha_2 k_2}$$

So $k_1 = \pm\omega\sqrt{\frac{\rho_1}{\alpha_1}}$, $k_2 = \pm\left(\frac{\rho_2^2\omega^4}{\alpha_2^2} + \frac{b^2\omega^2}{\alpha_2^2}\right)^{\frac{1}{4}} e^{\frac{i\theta}{2}}$ (where $\theta = \arctan\left(\frac{b}{\rho_2\omega}\right)$, $\arctan\left(\frac{b}{\rho_2\omega}\right)+\pi$), $R = \frac{\alpha_1 k_1 - k_2\alpha_2}{\alpha_1 k_1 + \alpha 2 k_2}$, and $T = \frac{2\alpha_1 k_1}{\alpha_1 k_1 + \alpha_2 k_2}$.

This time, addressing the dependence of R and T on k_1 and k_2 gives:

$$\begin{aligned} R &= \frac{\alpha_1 k_1 - k_2 \alpha_2}{\alpha_1 k_1 + \alpha 2 k_2} \\ &= \frac{\pm\alpha_1\omega\sqrt{\frac{\rho_1}{\alpha_1}} \mp \alpha_2\left(\frac{\rho_2^2\omega^4}{\alpha_2^2} + \frac{b^2\omega^2}{\alpha_2^2}\right)^{\frac{1}{4}} e^{i\frac{\theta}{2}}}{\pm\alpha_1\omega\sqrt{\frac{\rho_1}{\alpha_1}} \pm \alpha_2\left(\frac{\rho_2^2\omega^4}{\alpha_2^2} + \frac{b^2\omega^2}{\alpha_2^2}\right)^{\frac{1}{4}} e^{i\frac{\theta}{2}}} \\ &= \frac{\pm\omega\sqrt{\alpha_1\rho_1} \mp \sqrt{\alpha_2}\left(\rho_2^2\omega^4 + b^2\omega^2\right)^{\frac{1}{4}} e^{i\frac{\theta}{2}}}{\pm\omega\sqrt{\alpha_1\rho_1} \pm \sqrt{\alpha_2}\left(\rho_2^2\omega^4 + b^2\omega^2\right)^{\frac{1}{4}} e^{i\frac{\theta}{2}}} \\ &= \frac{\pm\sqrt{\alpha_1\rho_1} \mp \sqrt{\alpha_2}\left(\rho_2^2 + \frac{b^2}{\omega^2}\right)^{\frac{1}{4}} e^{i\frac{\theta}{2}}}{\pm\sqrt{\alpha_1\rho_1} \pm \sqrt{\alpha_2}\left(\rho_2^2 + \frac{b^2}{\omega^2}\right)^{\frac{1}{4}} e^{i\frac{\theta}{2}}} \end{aligned}$$

And similarly

$$T = \frac{2\alpha_1 k_1}{\alpha_1 k_1 + \alpha_2 k_2}$$
$$= \frac{\pm 2\sqrt{\alpha_1 \rho_1}}{\pm\sqrt{\alpha_1 \rho_1} \pm \sqrt{\alpha_2}\left(\rho_2^2 + \frac{b^2}{\omega^2}\right)^{\frac{1}{4}} e^{i\frac{\theta}{2}}}$$

And considering that $\theta = \arctan\left(\frac{b}{\rho_2 \omega}\right)$, $\arctan\left(\frac{b}{\rho_2 \omega}\right) + \pi$, R and T will have some dependence on frequency ω unless the damping is $b(\omega) = \text{constant} \times \omega$.

Figures 2.17, 2.18, 2.19, 2.20 and 2.21 include absorption in Region 2 and correspond to Figures 2.11, 2.12, 2.13, 2.14 and 2.15.

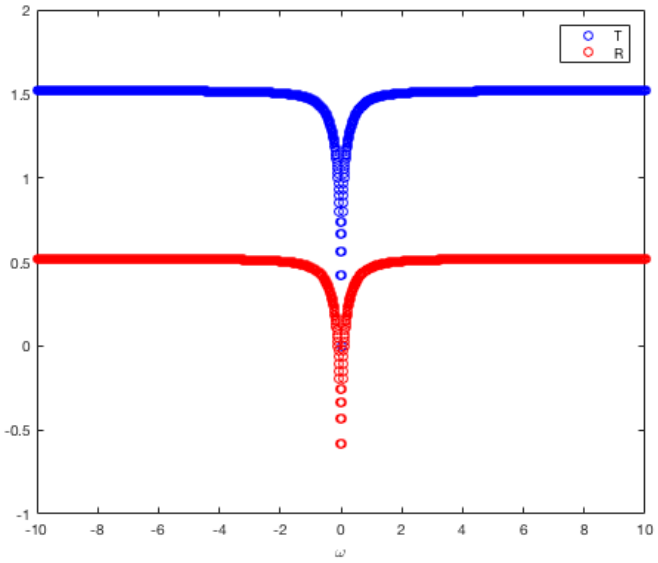

Figure 2.17: The real part of the coefficients R and T with varying ω and constant $b = 1$, $\alpha_1 = 1$, $\alpha_2 = 0.1$, $\rho_1 = 1$ and $\rho_2 = 1$

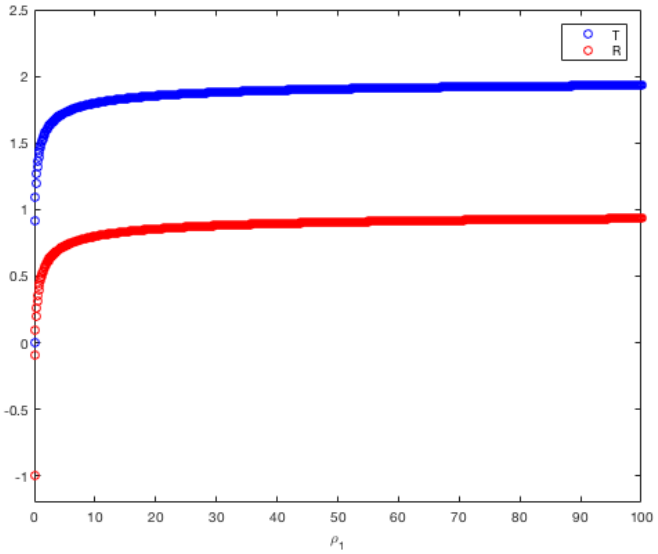

Figure 2.18: The real part of the coefficients R and T with varying ρ_1 and constant $b = 1$, $\omega = 1$, $\alpha_1 = 1$, $\alpha_2 = 0.1$ and $\rho_2 = 1$

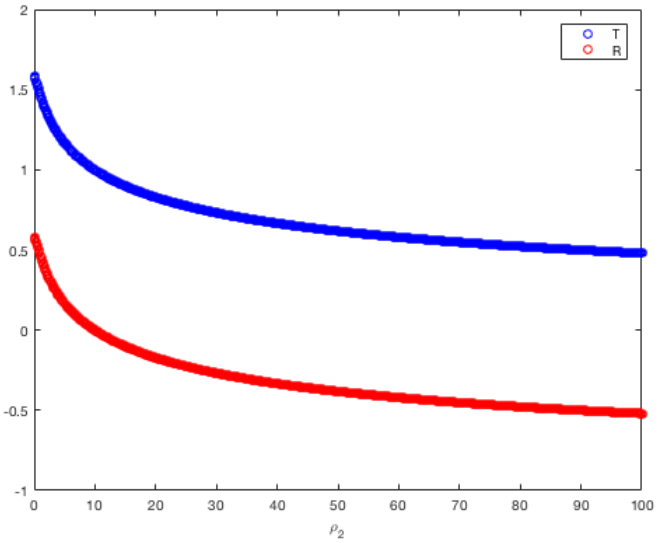

Figure 2.19: The real part of the coefficients R and T with varying ρ_2 and constant $b = 1$, $\omega = 1$, $\alpha_1 = 1$, $\alpha_2 = 0.1$ and $\rho_1 = 1$

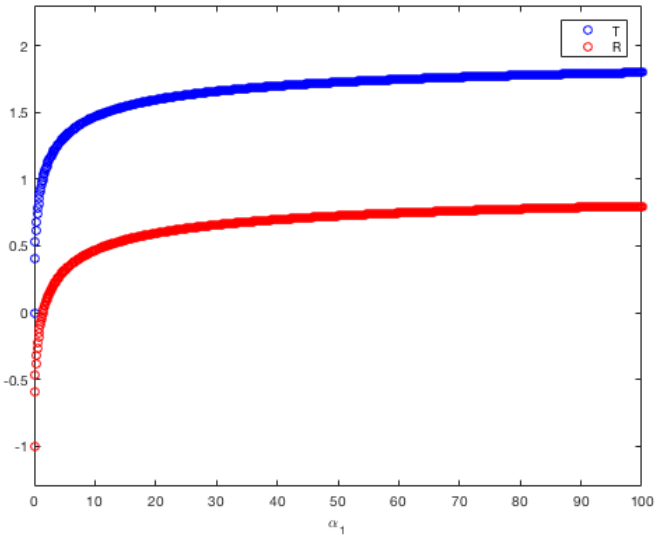

Figure 2.20: The real part of the coefficients R and T with varying α_1 and constant $b = 1$, $\omega = 1$, $\rho_1 = 1$, $\rho_2 = 1$ and $\alpha_2 = 1$

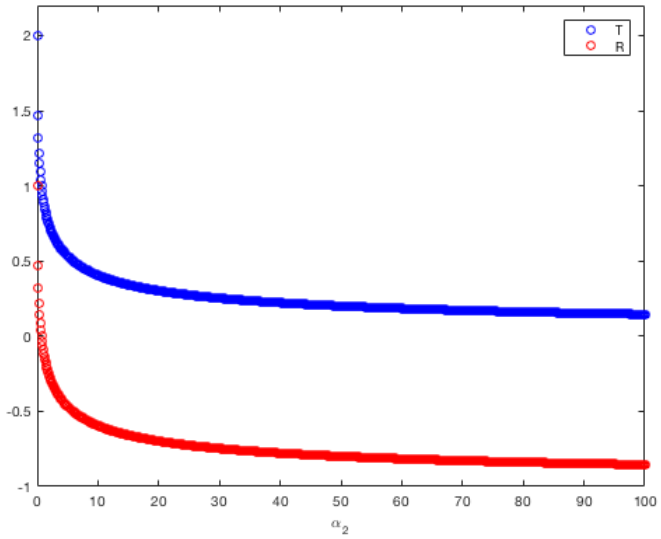

Figure 2.21: The real part of the coefficients R and T with varying α_2 and constant $b = 1$, $\omega = 1$, $\rho_1 = 1$, $\rho_2 = 1$ and $\alpha_1 = 1$

The behaviours of the real parts of R and T are similar to the previous values found for these coefficients but with small differences between cases. The exception is Figure 2.17 where a much larger difference can be seen in comparison to Figure 2.11. Note that including absorption in region 2 leads to complex values of R and T, whereas everything was real valued without absorption.

2.2 Driven Half Space Problem

In the case of spatially uniform properties (such as sound speed and absorption constant) the Fourier transform can be used to transform problems to Fourier space where an analytical solution may be found. The resulting expressions can then be transformed numerically to physical space. Begin with the governing equation in 1D,

$$u_{tt} + bu_t = c^2 u_{xx} + f(x,t)$$

Using the wave ansatz

$$u(x,t) = e^{i(kx-\omega t)}$$

the 2D Fourier transform gives:

$$-\omega^2 U - i\omega b U = -k^2 c^2 U + F(k,\omega)$$

The unforced problem gives the relation:

$$-\omega^2 - i\omega b = -k^2 c^2$$
$$k^2 = \frac{\omega^2 + i\omega b}{c^2}$$

Using this relation to get two values for k:

$$k_1 = \frac{\sqrt{|\omega|}}{c}\left(\omega^2 + b^2\right)^{\frac{1}{4}} \exp\left(\frac{i \arctan\left(\frac{b}{\omega}\right)}{2}\right)$$
$$k_2 = \frac{\sqrt{|\omega|}}{c}\left(\omega^2 + b^2\right)^{\frac{1}{4}} \exp\left(\frac{i\left(\arctan\left(\frac{b}{\omega}\right) + \pi\right)}{2}\right)$$

k is chosen such that its imaginary part is greater than zero, ensuring the wave decays as x grows. So a solution is constructed using the Fourier transform of the forcing to provide the amplitudes of the waves:

$$u_n = \mathbb{R}(\text{amplitude} \times e^{i(\omega_n t - k_m x)})$$

where the full solution is the sum of the u_n and $\omega_n \in$(a defined set of values for temporal frequency) and each k_m is decided such that the wave stays bounded.

To demonstrate, here are two sample forcing functions:

$$f_1 = \exp\left[-\left(\frac{t}{t_0}\right)^2\right] \cos\left(\frac{2\pi t}{T_1}\right)$$

$$f_2 = \exp\left[-\left(\frac{t}{t_0}\right)^2\right] \cos\left(\frac{2\pi t}{T_2} + \epsilon\right)$$

where ϵ is a small phase shift to avoid overlays leading to massive resonance.

And the superposition of the two sample forcing functions is simply:

$$f_3 = f_1 + f_2$$

Figure 2.22 shows these forcing functions and Figures 2.23, 2.24, and 2.25 show the results of the forcing functions f_1, f_2, and f_3 respectively.

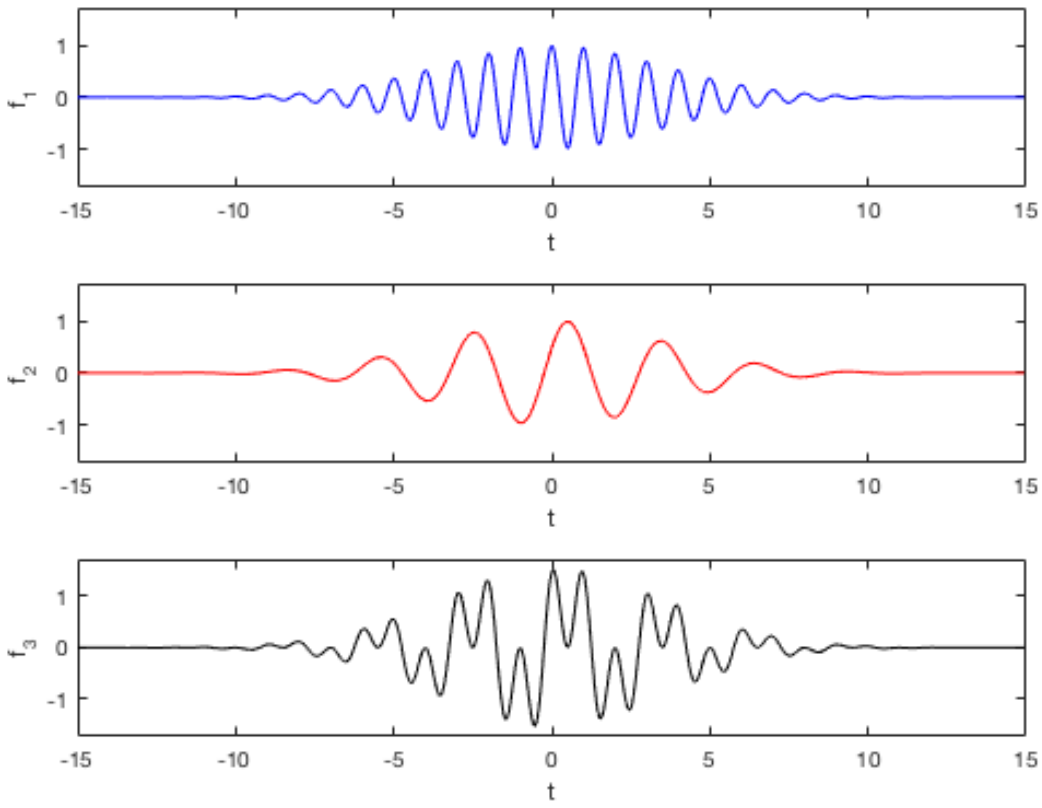

Figure 2.22: The forcing functions f_1, f_2, and f_3 (which is a superposition of f_1 and f_2). With $t_0 = 5$, $T_1 = 1$, and $T_2 = 3$

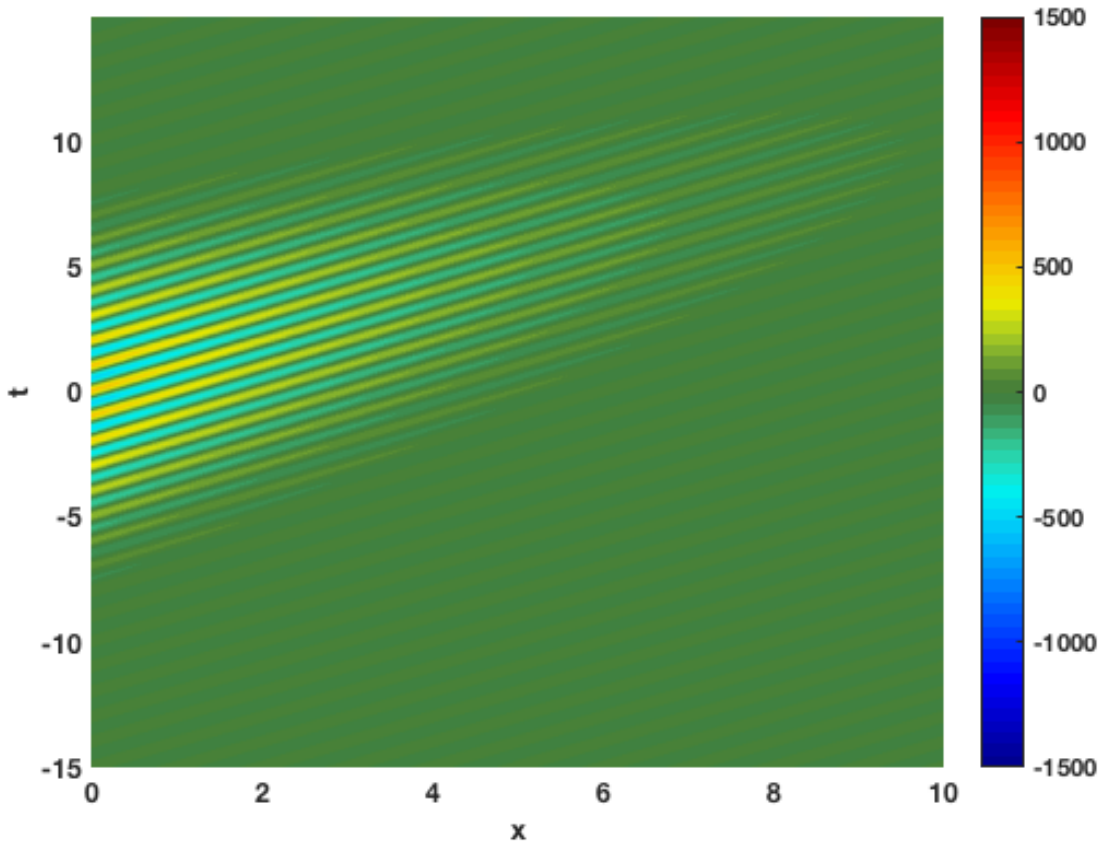

Figure 2.23: Results of f_1 with constant damping. With $t_0 = 5$, $T_1 = 1$, and $b = 0.5$

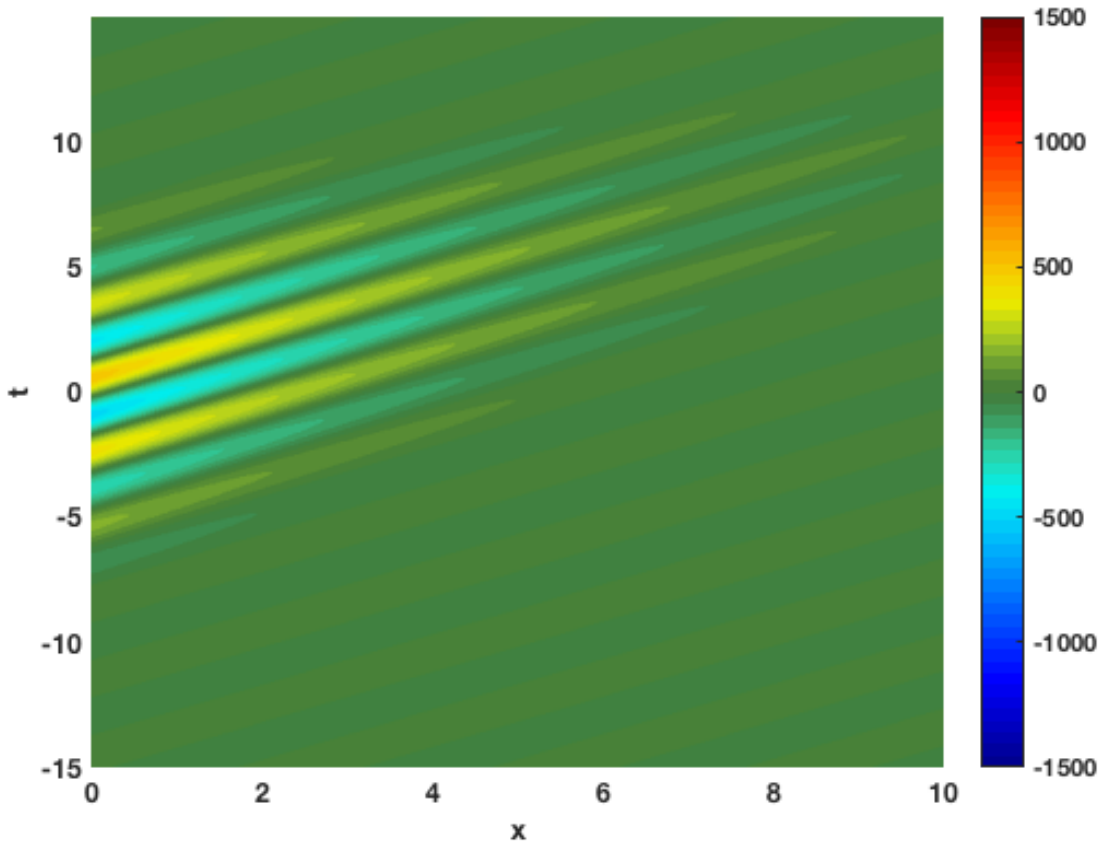

Figure 2.24: Results of f_2 with constant damping. With $t_0 = 5$, $T_2 = 3$, and $b = 0.5$

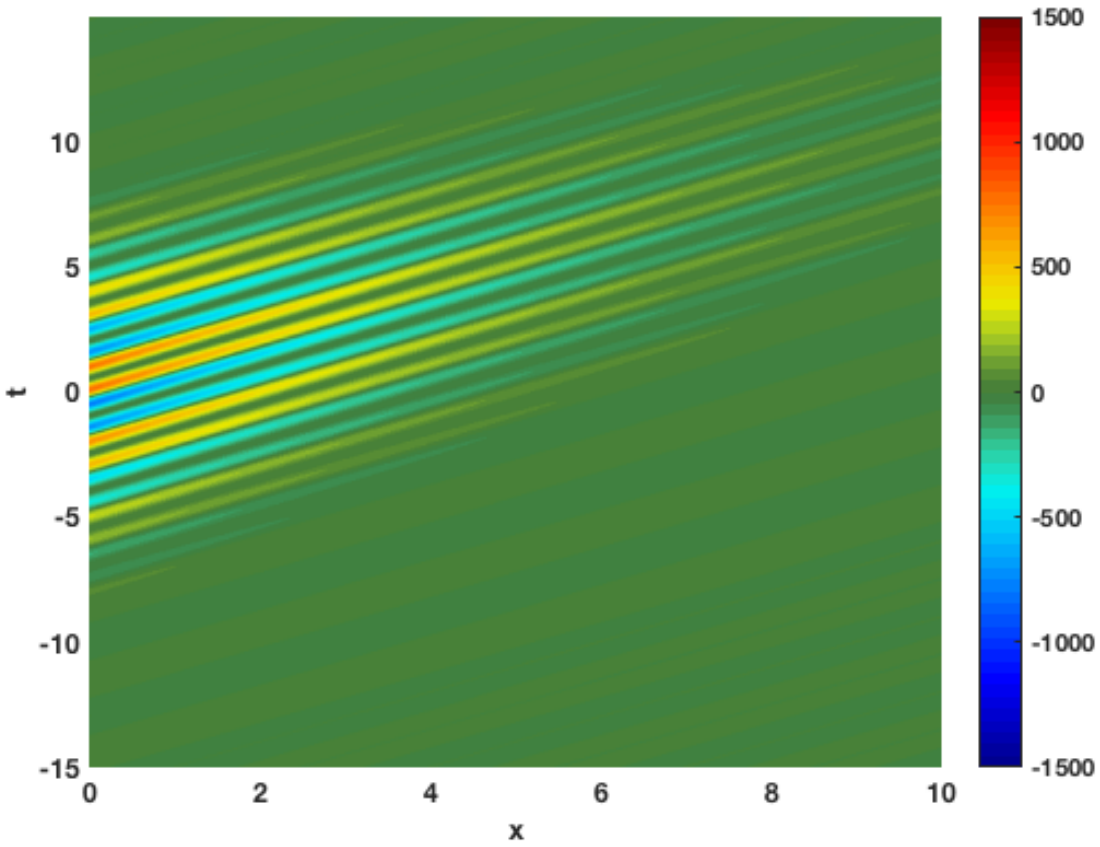

Figure 2.25: Results of f_3, the superposition of f_1 and f_2, with constant damping. With $t_0 = 5$, $T_1 = 1$, $T_2 = 3$, and $b = 0.5$

2.2.1 Frequency Dependent Damping

In tissue sound absorption depends on frequency [1, 17]. Adapting the model appropriately, the damping coefficient b now depends on frequency, $b(\omega)$. Figure 2.26 shows a case using constant damping. Figure 2.27 shows the same forcing but instead of the constant damping, damping is larger for higher frequencies. Figure 2.28 again uses the same forcing but this time the damping is larger for lower frequencies.

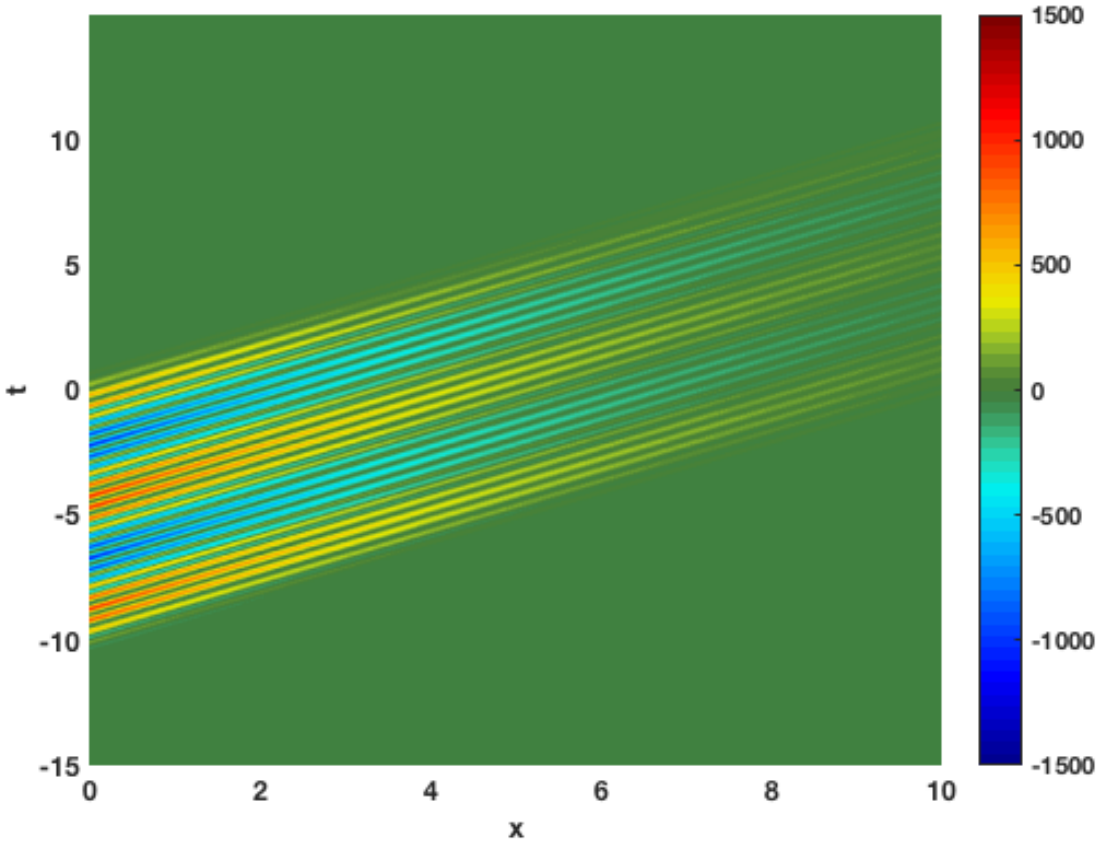

Figure 2.26: Constant damping coefficient b

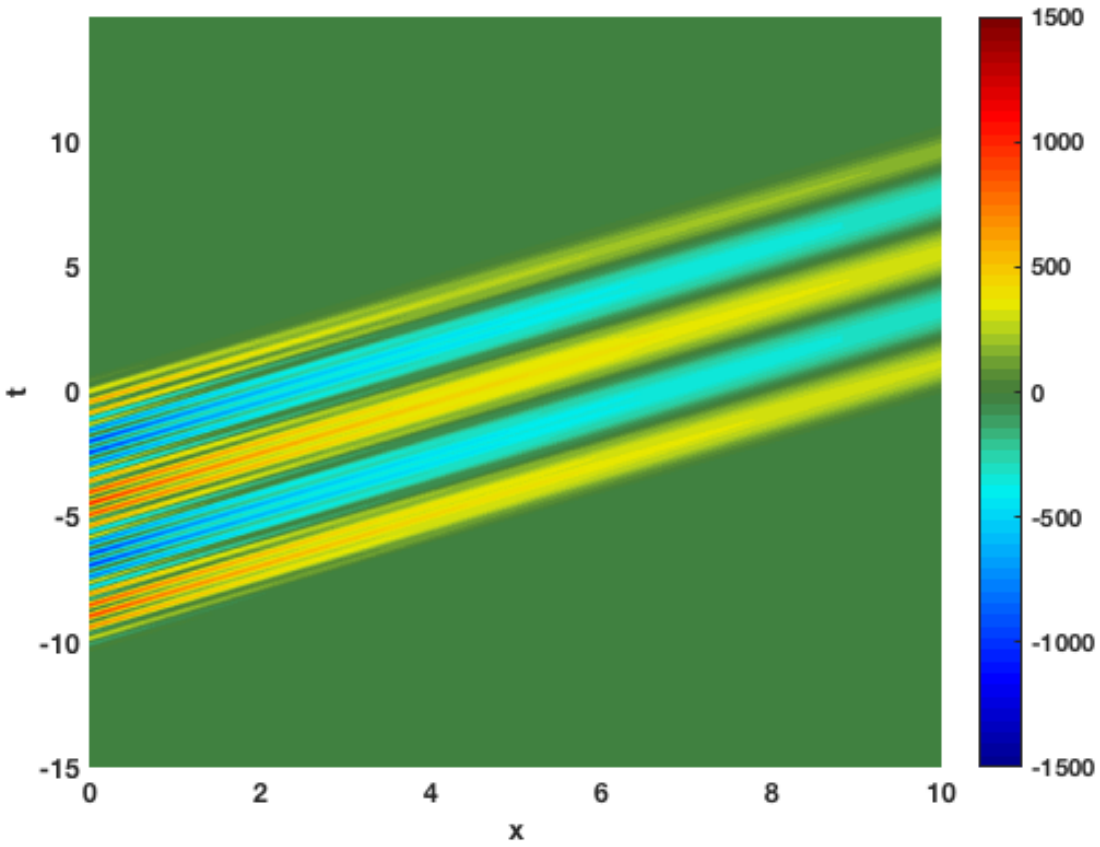

Figure 2.27: Damping coefficient $b(\omega)$ is greater for higher frequencies

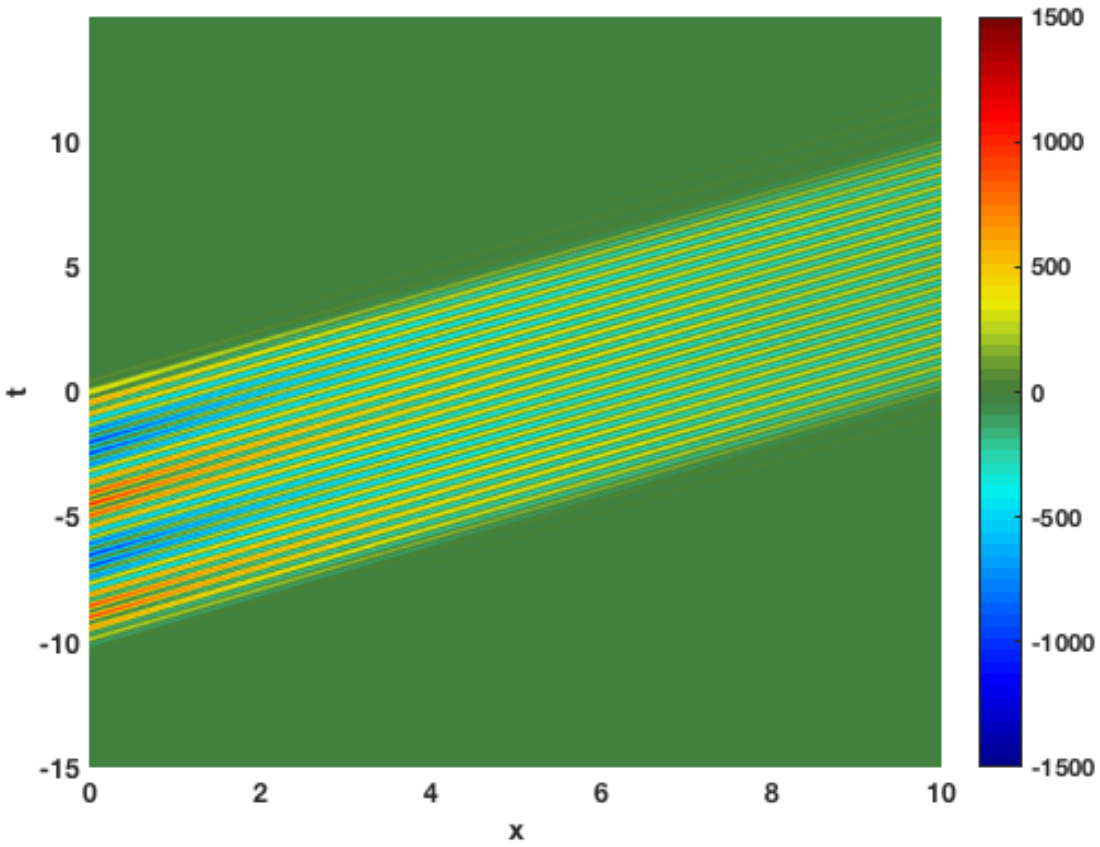

Figure 2.28: Damping coefficient $b(\omega)$ is greater for lower frequencies

2.3 Numerical Methods

The previous sections have develop at least some understanding of the phenomenology of waves in a medium with variable properties, including absorption. In this section we turn to the numerical methods used in the remainder of the thesis to carry out simulations. The governing equations for these simulations are linear, but they are not necessarily constant coefficient. For the purposes of exposition it is worth beginning with the constant coefficient case:

$$u_{tt} + bu_t = c^2 u_{xx}$$

If we take the Fourier transform we get an ordinary differential equation for the transformed variable

$$\bar{u}_{tt} + b\bar{u}_t = -c^2k^2\bar{u}.$$

In the discretized case on a grid the wavenumber is discretized as well, but the essential facts remain unchanged. The ODE can be solved by a number of methods, but for the simulations the second order in time leapfrog method is adopted [9].

When the properties of the medium vary in space we can write the 1D equation without damping as

$$\rho_0 u_{tt} = (T(x)u_x)_x$$

Using the superscript $u^{(n)}$ to denote the u field at the nth time step we can write the time-stepping as

$$\rho_0 \frac{u^{(n+1)} - 2u^{(n)} + u^{(n-1)}}{\Delta t^2} = \text{iFFT}[ik\text{FFT}(T(x)\text{iFFT}[ik\text{FFT}(u^{(n)})])].$$

Here FFT denotes the Fast Fourier Transform and iFFT denotes its inverse. The scheme outlined is an explicit method since it can be rearranged to give a formula for $u^{(n+1)}$. The extension to the variable damping case is straightforward, as is the extension to two dimensions, since the FFT2 command in Matlab provides a built in way to handle the two dimensional Fourier transform. The following code listing provides an example of the code implementation in Matlab.

```
%spatial derivatives of c
cx = real(ifft2(1i*k.*fft2(c)));
cy = real(ifft2(1i*l.*fft2(c)));
%factor doesn't change so set it once now
factlh=1./(1+myb/2*dt);
for ii=1:numouts
   for jj=1:numsteps
      %step time forward
      t=t+dt;
      %first spatial derivatives of pressure using fft2
      pnx = real(ifft2(1i*k.*fft2(pn)));
      pny = real(ifft2(1i*l.*fft2(pn)));
      %laplacian of pressure using fft2
      pnl = real(ifft2(lap.*fft2(pn)));
      %laplacian of cn
```

```
      cnl = real(ifft2(lap.*fft2(cn)));
      % next step in p using explicit time stepping
      pf = factlh.*(2*pn - (1-myb/2*dt).*pp + dt2*(cx.*pnx+cy.*pny+c.*pnl));
      %update cn
      cn=cn+conv_factor*pn.^2+dt*kappa*cnl;
      %update p_past, p_now
      pp = pn;
      pn = pf;
   end
end
```

While the technique above is standard, care was taken to ensure that results reported were independent of grid doubling or halving. Given the difficulty of in vivo measurements, it is expected that the accuracy of spectral methods is considerably higher than that of measurements.

2.4 Spatially Variable Medium

As shown in Figure 2.29 an obstacle in the path of a wave leads to interaction patterns.

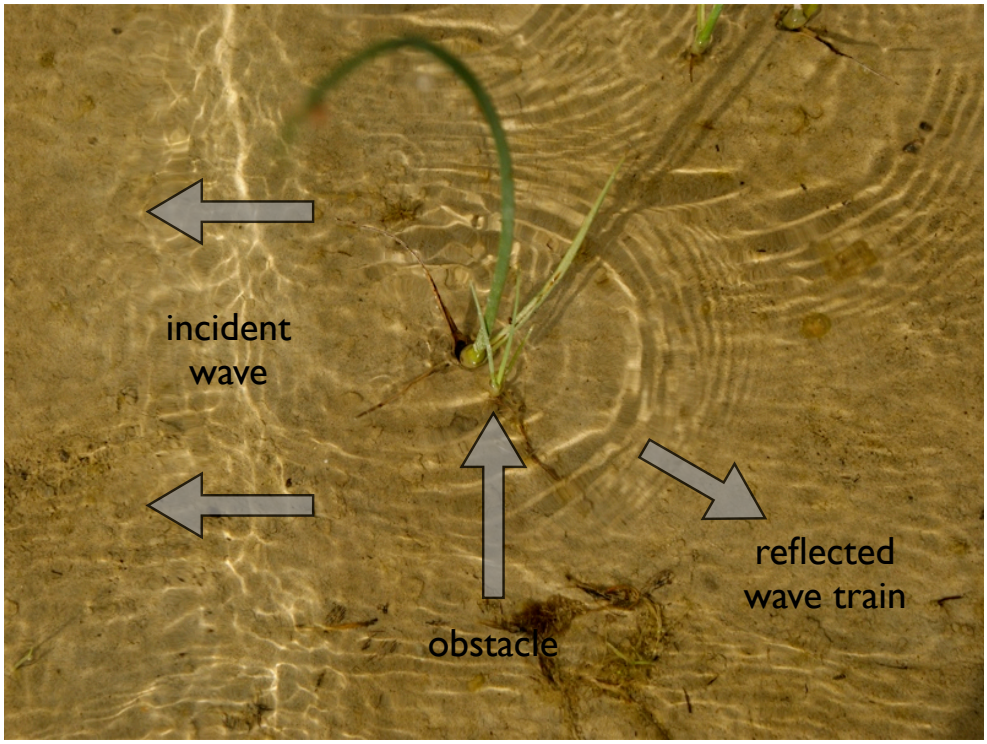

Figure 2.29: The interaction of a leftward propagating wave and an obstacle, in this case a plant.

To better illustrate the sort of interaction effect seen, wave fronts are shown in Figure 2.30 entering an area of lower sound speed (from the right) and the wave front is bent as the parts of the front that spend more time in the slower area drag behind the others.

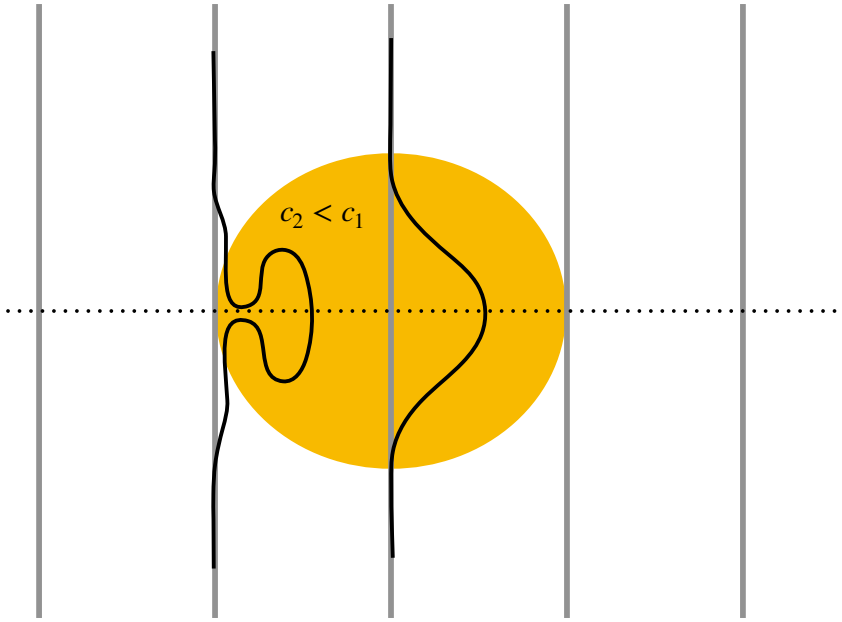

Figure 2.30: A diagram of wave fronts moving through an area of lower sound speed compared to the surrounding medium.

The following simulations were run on a grid with a 256 by 256 resolution.

2.4.1 Refraction without Damping

Now introducing variability in the medium, the wave speed is 20 times lower in the two elliptical areas than in the surrounding area. As such the refraction results in a focusing of the wave within the regions and makes, in essence, a point source. Figure 2.31 shows the evolution of the wave as time progresses and Figure 2.32 shows the same but as a close-up on the top ellipse to allow a better visualization of the behaviour.

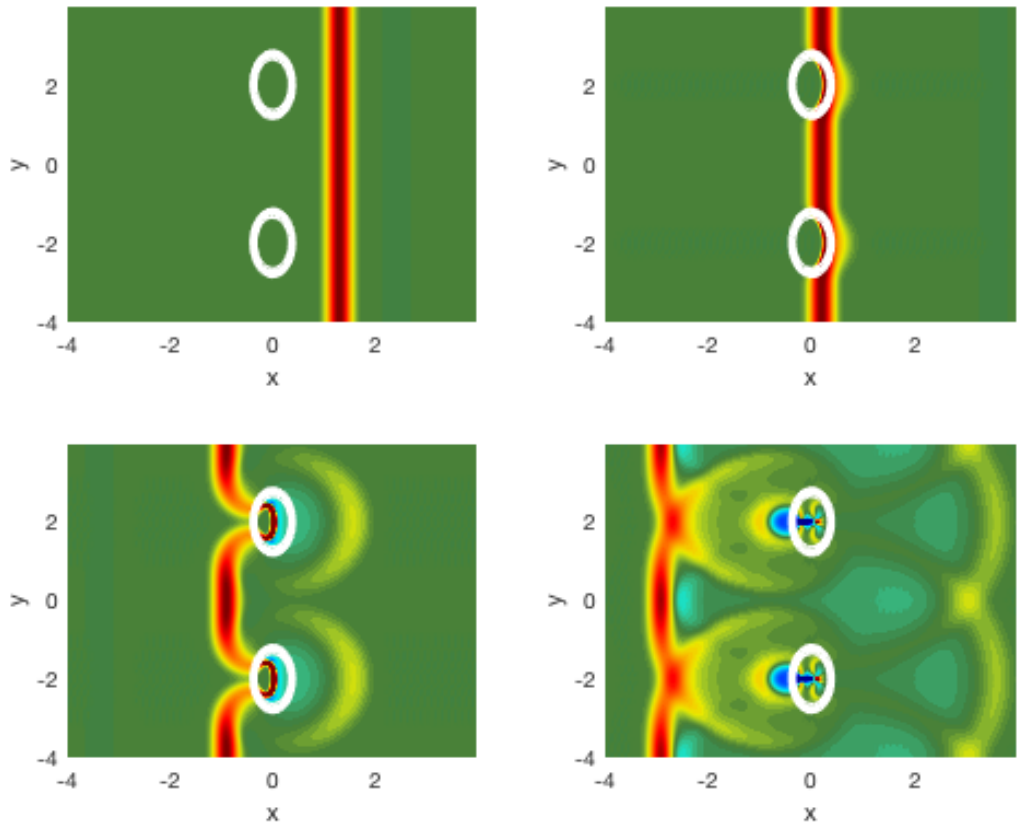

Figure 2.31: The wave evolution. Top left panel is at $t = 0.7$, top right panel is at $t = 1.8$, bottom left panel is at $t = 2.9$, and bottom right panel is at $t = 4.9$. The colour bar scale is -1 to 1.

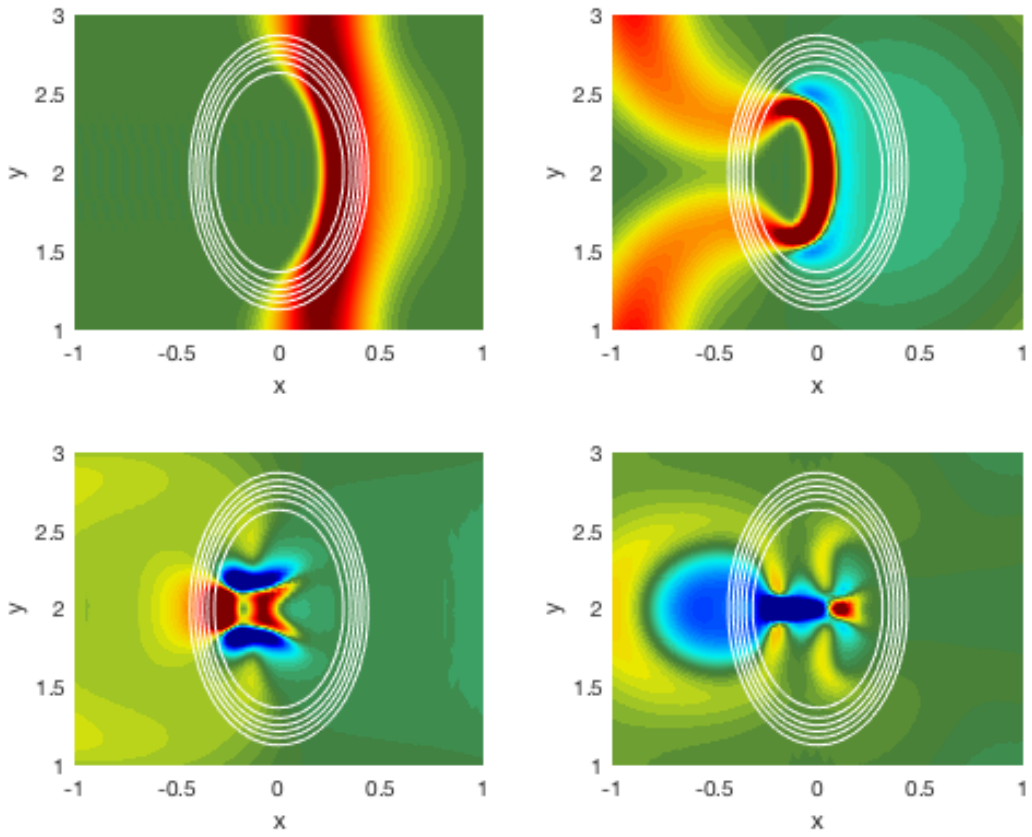

Figure 2.32: A close-up of the wave evolution inside the top ellipse. Top left panel is at $t = 1.8$, top right panel is at $t = 2.9$, bottom left panel is at $t = 4.2$, and bottom right panel is at $t = 4.9$. The colour bar scale is -1 to 1.

As the temperature change in HIFU depends on the squared acoustic pressure in an area, a series of simulations were run showing the accumulation of this pressure over time,

$$\int_0^t p(t')^2 \, dt',$$

scaled to account for stepping. Figure 2.33 is the accumulated pressure by $t = 30$ from the same simulation set-up as used for Figures 2.31 and 2.32.

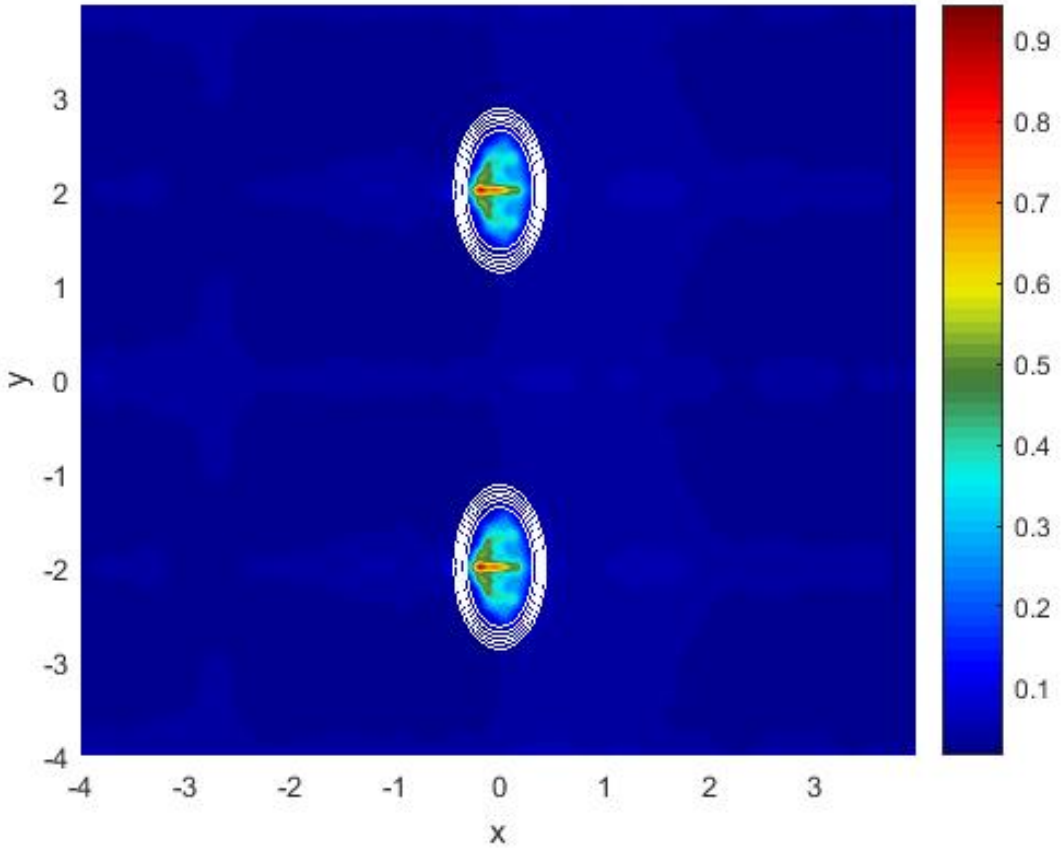

Figure 2.33: The pressure accumulated (via time integral) due to wave propagation. This is the initial set-up, with two elliptical areas where the wave speed is 20 times lower than in the surrounding area.

The model was run again with varying sizes and orientations. The ellipses were decreased to half of their original size (Figure 2.34), increased to twice their original size (Figure 2.35), and each rotated 90° from their original orientation (Figure 2.36). The focusing effect appeared to be identical and so it was determined that the size and orientation had little bearing on the focusing effect of the regions.

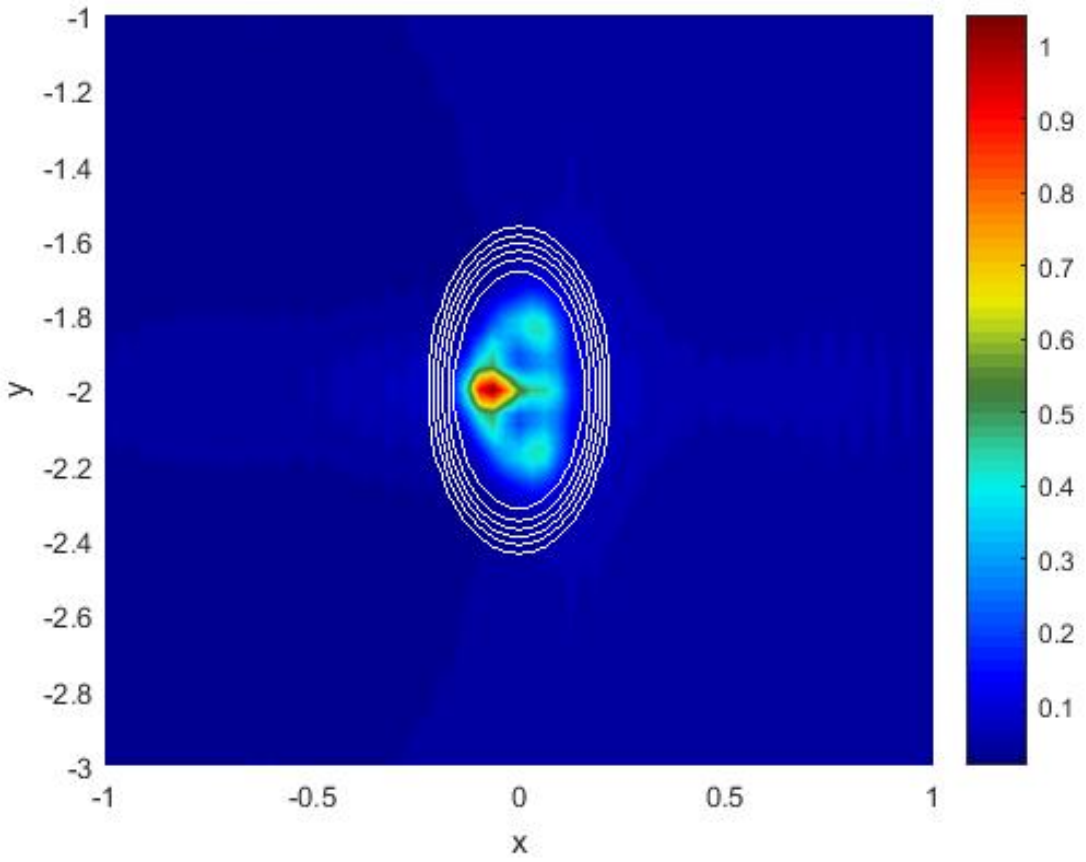

Figure 2.34: The pressure accumulated (via time integral) in smaller ellipses. The ellipses were decreased to half of their original size with the same wave speeds as the original. This figure is enlarged around the lower ellipse for better visibility.

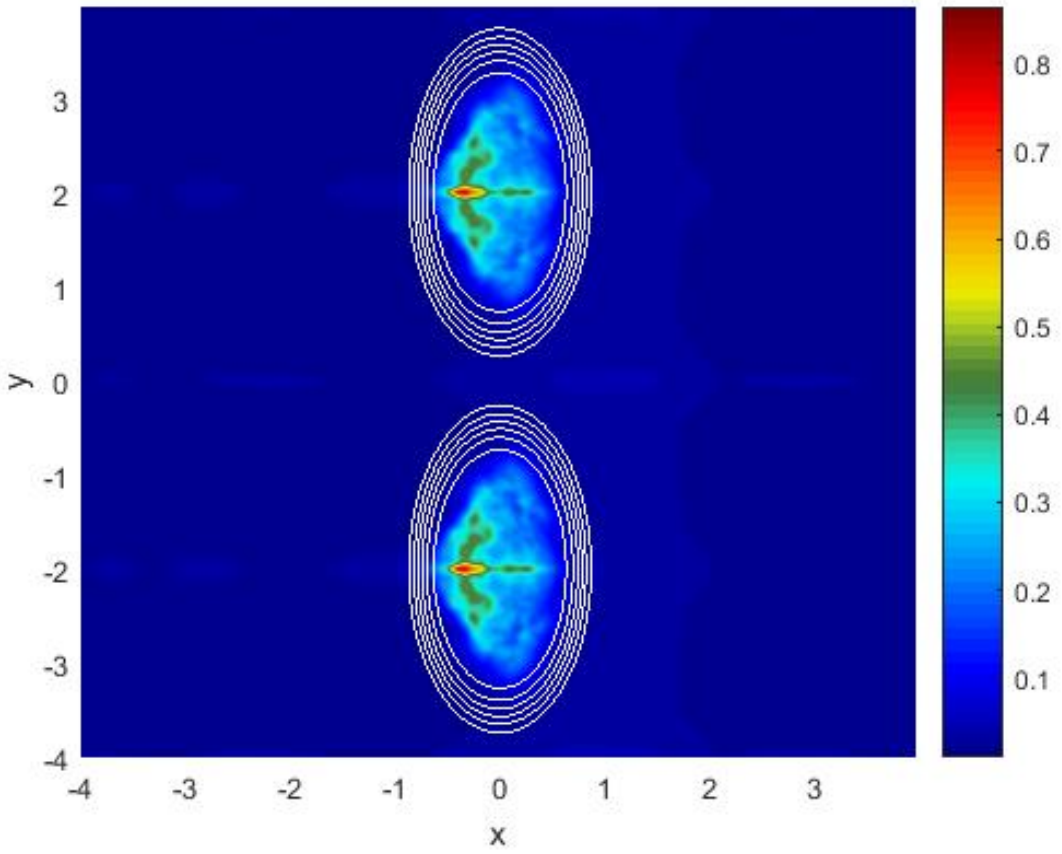

Figure 2.35: The pressure accumulated (via time integral) in larger ellipses. The ellipses were increased to twice their original size with the same wave speeds as the original.

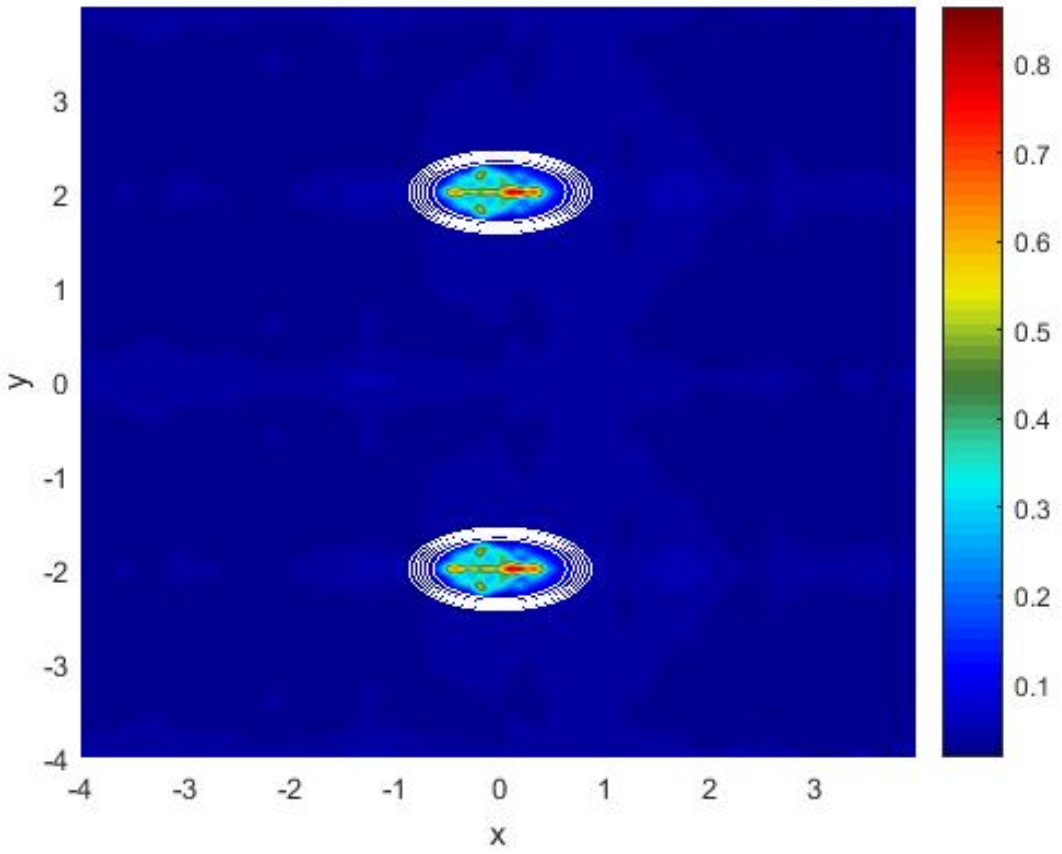

Figure 2.36: The pressure accumulated (via time integral) in rotated ellipses. The ellipses were turned 90°from their original orientations, maintaining the same wave speeds as the original.

Figure 2.37 shows a case where the wave speed instead is 6 times faster compared to when in the surrounding area. This is analogous to tissue surrounding bone, as opposed to less dense areas, such as lung, used for the other cases. There were no strong signs of the wave focusing. When scaled similarly to the previous models, no effects could be seen.

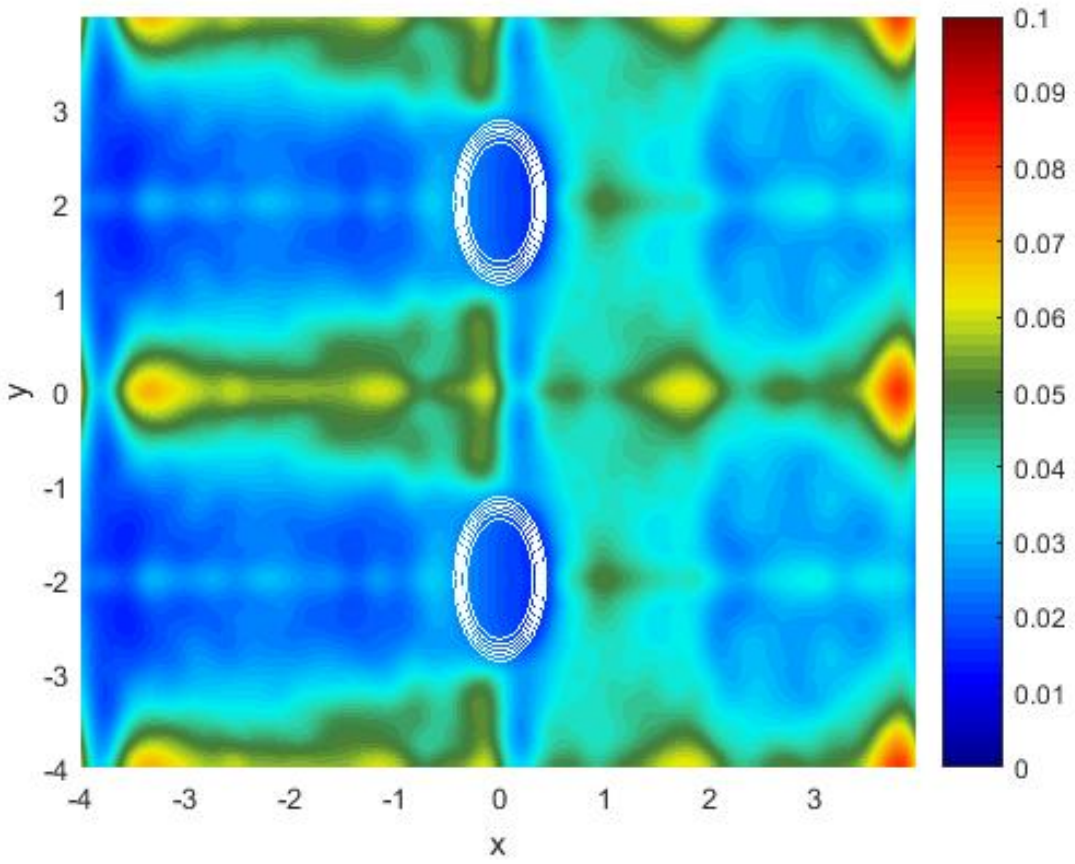

Figure 2.37: The pressure accumulated (via time integral) in the same ellipses as the original model with the wave speed now 6 times higher than in the surrounding area.

2.4.2 Refraction with Damping

Including damping in the earlier refraction, Figures 2.38 and 2.39 are versions of Figures 2.31 and 2.32 now with damping included. It can be seen in Figure 2.38 that the wave is already losing strength by the time it reaches the elliptical zones and that there is much less of a wave continuing past the ellipses than in the undamped case. The focusing still occurs but Figure 2.39 shows a significant drop in the amplitude of the waves inside the ellipses.

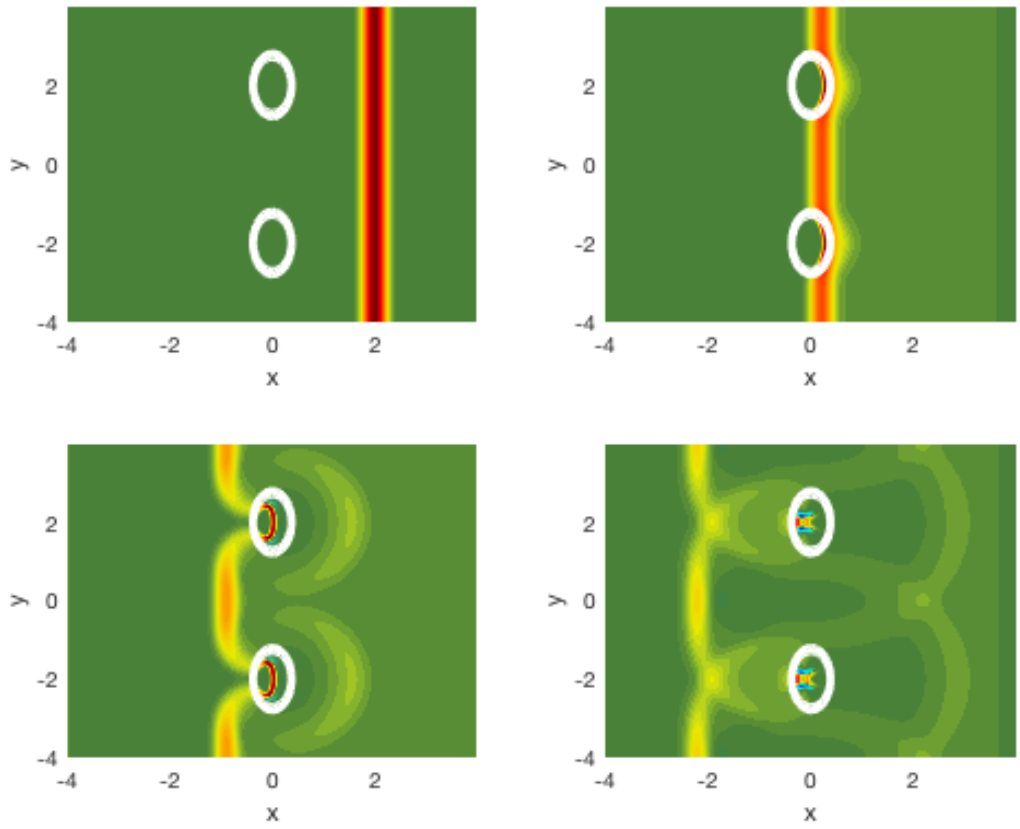

Figure 2.38: The wave evolution with damping. Top left panel is at $t = 0$, top right panel is at $t = 1.8$, bottom left panel is at $t = 2.9$, and bottom right panel is at $t = 4.9$. The colour bar scale is -1 to 1.

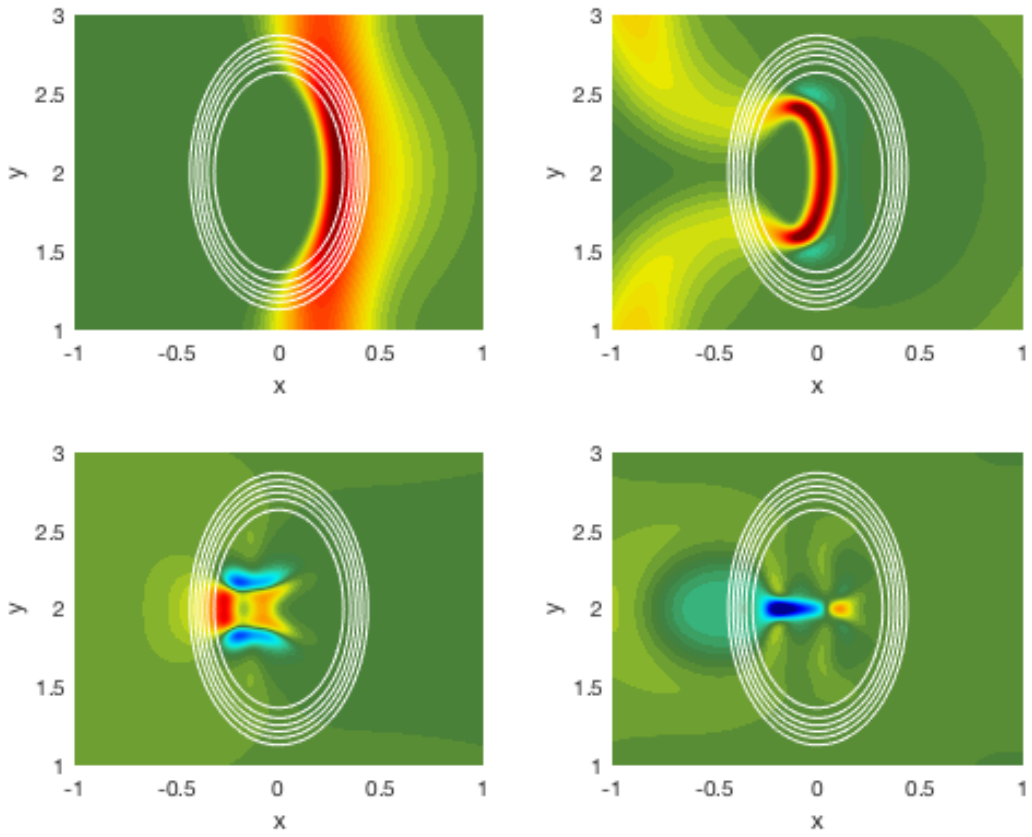

Figure 2.39: A close-up of the wave evolution with damping inside the top ellipse. Top left panel is at $t = 1.8$, top right panel is at $t = 2.9$, bottom left panel is at $t = 4.2$, and bottom right panel is at $t = 4.9$. The colour bar scale is -1 to 1.

Performing the accumulated pressure analysis, but now with damping, we get Figures 2.40, 2.41, 2.42, 2.43, and 2.44 (corresponding to Figures 2.33, 2.34, 2.35, 2.36, and 2.37 respectively). As expected, with damping the accumulated pressure is much less, an order of magnitude less, than it is without damping (note the change in scales).

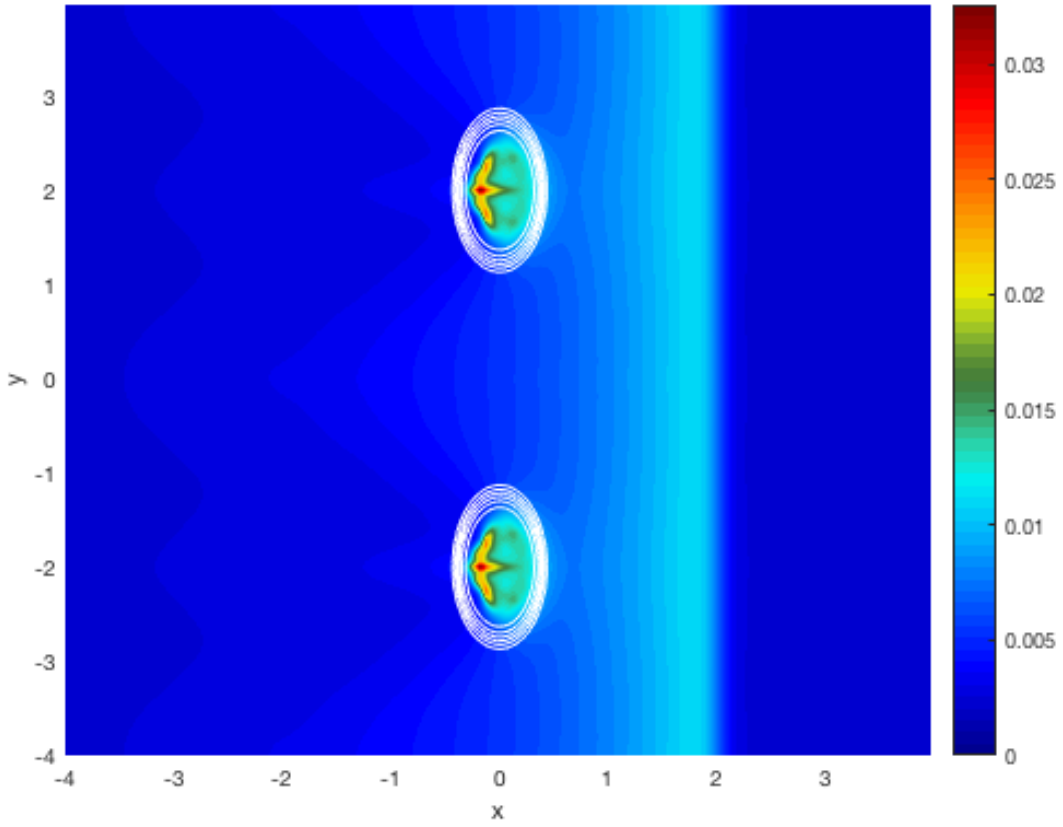

Figure 2.40: The pressure accumulated (via time integral) due to damped wave propagation. The wave speed is 20 times lower in the two elliptical areas than in the surrounding area.

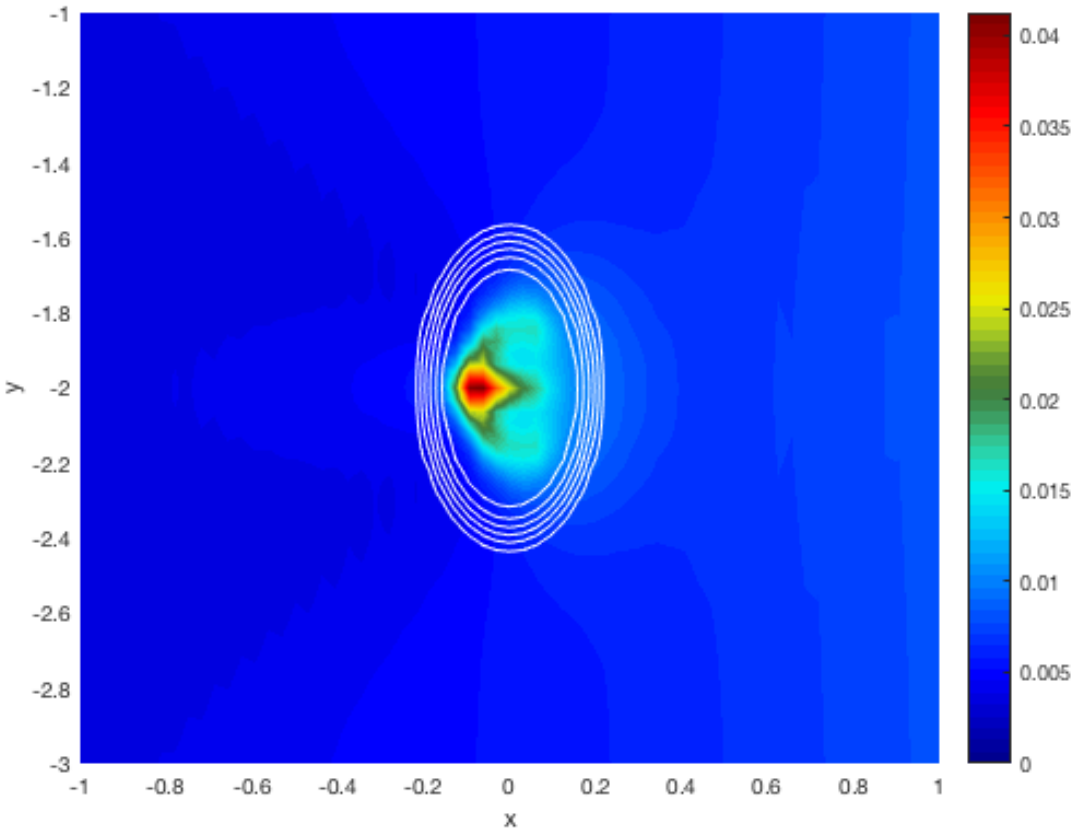

Figure 2.41: The pressure accumulated (via time integral) due to damped wave propagation in smaller ellipses. The ellipses were decreased to half of their original size with the same wave speeds as the original. This figure is enlarged around the lower ellipse for better visibility.

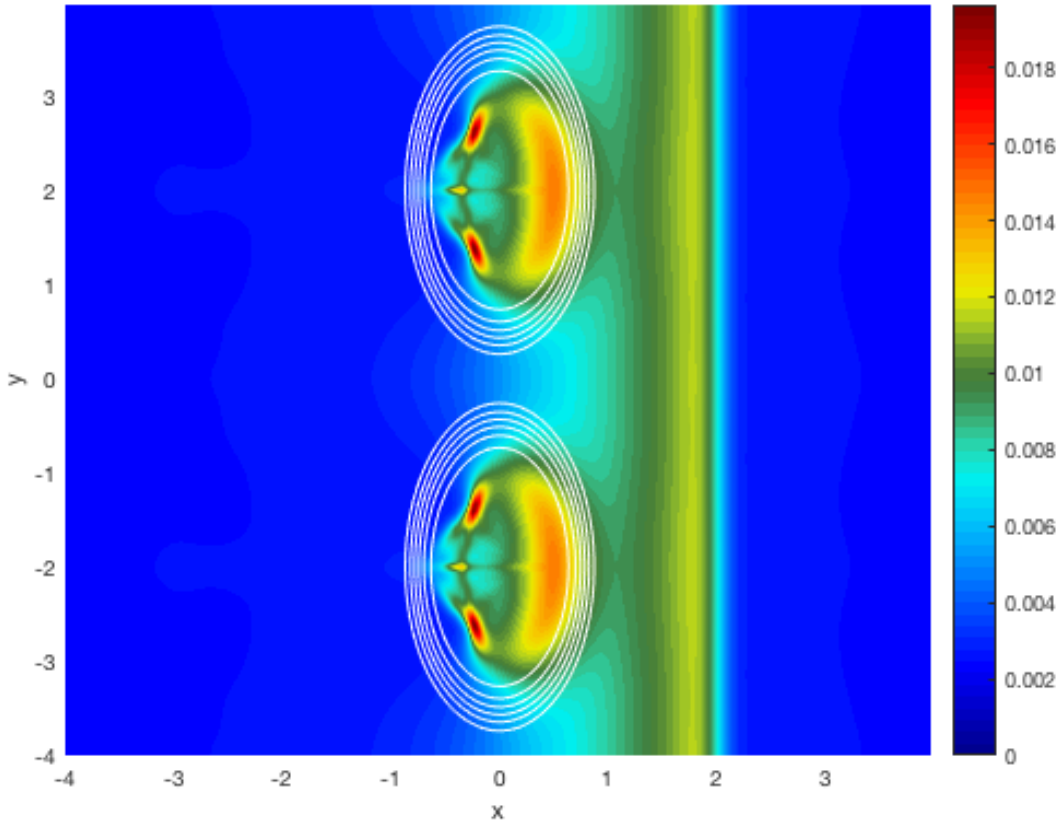

Figure 2.42: The pressure accumulated (via time integral) due to damped wave propagation in larger ellipses. The ellipses were increased to twice their original size with the same wave speeds as the original.

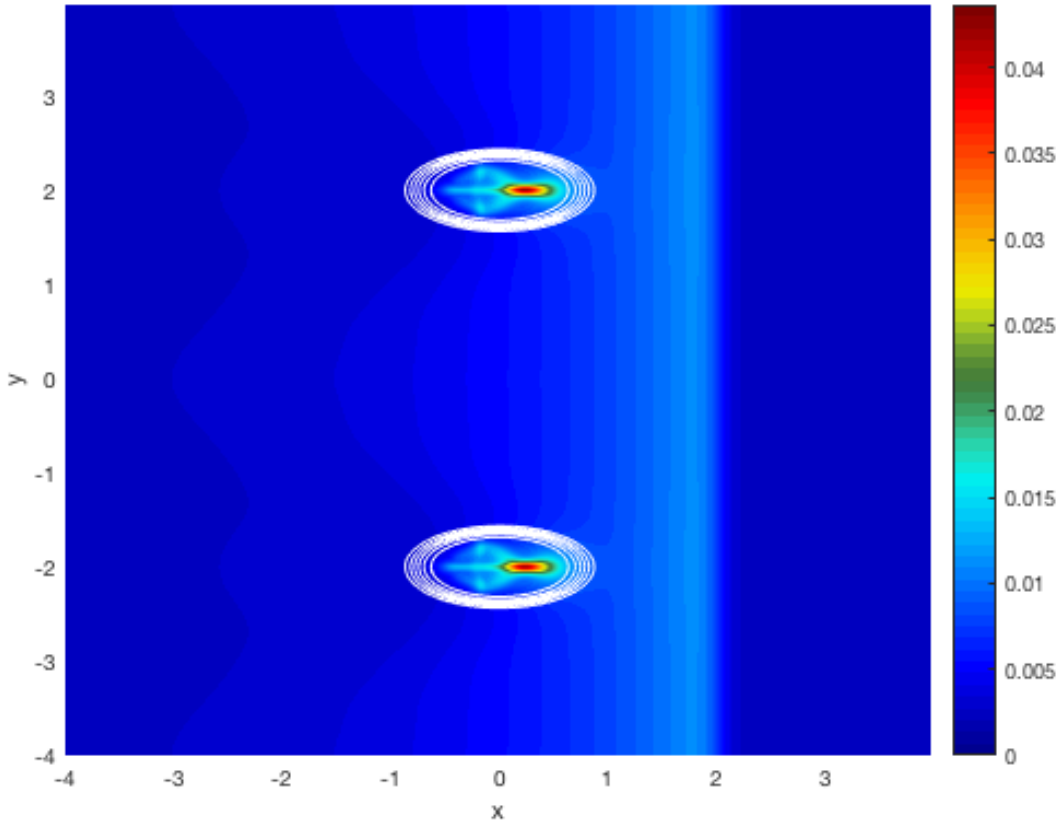

Figure 2.43: The pressure accumulated (via time integral) due to damped wave propagation in rotated ellipses. The ellipses were turned 90°from their original orientations, maintaining the same wave speeds as the original.

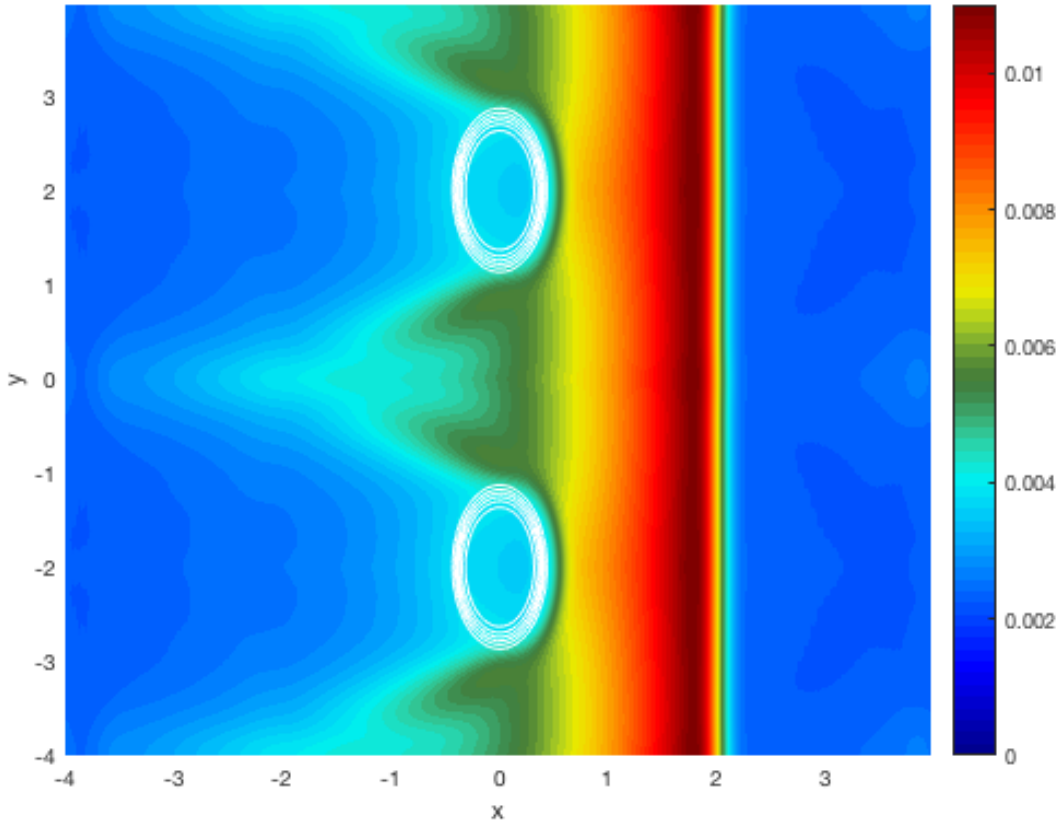

Figure 2.44: The pressure accumulated (via time integral) due to damped wave propagation in the same ellipses as the original model with the wave speed now 6 times higher than in the surrounding area.

2.5 Conclusions

A two-dimensional version of the acoustic model is used for numerical simulations which illustrate a focusing effect from the refraction of the acoustic waves in and around anomalous regions. This is of great interest clinically as the peaks seen due to the reflections and refractions inside the anomaly indicate a risk of generating high temperatures in unintended regions. In fact it is noted that the focusing is more prominent when the waves encounter embedded areas of lower sound speeds, such as lungs, as opposed to areas of

higher sound speed, such as bones. The behaviour of HIFU in and around bone is an area of interest clinically as MRI cannot detect temperature data in bone as it can in other tissue, though this situation is complicated by Rayleigh waves at the bone tissue interface and the possibility of shear waves inside the bone.

Chapter 3

A Sensitivity Analysis of Parameters: Parametric Stochastics

3.1 Methods

The average velocity of sound in human tissue is 1540 m/s [10] although Ludwig did find the values varied from 1490 m/s to 1610 m/s, largely depending on specific tissue types [10]. The velocity of sound in human bone is 2070-5350 m/s [13]. For the simulation, the average speed of sound in bone was set to 5350 m/s (chosen so the simulation represents an anomaly most similar to the denser cortical bone) and the average speed of sound in tissue was set to 1540 m/s. The model utilizes a dimensionless pressure therefore it is the ratios, or percent changes, that are significant.

A technician (Adam Waspe, Sick Kids Hospital, *personal communication*) using HIFU to treat patients found that in rare cases the treatment dramatically deviated from what the model predicted and so treatment could not be continued. In an attempt to resolve the problem he tried adjusting some of the parameters in the in-house model by ten percent of the commonly accepted values *(Adam Waspe, personal communication)*. The goal of this chapter is to look at such adjustments from a parametric stochastic viewpoint.

The parameters manipulated are: c_1, the speed of sound in the tissue; c_2, the speed of sound in bone and; r, the radius of the bone. These parameters are either held constant or taken from a Gaussian distribution $\mathcal{N}(\mu, \sigma^2)$ using cited averages for μ values and standard

deviations of ten percent of the average value (as mentioned above). The specific cases are laid out in Table 3.1.

Case	c_1 (m/s)	c_2 (m/s)	r
1	$\mathcal{N}(1540, 154^2)$	5350	0.4
2	1540	$\mathcal{N}(5350, 535^2)$	0.4
3	1540	5350	$\mathcal{N}(0.4, 0.04^2)$
4	$\mathcal{N}(1540, 154^2)$	$\mathcal{N}(5350, 535^2)$	0.4
5*	$\mathcal{N}(1540, 154^2)$	$\mathcal{N}(5350, 535^2)$	0.4
6	$\mathcal{N}(1540, 154^2)$	$\mathcal{N}(5350, 535^2)$	$\mathcal{N}(0.4, 0.04^2)$

Table 3.1: Table of cases and values. In general, values for c_1 and c_2 are chosen from the distribution once per "person" (simulation) and used everywhere in the corresponding region. However, Case 5 was run selecting different values from the distribution at each point in the corresponding regions rather than a single value for the entirety of each corresponding region (as was done in all other cases).

All cases use an ensemble of 100 simulations. Each simulation is set to have an ultrasound wave incoming from the right of the anomaly and includes damping of the wave. Please note that radius is in dimensionless units. And because time and space are dimensionless and no values were available in the clinical literature, b was chosen so as to provide a representative value. However, b was not large enough to damp the wave prior to reaching the anomaly.

The anomaly used for subsections 3.2.1, 3.2.2, and 3.2.4 is shown in Figure 3.1. In subsections 3.2.3 and 3.2.6 the anomaly has a varying radius but is otherwise set up the same way. An example of the anomaly used for subsection 3.2.5 is shown in Figure 3.2.

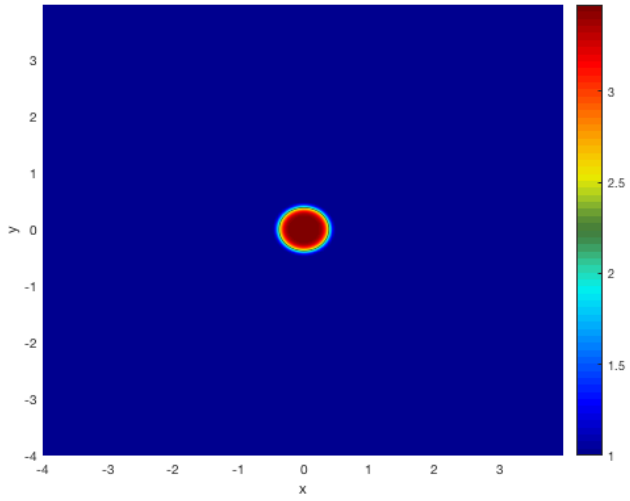

Figure 3.1: The anomalous zone in the simulations when using the average values for the speed of sound in each material. The interior region has a faster sound speed than the outer region, simulating bone surrounded by tissue. ($c_1 = 1540$, $c_2 = 5350$)

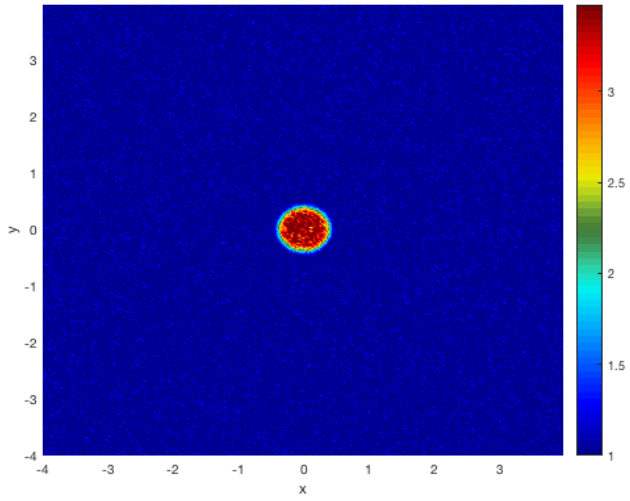

Figure 3.2: Example anomalous zone in the Case 5 simulations. Values for the speed of sound in each region were taken from Gaussian distributions as described in Table 3.1. Parameters c_1 and c_2 taken from $\mathcal{N}(1540, 154^2)$ and $\mathcal{N}(5350, 535^2)$ distributions respectively.

3.2 Results

3.2.1 Normal distribution for c_1

Figure 3.3 shows the results of the simulation when selecting c_1 from a normal distribution with mean 1540 m/s and standard deviation of 154 m/s (ten percent of the commonly used standard, as discussed).

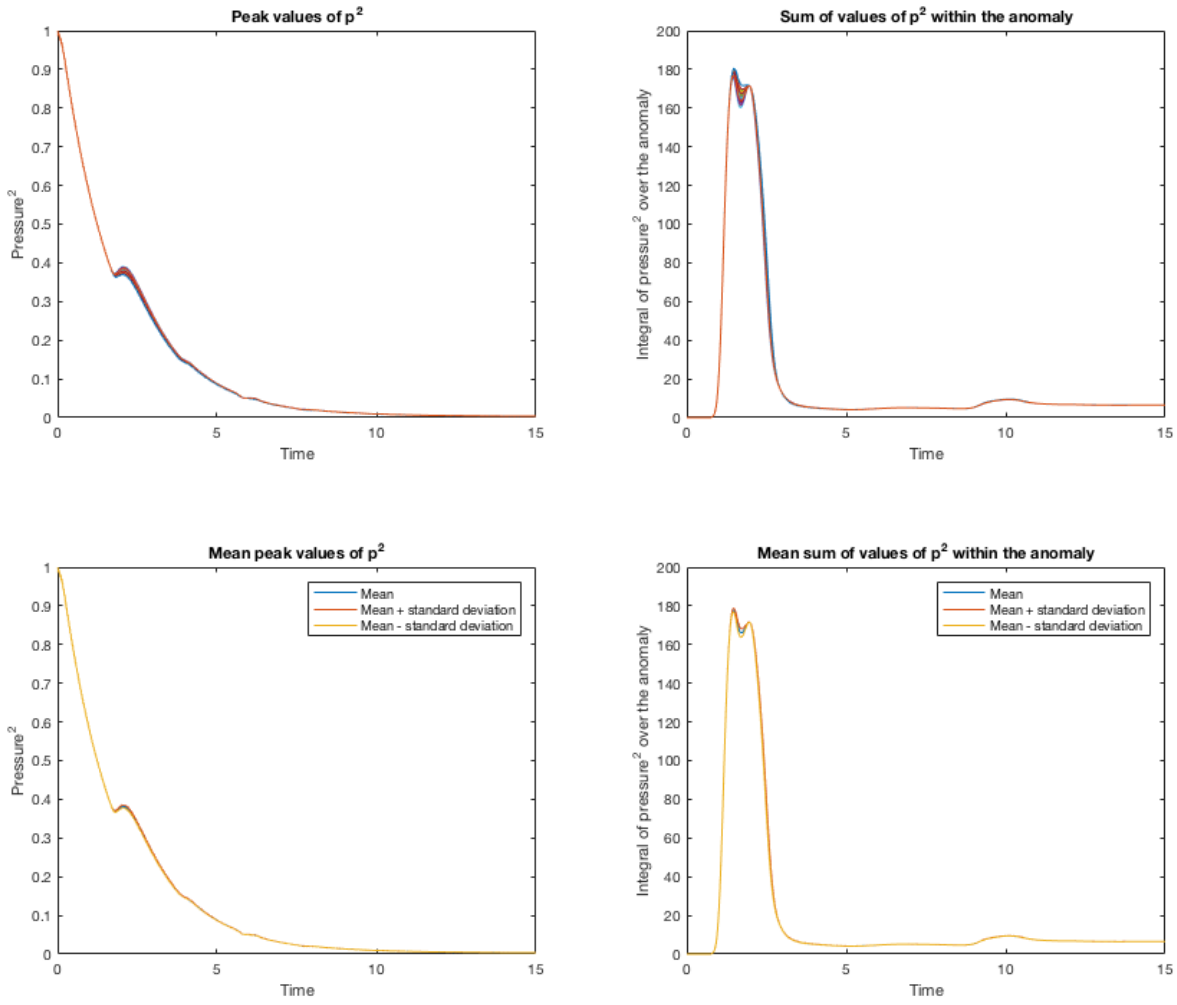

Figure 3.3: Case 1 (from Table 3.1): Time series depicting an ensemble of 100 varying the speed of sound in the material around the anomalous area (c_1). Parameters: $c_2 = 5350$m/s and $r = 0.4$. Top left: The peak value of pressure squared as a function of time for each member of the ensemble. Top right: The sum of pressure squared as a function of time within the anomaly area for each member of the ensemble. Bottom left: The mean for the ensemble of the peak value of pressure squared as a function of time. Bottom right: The mean for the ensemble of the sum of pressure squared as a function of time within the anomaly area

The top left plot in Figure 3.3 depicts how the maximum value of the squared pressure

changes over time for the set of simulations. The damping incorporated in the simulation is responsible for the initial decrease in the graph. The secondary peak is due to the interaction with the anomalous area, in particular the reflections and refractions discussed in Section 2.4. Notice that, although it is the speed in the tissue (the outer region) that is being varied, the results do not show significant differences until the waves have hit the anomalous region and the resulting reflections and refractions were introduced. The bottom left plot in Figure 3.3 shows the mean of the ensemble in the top left plot along with lines indicating the standard deviation. However, the variation in the ensemble was so small that the lines overlap to the point of being nearly unseen.

The top right plot in Figure 3.3 depicts how the total of the squared pressure within the anomalous area changes over time for the ensemble. The peak corresponds with when the ultrasound wave reached the anomalous zone. The bottom right plot in Figure 3.3 shows the mean of the ensemble in the top right plot along with lines indicating the standard deviation. Similar to the bottom left plot in Figure 3.3, the lines showing the variation are frequently hidden from view due to overlapping. For better visibility, Figure 3.4 shows a close-up of the double peak in the bottom right plot on Figure 3.3.

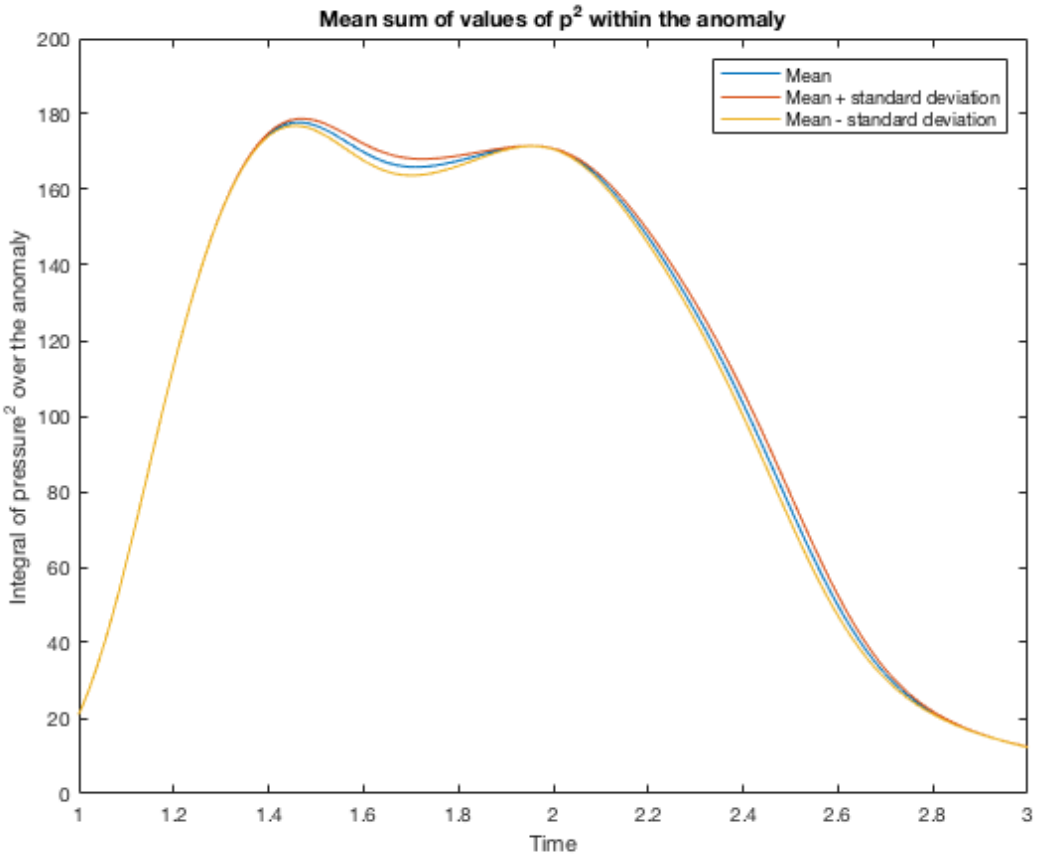

Figure 3.4: Case 1: A close-up of the double peak in the mean for the ensemble of the sum of pressure squared as a function of time within the anomaly area. Parameters: $c_2 = 5350$m/s and $r = 0.4$. Varying c_1.

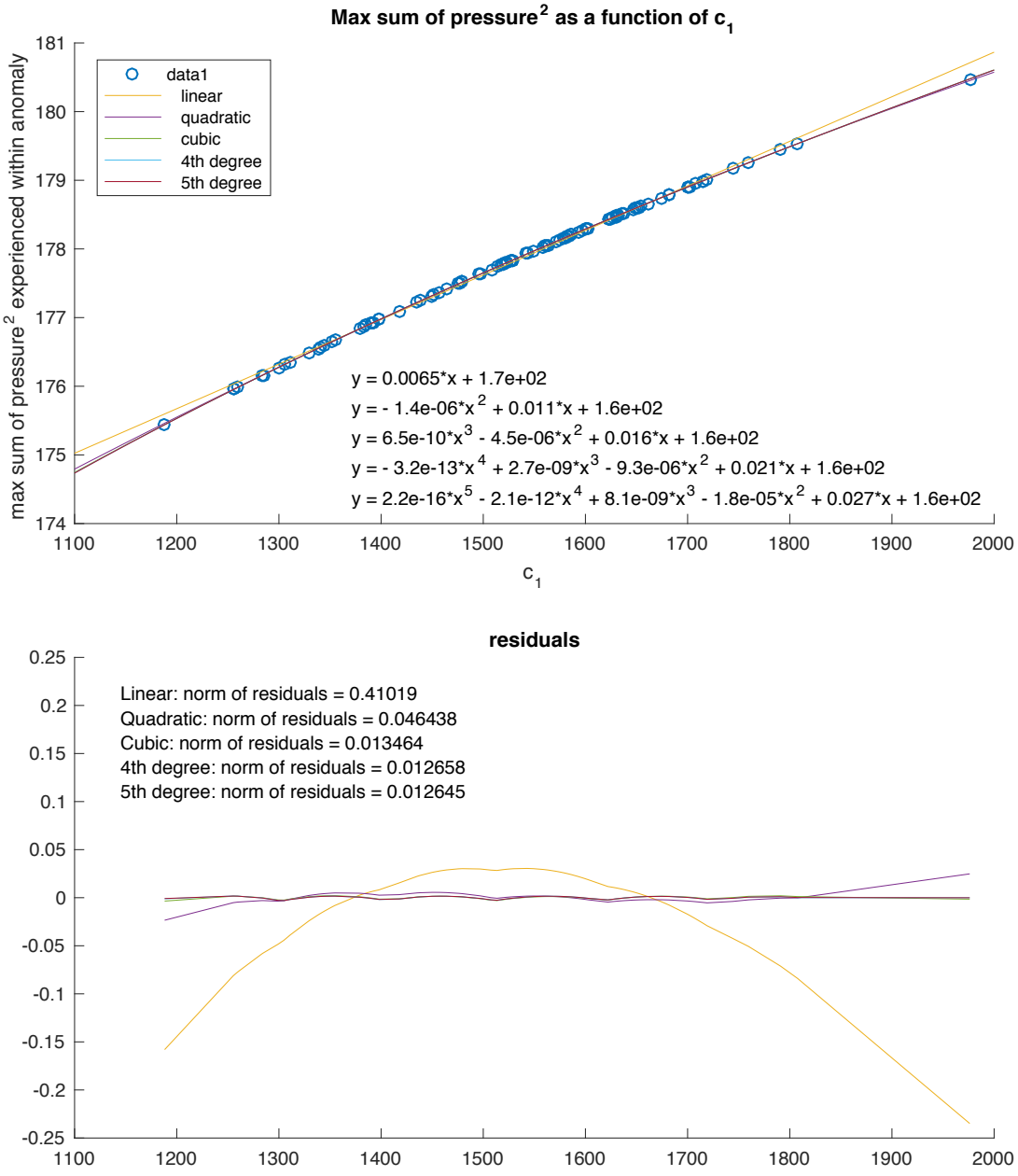

Figure 3.5: Case 1: Top: Correlation of c_1 with the maximum value of the sum of pressure squared inside the anomaly achieved in a run when varying only c_1 with five orders of polynomial fits. Bottom: The residuals for the polynomial fits shown in the top graph. Parameters: $c_2 = 5350$m/s and $r = 0.4$. Varying c_1.

Figure 3.5 shows the roughly linear relation between c_1 (the speed outside of the anomaly) and the maximum of the sum of pressure squared inside the anomalous region for each simulation, as well as a number of higher order polynomial fits. The linear approximation ($y = 0.0065x + 170$) shows that the maximum pressure squared inside of the anomaly increases with c_1. Note that going up to only a quadratic approximation decreases the residual by an order of magnitude. Also, increasing the order of the approximation further than cubic has limited effect on the residual. The greatest maximum of the sum of pressure squared inside of the anomaly was 180.4756 and the least was 175.4383 so there is less than a three percent difference over the ensemble.

3.2.2 Normal distribution for c_2

Figure 3.6 shows the results of the simulation when selecting c_2 from a normal distribution with mean 5350 m/s and standard deviation of 535 m/s (ten percent of the commonly used standard, as discussed) while keeping c_1 and radius constant at 1540 m/s and 0.4 dimensionless units, respectively. Again, for better visibility, Figure 3.7 shows a close-up of the double peak in the bottom right plot on Figure 3.6.

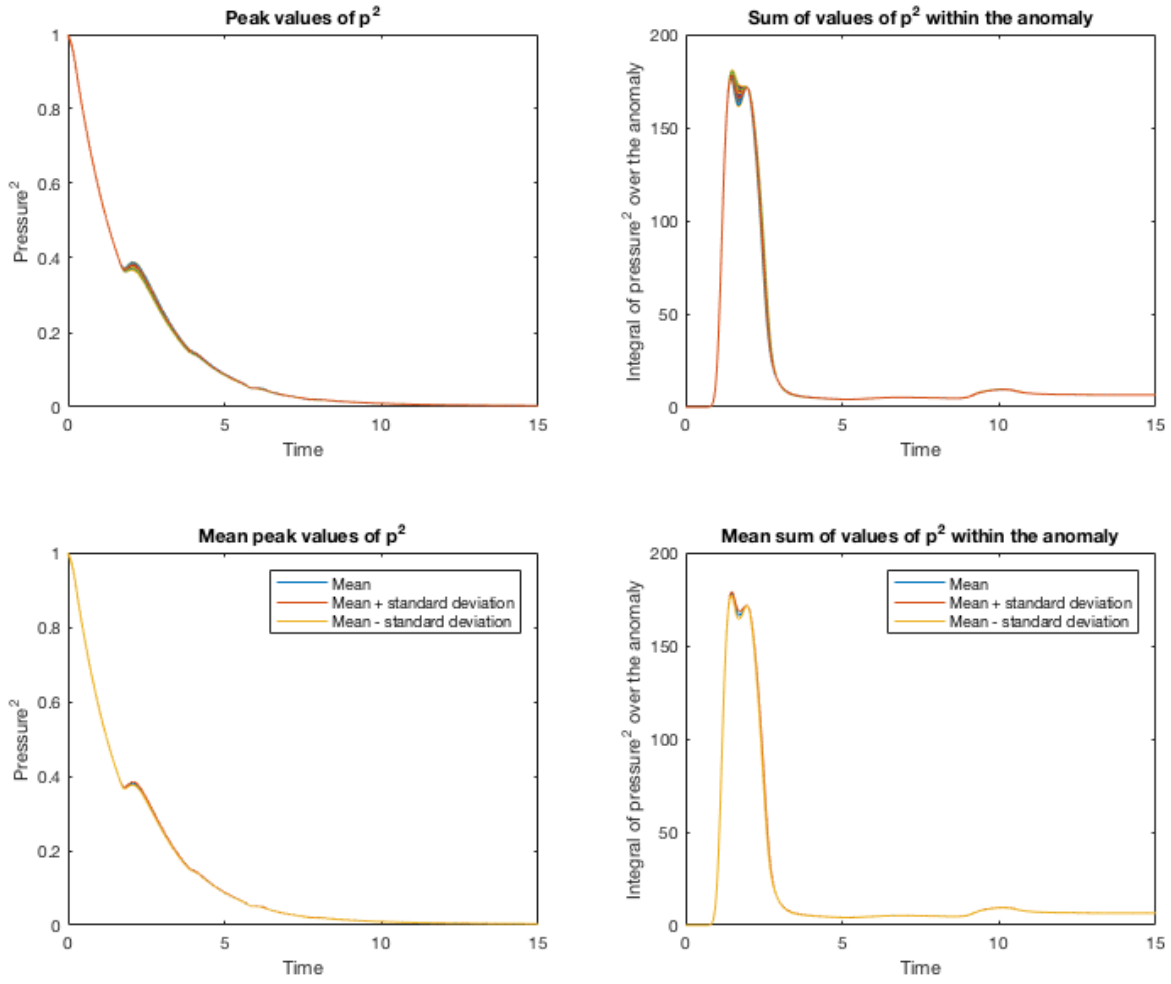

Figure 3.6: Case 2 (from Table 3.1): Time series depicting an ensemble of 100 varying the speed of sound in the material inside the anomalous area (c_2). Parameters: $c_1 = 1540$m/s and $r = 0.4$. Top left: The peak value of pressure squared as a function of time for each member of the ensemble. Top right: The sum of pressure squared as a function of time within the anomaly area for each member of the ensemble. Bottom left: The mean for the ensemble of the peak value of pressure squared as a function of time. Bottom right: The mean for the ensemble of the sum of pressure squared as a function of time within the anomaly area.

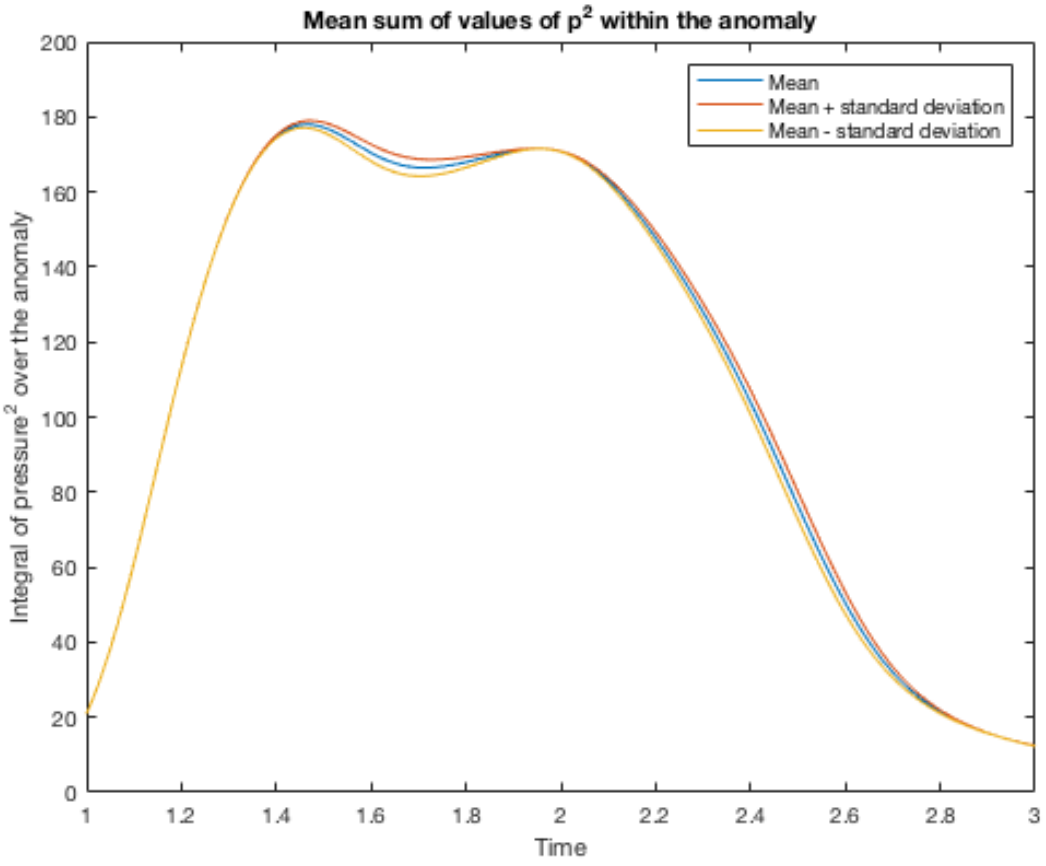

Figure 3.7: Case 2: A close-up of the double peak in the mean for the ensemble of the sum of pressure squared as a function of time within the anomaly area. Parameters: $c_1 = 1540$m/s and $r = 0.4$. Varying c_2.

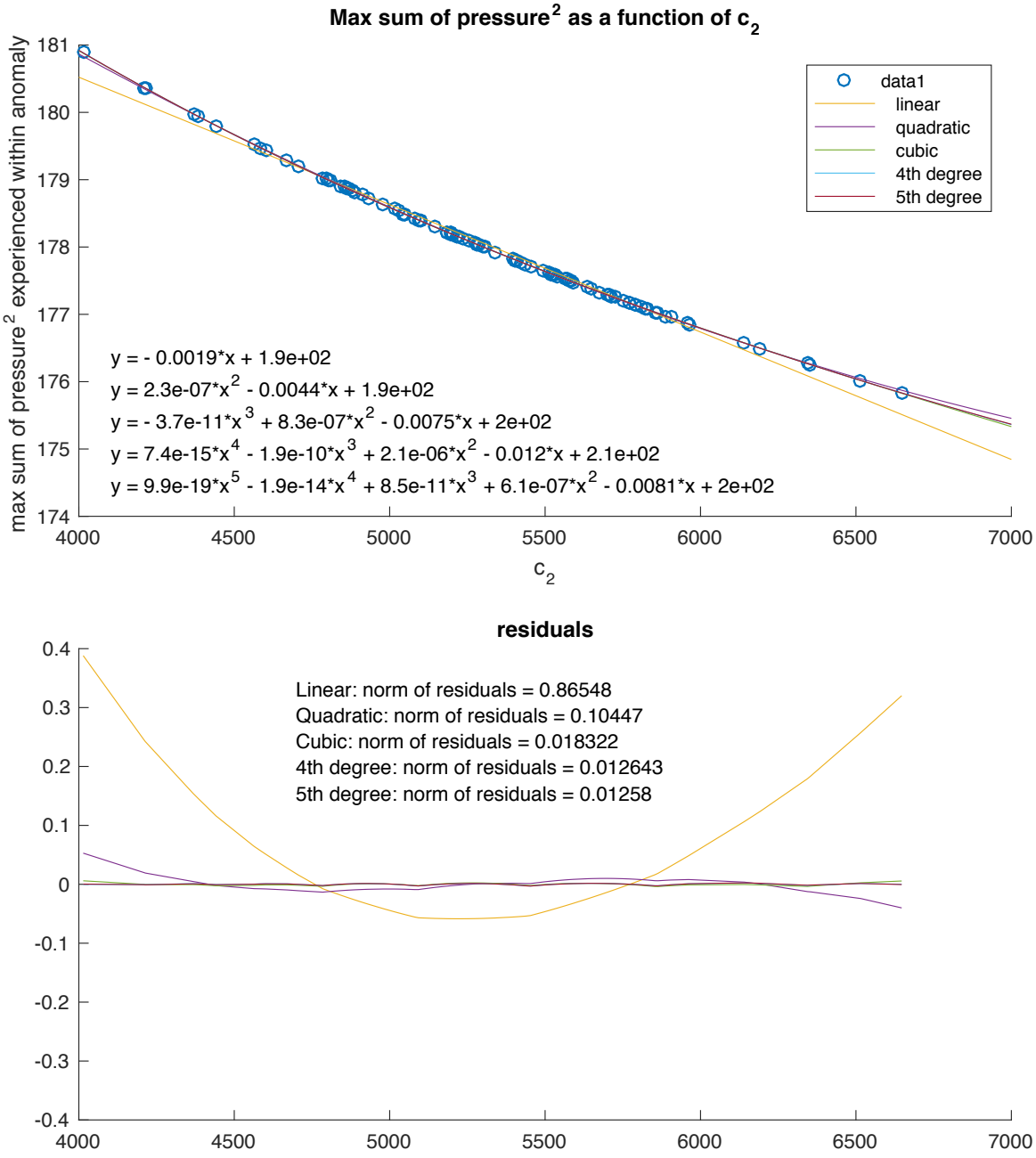

Figure 3.8: Case 2: Top: The normalized maximum value of the sum of the pressure squared inside the anomaly as a function of c_2 with five orders of polynomial fits. Bottom: The residuals for the polynomial fits shown in the top graph. Parameters: $c_1 = 1540$m/s and $r = 0.4$. Varying c_2.

This section, specifically Figure 3.8, shows a roughly linear (or exceptionally straight higher order polynomial) relation between c_2 (the speed inside of the anomaly) and the sum of the maximum pressure squared inside the anomalous region for each simulation, as well as a number of higher order polynomial fits. The quadratic approximation again has a residual an order of magnitude smaller than the linear approximation and there is close agreement at higher order approximations. Note however that, unlike with the speed of sound outside of the anomaly, increasing the speed of sound inside of the anomaly decreases the maximum sum of pressure squared experienced within the anomalous region. The greatest maximum of the sum of pressure squared inside of the anomaly was 180.8837 and the least was 175.8325 so there is again less than a three percent difference over the ensemble.

3.2.3 Normal distribution for radius

Figure 3.9 shows the results of the simulation when selecting the radius from a normal distribution with a mean of 0.4 dimensionless units and a standard deviation of 0.04 dimensionless units while keeping c_1 and c_2 constant at 1540 m/s and 5350 m/s respectively. Note that the right-hand plots in Figure 3.9 show values normalized by the mean area.

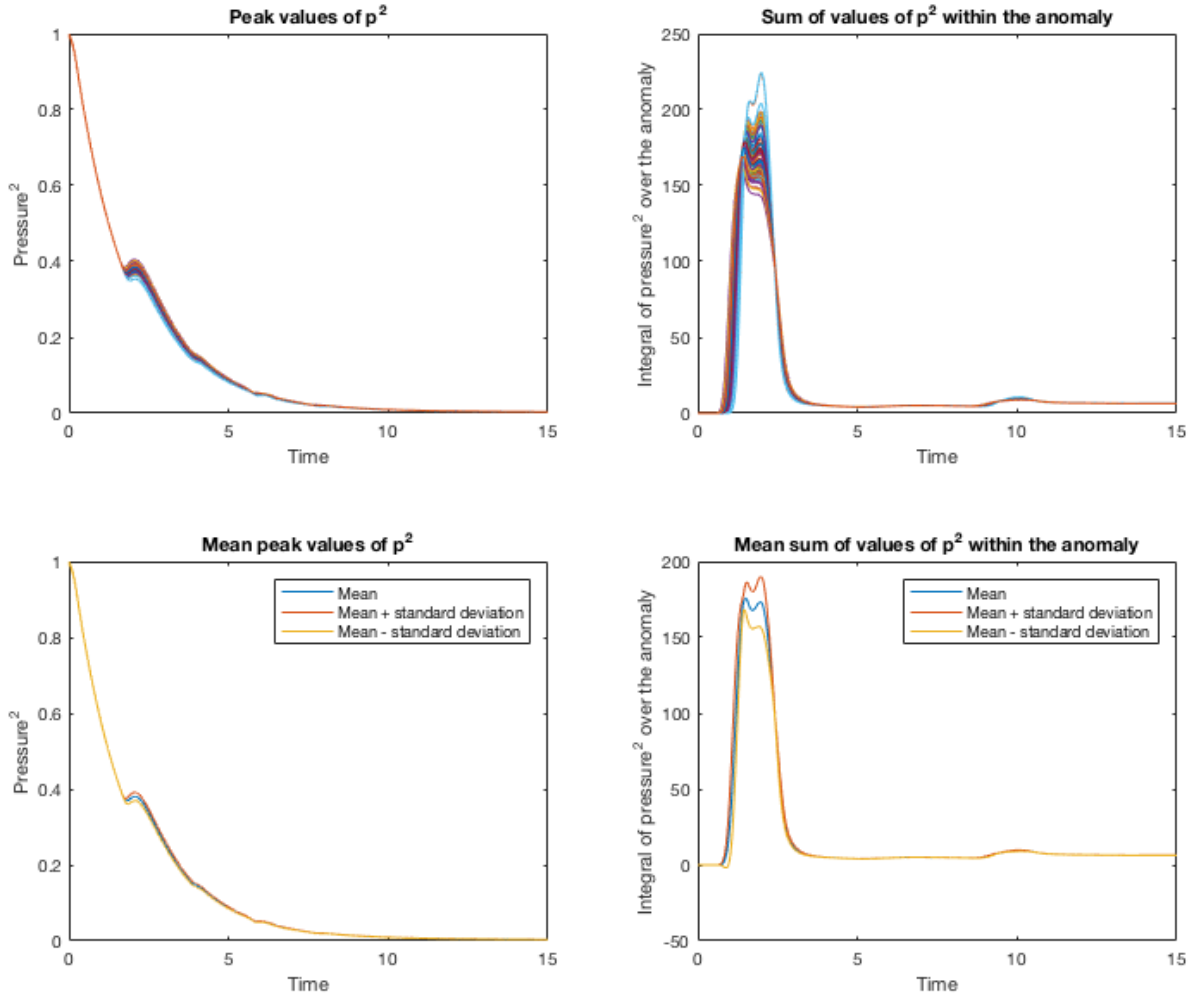

Figure 3.9: Case 3 (from Table 3.1): Time series depicting an ensemble of 100 varying only radius (r). Parameters: $c_1 = 1540$m/s and $c_2 = 5350$m/s. Top left: The peak value of pressure squared as a function of time for each member of the ensemble. Top right: The normalized sum of pressure squared as a function of time within the anomaly area for each member of the ensemble. Bottom left: The mean for the ensemble of the peak value of pressure squared as a function of time. Bottom right: The normalized mean for the ensemble of the sum of pressure squared as a function of time within the anomaly area.

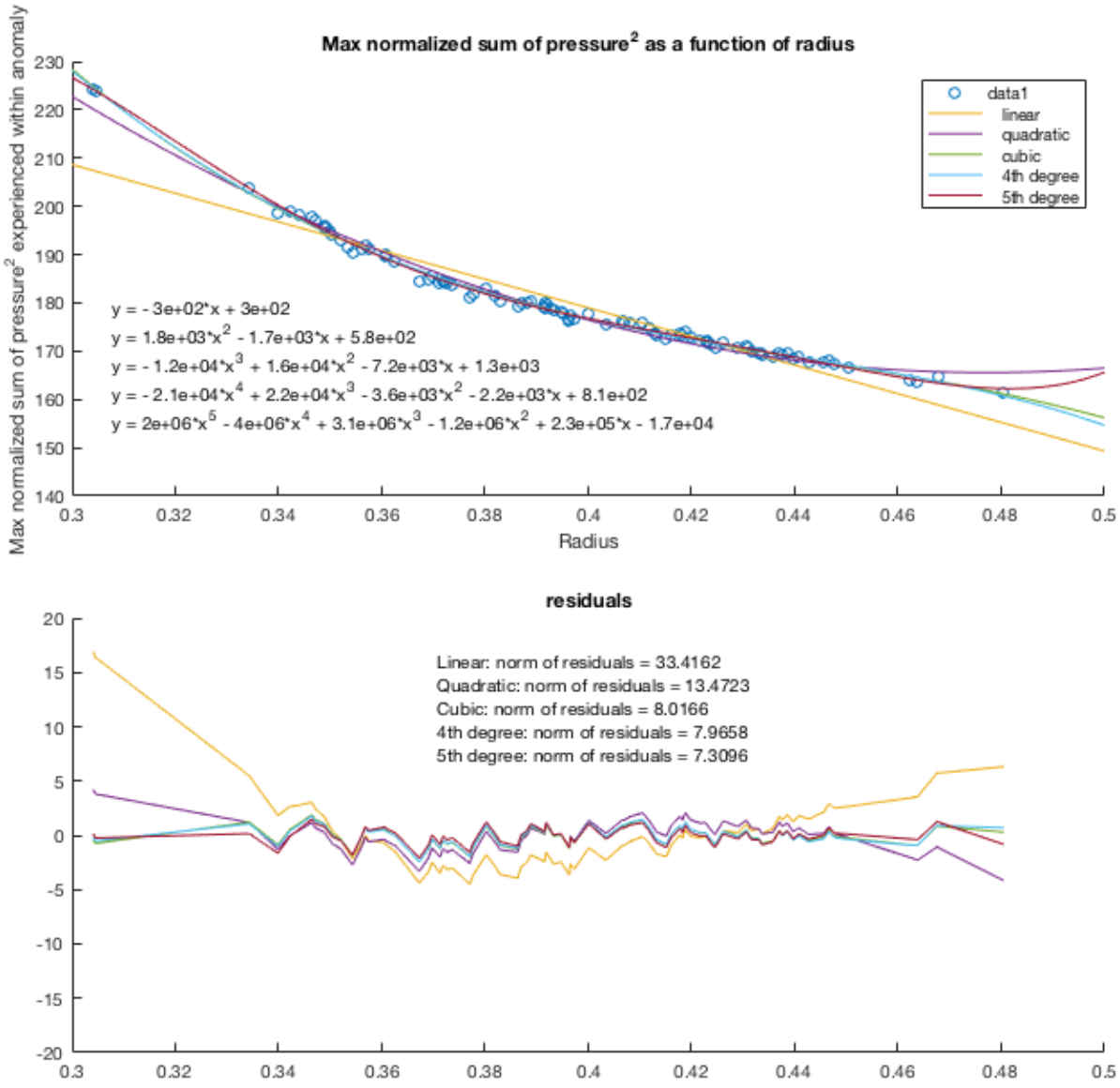

Figure 3.10: Case 3: Top: The normalized maximum value of the sum of the pressure squared inside the anomaly as a function of radius with five orders of polynomial fits. Bottom: The residuals for the polynomial fits shown in the top graph. Parameters: $c_1 = 1540$m/s and $c_2 = 5350$m/s. Varying r.

This section, specifically Figure 3.10, shows that a smaller radius contributes to higher

pressure squared sums as the linear approximation is $y = -300x + 300$. Increasing the order of approximation is not as dramatic as in the previous two cases but it does reduce the residual for the quadratic to one third of the residual for the linear approximation. The greatest maximum of the normalized sum of pressure squared inside of the anomaly was 224.3559 and the least was 161.4110 with a mean of 179.7344 so the max can rise over twenty-four percent above the mean and drop over ten percent below the mean. Remembering the effects of reflection and refraction as discussed in Section 2.4 it becomes clear why this is the case. The focusing caused by the anomaly is largely dependent on the radius and is clearly significant.

3.2.4 Normal distributions for c_1 and c_2

Figure 3.11 shows the results of the simulation when selecting c_1 from a normal distribution with mean 1540 m/s and standard deviation of 154 m/s (ten percent of the commonly used standard, as discussed), selecting c_2 from a normal distribution with a mean of 5350 m/s and standard deviation of 535 m/s (again, ten percent of the commonly used value), and keeping radius constant at 0.4 dimensionless units.

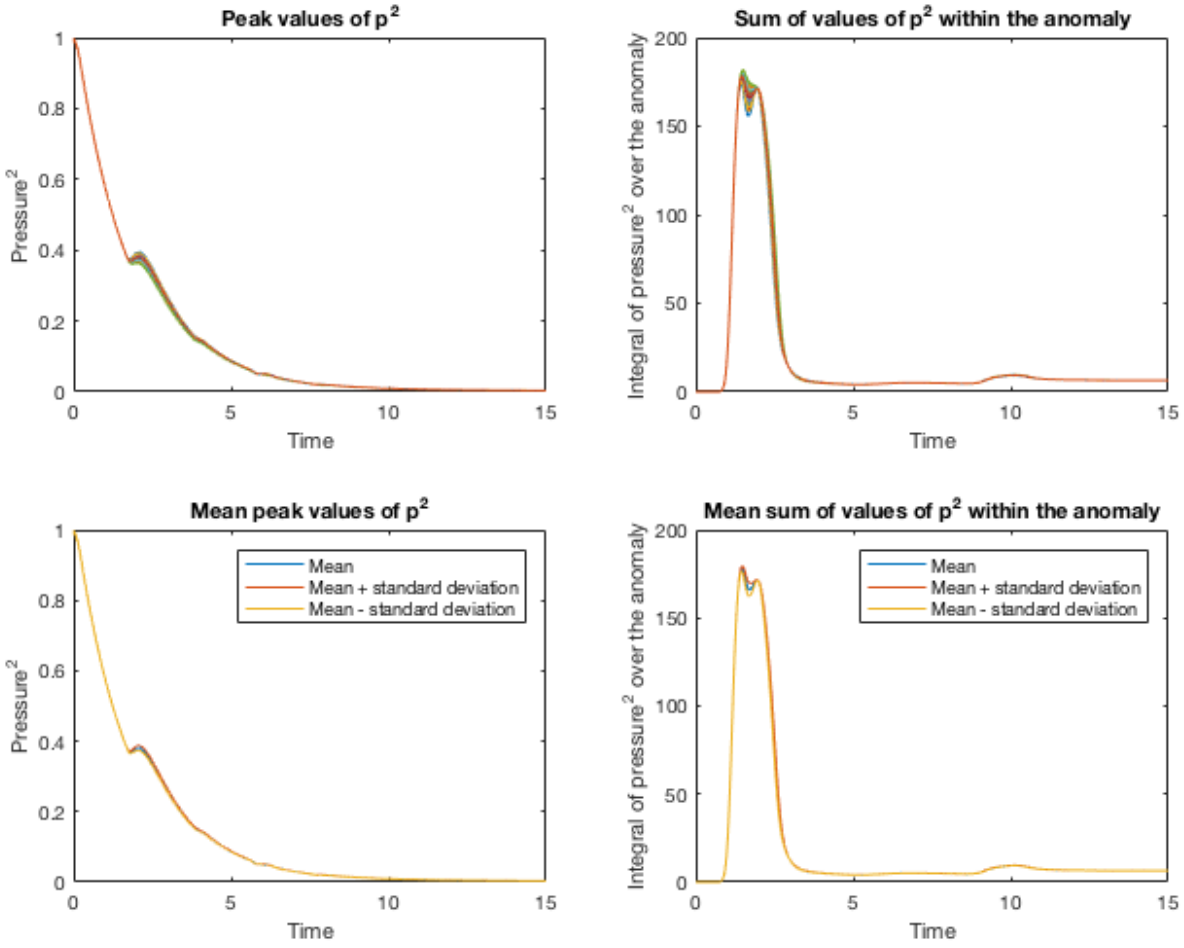

Figure 3.11: Case 4 (from Table 3.1): Time series depicting an ensemble of 100 varying c_1 and c_2. Parameter: $r = 0.4$. Top left: The peak value of pressure squared as a function of time for each member of the ensemble. Top right: The sum of pressure squared as a function of time within the anomaly area for each member of the ensemble. Bottom left: The mean for the ensemble of the peak value of pressure squared as a function of time. Bottom right: The mean for the ensemble of the sum of pressure squared as a function of time within the anomaly area.

Figures 3.12 and 3.13 plot the maximum value of the sum of pressure squared inside the anomalous region versus the speed of sound outside of the anomaly, c_1, and versus the speed of sound inside the anomaly, c_2, respectively.

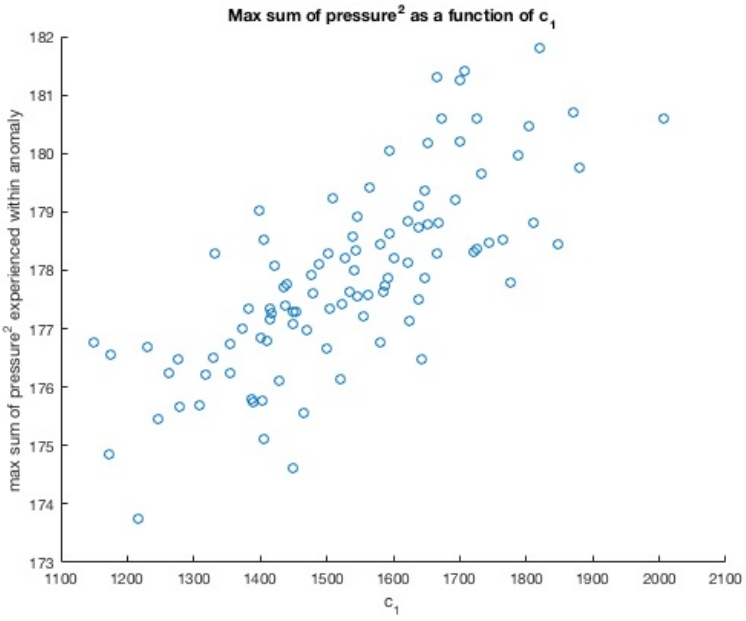

Figure 3.12: Case 4: Correlation of c_1 with the maximum value of the sum of pressure squared inside the anomaly achieved in a run when varying c_1 and c_2. Parameter: $r = 0.4$

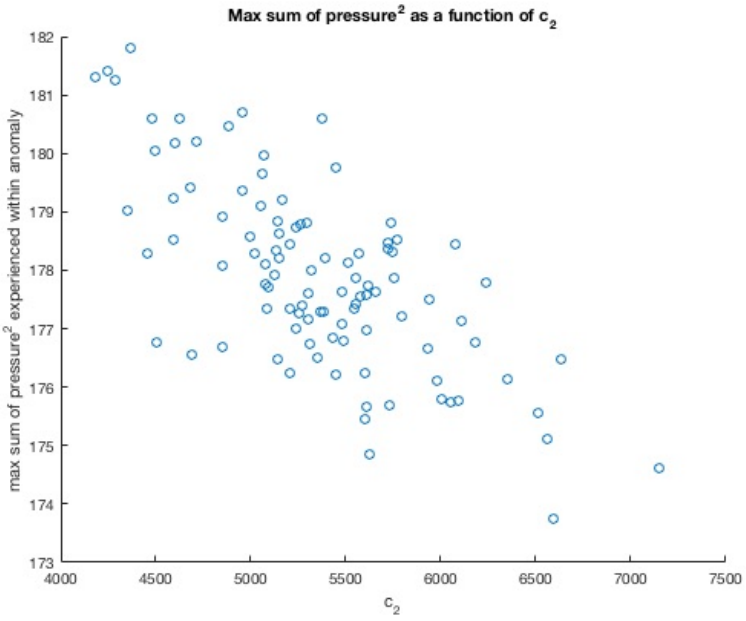

Figure 3.13: Case 4: Correlation of c_2 with the maximum value of the sum of pressure squared inside the anomaly achieved in a run when varying c_1 and c_2. Parameter: $r = 0.4$

To get a better idea of how the two variables, c_1 and c_2, together affect the maximum pressure squared, Figure 3.14 shows a colour plot where the colour represents the maximum pressure squared for a pair of variable speeds and Figure 3.15 shows a three-dimensional representation of the maximum value of the sum of pressure squared inside the anomalous region versus c_1 and c_2. Figures 3.16, 3.17, and 3.18 show the same three-dimensional representation as Figure 3.15 but with the MatLab fitting routines poly11, poly22, poly33, respectively.

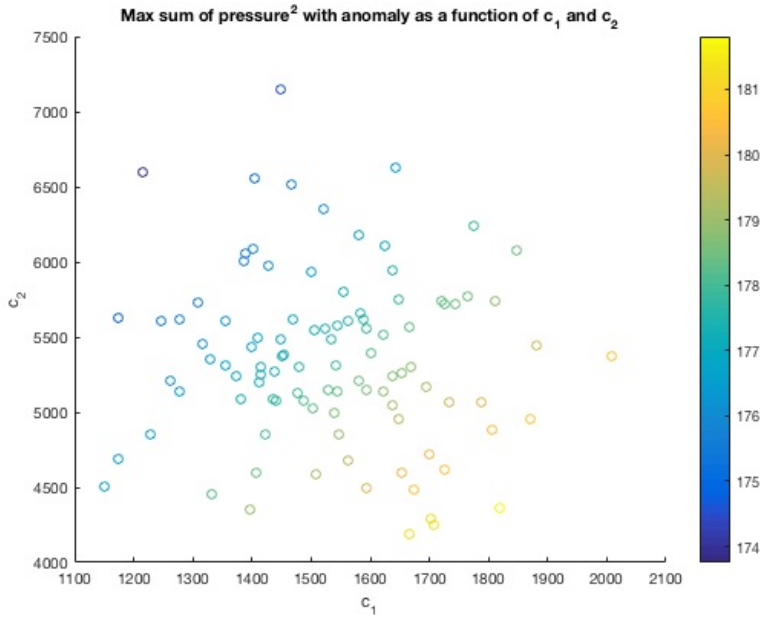

Figure 3.14: Case 4: The maximum value of the sum of the pressure squared inside the anomaly as a function of c_1 and c_2. Parameter: $r = 0.4$

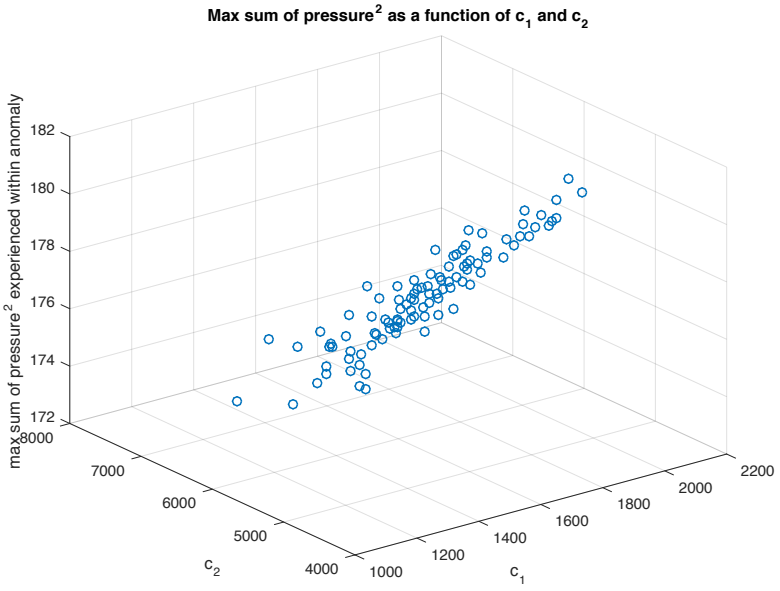

Figure 3.15: Case 4: Correlation of c_1 and c_2 with the maximum value of the sum of pressure squared inside the anomaly achieved in a run which varied both c_1 and c_2. Parameter: $r = 0.4$

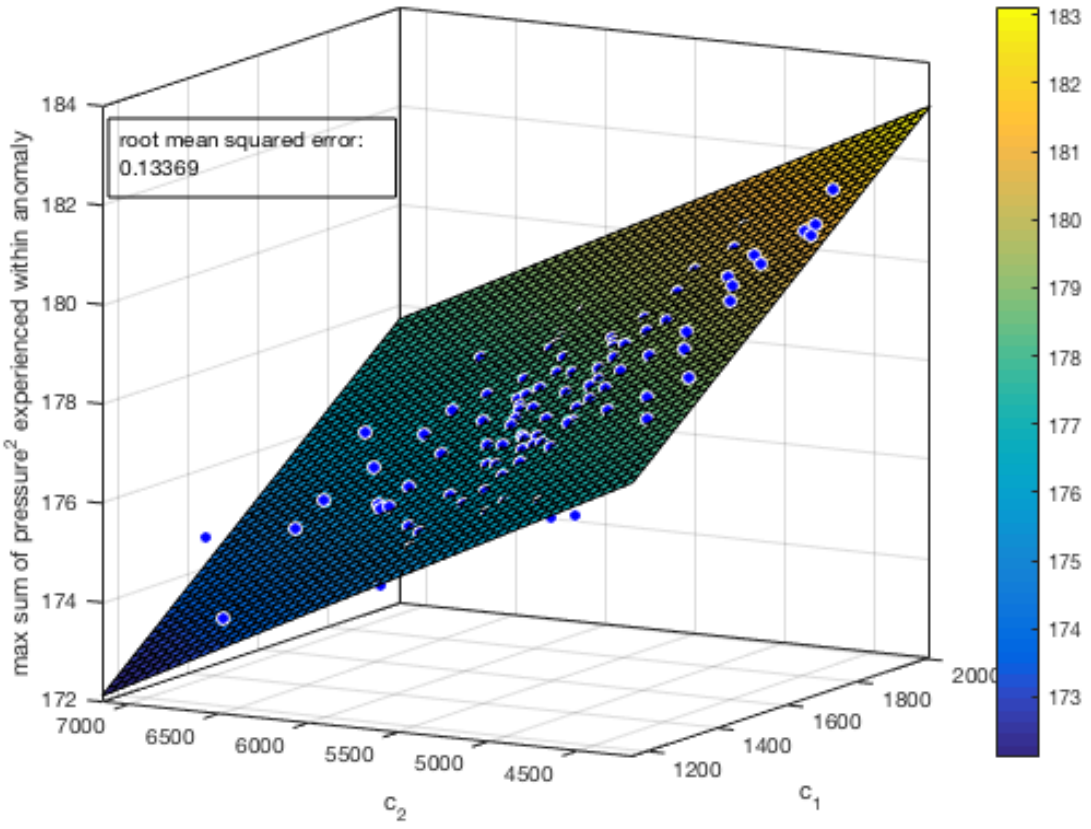

Figure 3.16: Case 4: Poly11 fit to the correlation of c_1 and c_2 with the maximum value of the sum of pressure squared inside the anomaly achieved in a run which varied both c_1 and c_2. Parameter: $r = 0.4$

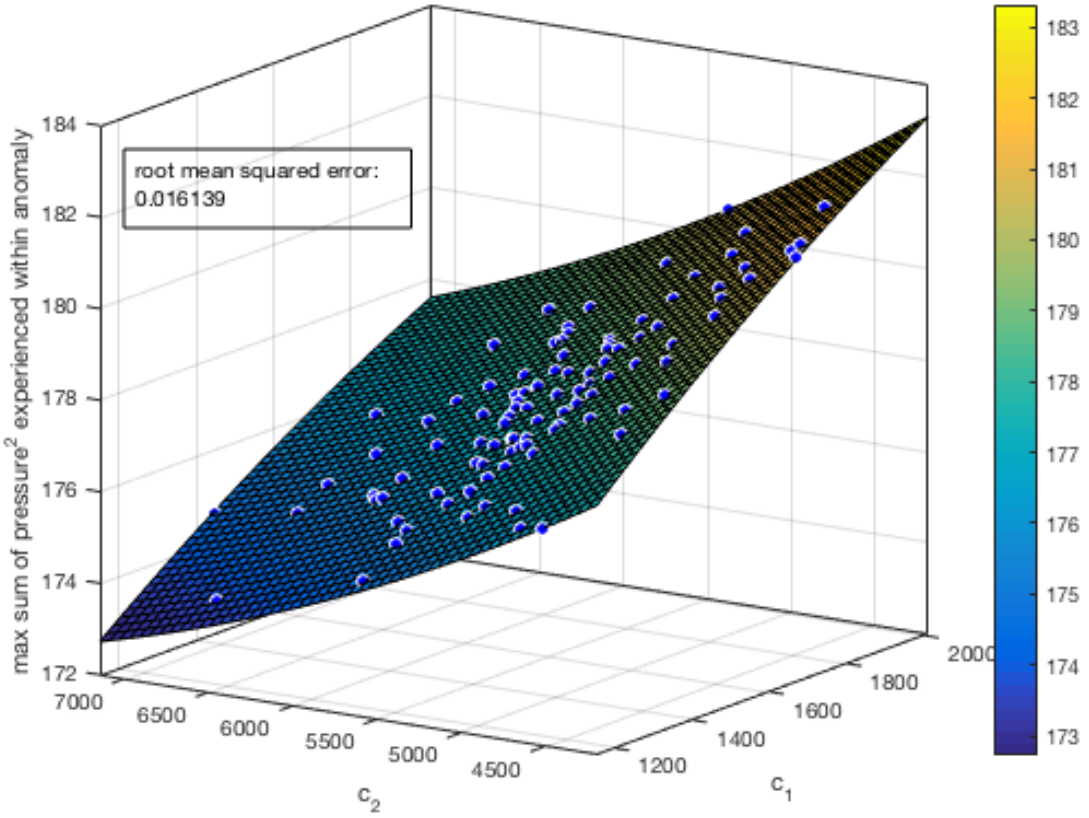

Figure 3.17: Case 4: Poly22 fit to the correlation of c_1 and c_2 with the maximum value of the sum of pressure squared inside the anomaly achieved in a run which varied both c_1 and c_2. Parameter: $r = 0.4$

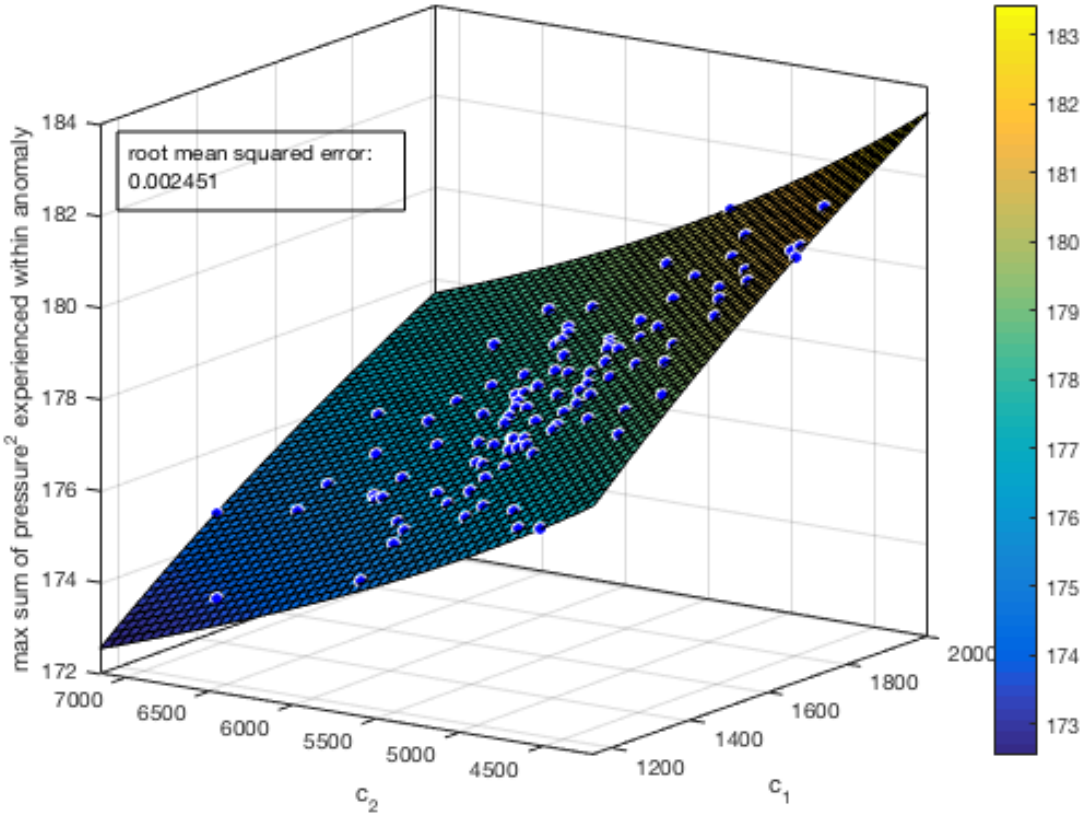

Figure 3.18: Case 4: Poly33 fit to the correlation of c_1 and c_2 with the maximum value of the sum of pressure squared inside the anomaly achieved in a run which varied both c_1 and c_2. Parameter: $r = 0.4$

Note that the root mean squared error is 0.13369 for the poly11 fit, 0.016139 for the poly22 fit, and 0.002451 for the poly33 fit. Again we see changes in an order of magnitude but this time as we increase the order of the fit in each direction. Figure 3.19 collapses the results down by looking at how the maximum pressure squared related to the ratio of c_1 to c_2, as well as several polynomial fits to the data.

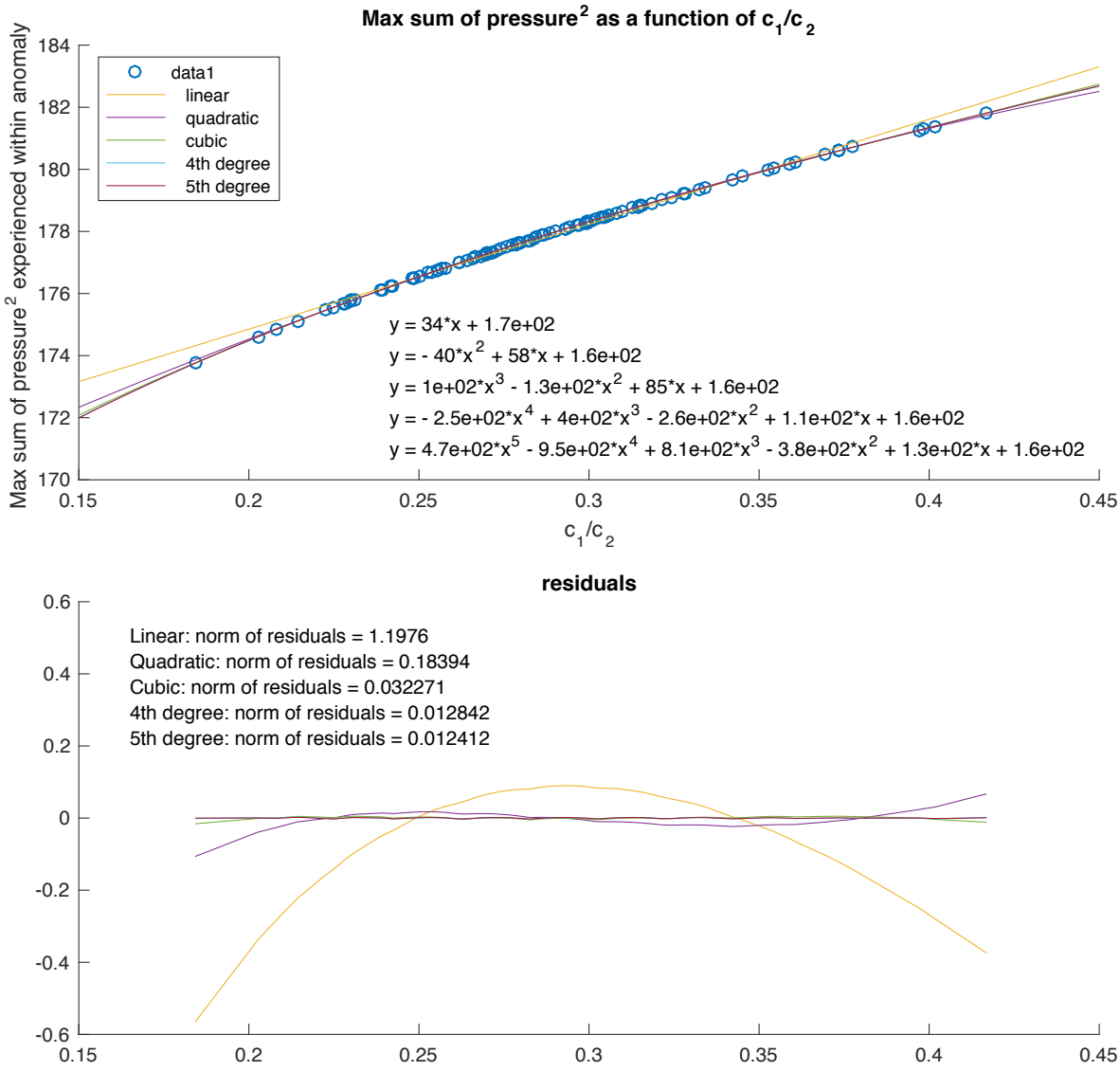

Figure 3.19: Case 4: Top: The normalized maximum value of the sum of the pressure squared inside the anomaly as a function of $\frac{c_1}{c_2}$ with five orders of polynomial fits. Bottom: The residuals for the polynomial fits shown in the top graph. Parameter: $r = 0.4$. Varying c_1 and c_2.

Notice that Figure 3.19 closely resembles Figure 3.5 so it appears that it is really the

ratio of the speeds that affects the results (as c_2 was constant for Figure 3.5). From Figure 3.19 it can be concluded that larger ratios of c_1 to c_2 lead to larger sums of pressure squared since the linear approximation ($y = 34x + 170$) has a positive slope. And once again, moving to the quadratic approximation reduces the residual by an order of magnitude but continuing to increase the order of the approximation has little effect. The greatest maximum of the sum of pressure squared inside of the anomaly was 181.8100 and the least was 173.7551 so there is less than a five percent difference over the ensemble.

3.2.5 Normal distributions for c_1 and c_2 throughout the domain

Figure 3.20 shows the results of the simulation when selecting c_1 from a normal distribution with mean 1540 m/s and standard deviation of 154 m/s (ten percent of the commonly used standard, as discussed) at every point in the section of domain assigned to be 'tissue' and selecting c_2 from a normal distribution with a mean of 5350 m/s and standard deviation of 535 m/s (again, ten percent of the commonly used value) at every point throughout the section of domain assigned to be 'bone'.

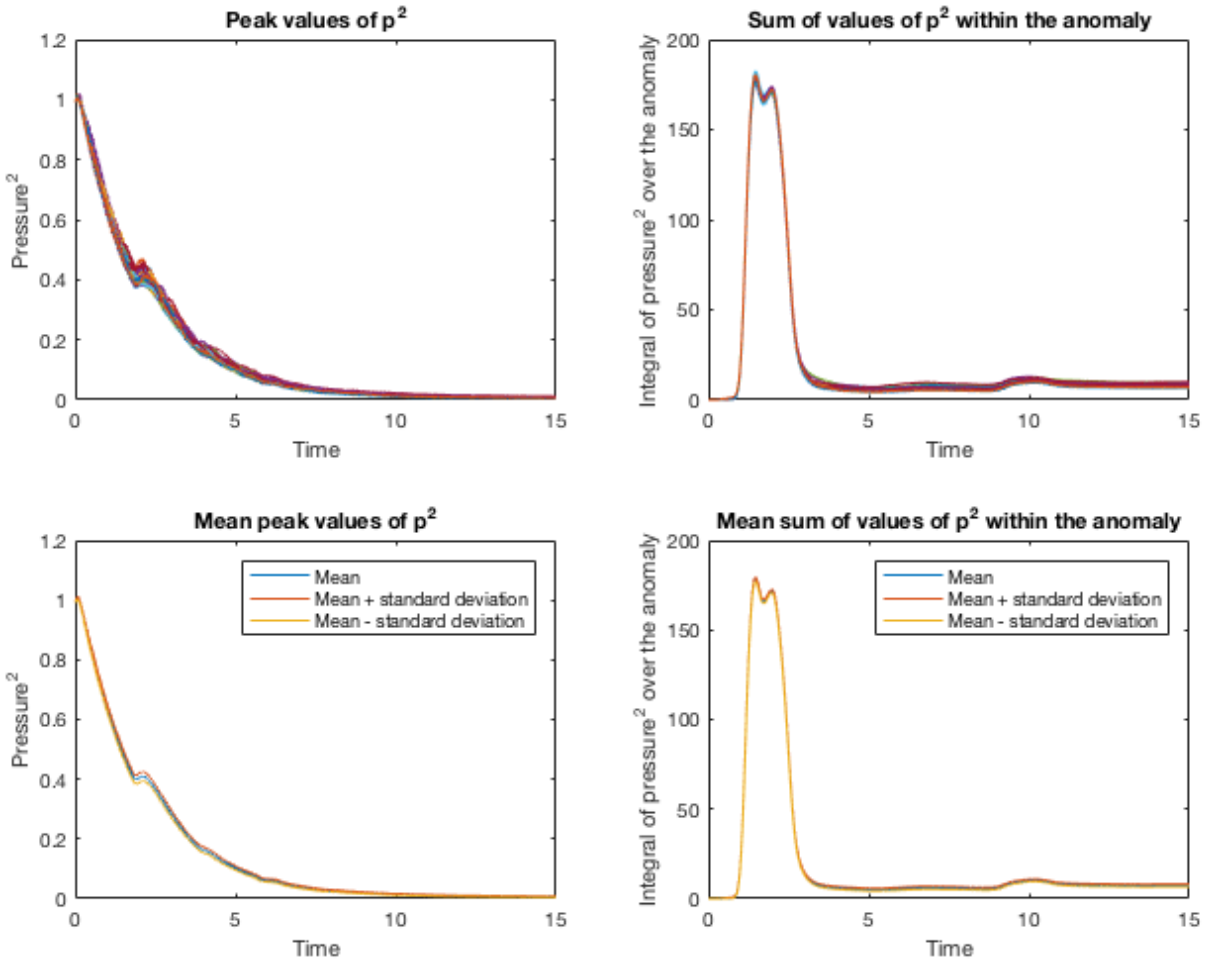

Figure 3.20: Case 5 (from Table 3.1): Time series depicting an ensemble of 100 varying c_1 and c_2 throughout the domain. Parameter: $r = 0.4$. Top left: The peak value of pressure squared as a function of time for each member of the ensemble. Top right: The sum of pressure squared as a function of time within the anomaly area for each member of the ensemble. Bottom left: The mean for the ensemble of the peak value of pressure squared as a function of time. Bottom right: The mean for the ensemble of the sum of pressure squared as a function of time within the anomaly area.

Because of the random selection of values throughout the domain, the same scatter plots as used in section 3.2.4 are not useful. The bottom left plot of mean peak values of p^2 shows a bit more variation than in the equivalent plot in Figure 3.11 but the bottom

right plot of the mean sum of values of p^2 within the anomaly shows less variation than its equivalent plot in Figure 3.11. The greatest maximum of the sum of pressure squared inside of the anomaly was 182.6114 and the least was 174.9528 so there is less than a five percent difference over the ensemble.

3.2.6 Normal distributions for c_1, c_2 and radius

Figure 3.21 shows the results of the simulation when selecting c_1 from a normal distribution with mean 1540 m/s and standard deviation of 154 m/s (ten percent of the commonly used standard, as discussed), selecting c_2 from a normal distribution with a mean of 5350 m/s and standard deviation of 535 m/s and selecting the radius from a normal distribution with a mean of 0.4 dimensionless units and a standard deviation of 0.04 dimensionless units. Note that the right-hand plots in Figure 3.21 show values normalized by the mean area.

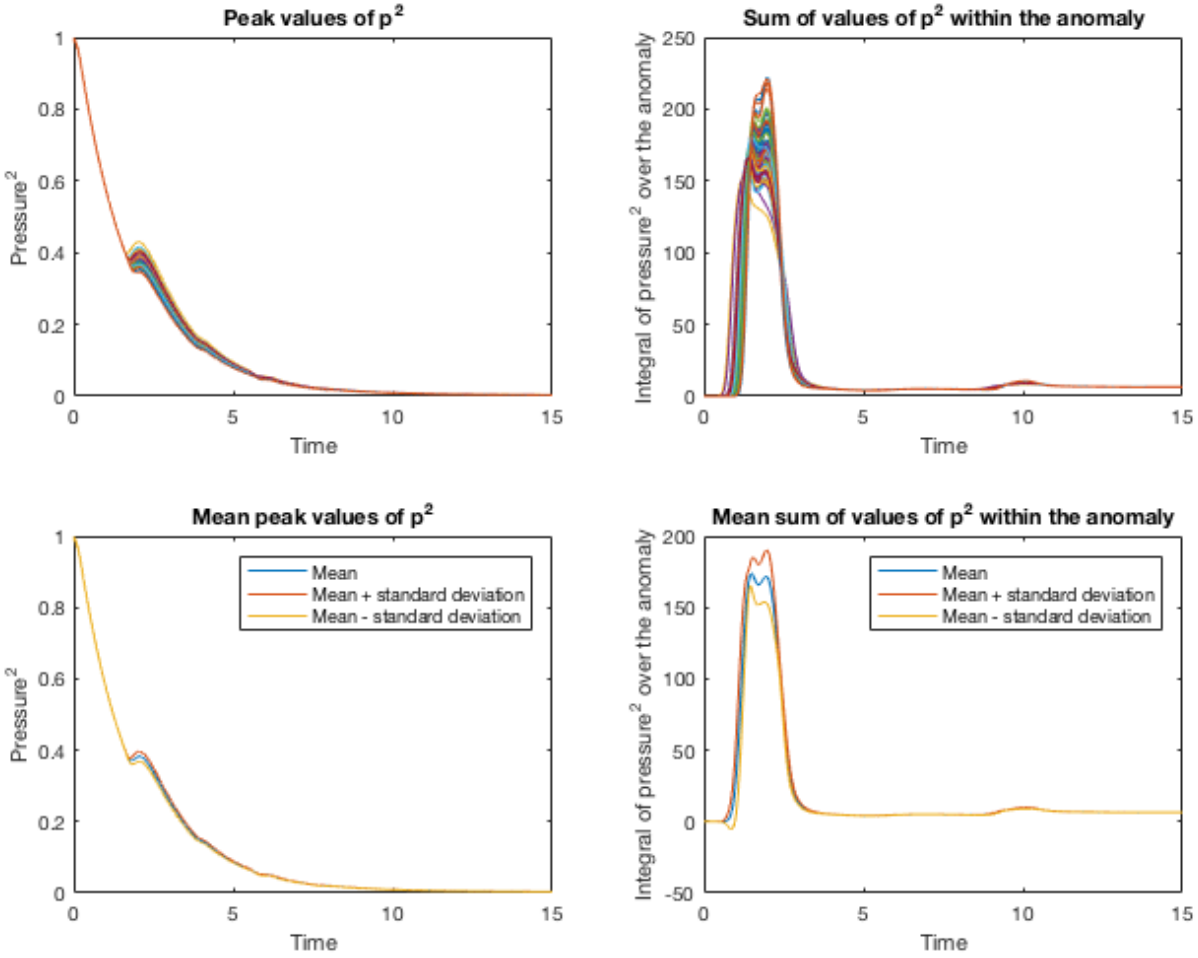

Figure 3.21: Case 6 (from Table 3.1): Time series depicting an ensemble of 100 varying c_1, c_2, and radius. Top left: The peak value of pressure squared as a function of time for each member of the ensemble. Top right: The sum of pressure squared as a function of time within the anomaly area for each member of the ensemble. Bottom left: The mean for the ensemble of the peak value of pressure squared as a function of time. Bottom right: The mean for the ensemble of the sum of pressure squared as a function of time within the anomaly area.

The variation in the bottom left plot, the mean peak values of p^2, is similar to that seen in Figure 3.20 but there is clearly a great deal of variation in the bottom right plot, the mean sum of values of p^2 within the anomaly, similar to Figure 3.9 when the radius of the

anomaly is changed. The greatest maximum of the normalized sum of pressure squared inside of the anomaly was 222.1815 and the least was 152.8651 with a mean of 178.6889 so the max can rise over twenty-four percent above the mean and drop over fourteen percent below the mean. Figure 3.22 uses the normalized data to see how the combination of the radius and $\frac{c_1}{c_2}$ affect the maximum of the sum of the pressure squared in the anomaly.

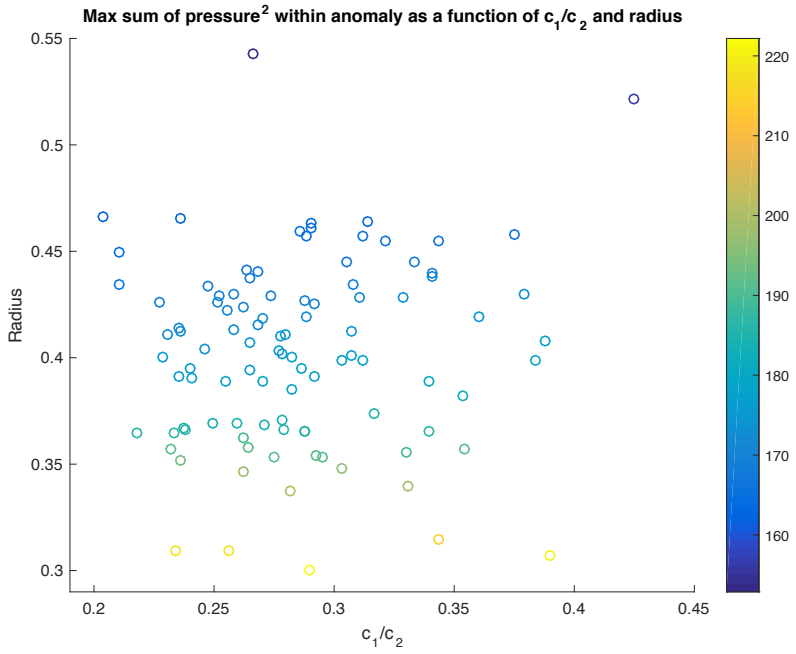

Figure 3.22: Case 6: The normalized maximum value of the sum of the pressure squared inside the anomaly as a function of $\frac{c_1}{c_2}$ and radius.

According to Figure 3.22 a smaller radius appears to contribute to higher pressure squared sums.

3.3 Conclusions

Subsection 3.2.1 shows that varying only the speed in the tissue yields small changes in the pressure squared metric. The bottom left plot in Figure 3.3 shows that the resulting variability in the peak values is extremely small on the scale of the mean values. Figure 3.4

shows that when summing the pressure squared within the anomaly, the resulting variation is not negligible on the scale of the mean values. Figure 3.5 shows the exceptionally flat quadratic relation between the speed of sound in the tissue and the resulting maximum value found for the sum of pressure squared in the anomalous area. Looking at the scales though, a significant change in the speed of sound in the tissue is required to make a comparatively small change in the squared pressure metric. Subsection 3.2.2 takes a similar look at c_2 and finds a similar conclusion, significant changes in the speed of sound in the bone is required to make a comparatively small change in the squared pressure metric.

Subsection 3.2.3 shows that varying the radius of the anomaly yields larger changes. The bottom left plot of Figure 3.9 shows that while the variation in the peak values is still small, it is reasonably discernible from the mean values (certainly more so than in Figures 3.3 and 3.6). The bottom right plot in Figure 3.9 shows even greater variation from changing the radius, particularly in comparison with the corresponding plots in Figures 3.3 and 3.6. Figure 3.10 shows the relation between the radius of the anomaly and the resulting maximum value found for the sum of the pressure squared in the anomalous area. Note that the normalized sum of the pressure varies from twenty-four percent above to ten percent below the mean when varying the radius, compared to the less than three percent difference over the ensemble when varying the speeds of sound individually. This indicates that a small reduction in radius can make a more significant change in the squared pressure metric than was the case when varying c_1 or c_2 individually.

Subsection 3.2.4 shows that varying the speed of sound in both materials yields similar results to section 3.2.1. The bottom left plot in Figure 3.11 matches rather closely with the plots in Figure 3.3 and 3.6 but the one in Figure 3.11 shows more resulting variability than the other two. Figures 3.14 and 3.19 show that larger ratios of the speed of sound in tissue to that in bone result in larger maximum values of the sum of pressure squared within the anomaly. Comparing Figures 3.5 and 3.8 with Figure 3.19, varying the ratio of the speeds has more effect than varying a speed individually.

Varying radius in addition to the speed of sound in both materials in subsection 3.2.6 shows results along the lines of subsection 3.2.3. The figures depicting the peak values of pressure squared anywhere in the simulations (the bottom left plots in 3.3, 3.6, 3.9, 3.11, 3.20, and 3.21) show reasonably similar results. However the bottom right plot of Figure 3.21, like that in Figure 3.9, shows more variability than the plots in either Figure 3.3, 3.6 or Figure 3.11. Finally, addressing Figure 3.22, varying radius as well as the speed of sound in both media results in changes of approximately thirty-eight percent in the maximum value of the sum of pressure squared in the anomalous region, compared to the roughly thirty-four percent change when varying only radius, five percent change when varying both speeds, and three percent change when varying only one speed. Clearly, the

variations in radius have a more significant effect than the speed of sound in the media but the most significant effects are seen for smaller radii and larger ratios of the speed of sound in tissue to that in bone.

Therefore variation in the shape of an anomaly has much more effect on the treatment than variation in the speeds of sound in the various media. More effort and resources should be put into determining the precise shape of bones and other anomalies than testing the tissue properties which determine their corresponding speed of sound. Once the shape is accurately known then the ultrasound forcing can be tuned appropriately.

Chapter 4

Future Work

Continuing work could be in a few directions:

- Investigating the sensitivity of parameters when the tissue surrounds a material of lower density (and thus lower sound speed). We chose to focus on the situation of tissue surrounding bone in Chapter 3 but the work in Chapter 2 showed a much bigger difference when the anomaly was of a softer material.
- Tuning the model to the parameters actually used in HIFU. The work so far has been non-dimensionalized as an easier way to get a grasp on the effects investigated. To be used in a less theoretical sense the model would need to be tuned to true parameter values used in practical applications of HIFU.
- The model can be expanded to investigate 3D effects, particularly for the interaction with bones as they are anisotropic. This model has essentially dealt with a wave front approaching perpendicularly to the longitudinal axis of a bone, ie. a roughly circular bone cross section. The model can be expanded to deal with waves approaching bones at any angle. Even further, bones come in many shapes and sizes and one could adapt the model to investigate particular bone structures.
- Finally, the model can be coupled to the Pennes bioheat equation. Not only would this give more usable information as to the temperatures achieved but the tissue properties are not actually independent of temperature. The acoustic properties of tissue change as that tissue is heated but when cells are killed they also have different properties again. Coupling the acoustics with the bioheat model would allow for a more complete picture of what is happening.

References

[1] M. A. Biot. Theory of Propagation of Elastic Waves in a FluidSaturated Porous Solid. II. Higher Frequency Range. *The Journal of the Acoustical Society of America*, 28(2):179–191, 1956.

[2] Sebastien Crouzet, Francois J. Murat, Gilles Pasticier, Philippe Cassier, Jean Y. Chapelon, and Albert Gelet. High intensity focused ultrasound (HIFU) for prostate cancer: Current clinical status, outcomes and future perspectives. *International Journal of Hyperthermia*, 26(8):796–803, 2010.

[3] Xiaobing Fan and Kullervo Hynynen. The effects of curved tissue layers on the power deposition patterns of therapeutic ultrasound beams. *Medical Physics*, 21(1):25–34, jan 1994.

[4] Luis L. Ferrás, Neville J. Ford, Maria L. Morgado, João M. Nóbrega, and Magda S. Rebelo. Fractional Pennes' Bioheat Equation: Theoretical and Numerical Studies. *Fractional Calculus and Applied Analysis*, 18(4):1080–1106, 2015.

[5] Thomas James Hudson, Thomas Looi, Samuel Pichardo, Joao Amaral, Michael Temple, James M. Drake, and Adam C. Waspe. Simulating thermal effects of MR-guided focused ultrasound in cortical bone and its surrounding tissue. *Medical physics*, 45(2):506–519, feb 2018.

[6] R. O. Illing, J. E. Kennedy, F. Wu, G. R. Ter Haar, A. S. Protheroe, P. J. Friend, F. V. Gleeson, D. W. Cranston, R. R. Phillips, and M. R. Middleton. The safety and feasibility of extracorporeal high-intensity focused ultrasound (HIFU) for the treatment of liver and kidney tumours in a Western population. *British Journal of Cancer*, 93(8):890–895, 2005.

[7] James E Kennedy. High-intensity focused ultrasound in the treatment of solid tumours. *Nature Reviews Cancer*, 5(April):321–327, 2005.

[8] Tobias Klatte, Nils Kroeger, Uwe Zimmermann, Martin Burchardt, Arie S. Belldegrun, and Allan J. Pantuck. The contemporary role of ablative treatment approaches in the management of renal cell carcinoma (RCC): Focus on radiofrequency ablation (RFA), high-intensity focused ultrasound (HIFU), and cryoablation. *World Journal of Urology*, 32(3):597–605, 2014.

[9] R J LeVeque. *Finite Difference Methods for Ordinary and Partial Differential Equations: Steady-State and Time-Dependent Problems*. Other Titles in Applied Mathematics. Society for Industrial and Applied Mathematics, 2007.

[10] George D Ludwig. The Velocity of Sound through Tissues and the Acoustic Impedance of Tissues. *The Journal of the Acoustical Society of America*, 22(6):862–866, 1950.

[11] Ezekiel Maloney and Joo Ha Hwang. Emerging HIFU applications in cancer therapy. *International Journal of Hyperthermia*, 31(3):302–309, 2015.

[12] James Ross McLaughlan. *An investigation into the use of cavitation for the optimisation of high intensity focused ultrasound (HIFU) treatments*. PhD thesis, University of London, 2008.

[13] Janelle A. Molloy, Gordon Chan, Alexander Markovic, Shawn McNeeley, Doug Pfeiffer, Bill Salter, and Wolfgang A. Tome. Quality assurance of U.S.-guided external beam radiotherapy for prostate cancer: Report of AAPM Task Group 154. *Medical Physics*, 38(2):857–871, 2011.

[14] P M Morse and K U Ingard. *Theoretical Acoustics*. International series in pure and applied physics. McGraw-Hill, 1971.

[15] Henry H. Pennes. Analysis of Tissue and Arterial Blood Temperatures in the Resting Human Forearm. *Journal of Applied Physiology*, 1(2):93–122, 1948.

[16] Thomas D. Rossing, editor. *Springer Handbook of Acoustics*. Springer New York, New York, NY, 2007.

[17] R. Samanipour, M. Maerefat, and H. Rezaei Nejad. Numerical study of the effect of ultrasound frequency on temperature distribution in layered tissue. *Journal of Thermal Biology*, 38(6):287–293, 2013.

[18] Karun V. Sharma, Pavel S. Yarmolenko, Haydar Celik, Avinash Eranki, Ari Partanen, Anilawan Smitthimedhin, Aerang Kim, Matthew Oetgen, Domiciano Santos, Janish Patel, and Peter Kim. Comparison of Noninvasive High-Intensity Focused Ultrasound

with Radiofrequency Ablation of Osteoid Osteoma. *Journal of Pediatrics*, 190:222–228.e1, 2017.